Effective Field Theory Methods:
From New-Physics Searches in Beta Decays to Strong Interactions

Maria Dawid

A dissertation
submitted in partial fulfillment of the
requirements for the degree of

Doctor of Philosophy

University of Washington

2025

Reading Committee:

Vincenzo Cirigliano, Chair

Wouter Dekens

Sanjay Reddy

Program Authorized to Offer Degree:
Physics

University of Washington

Abstract

Effective Field Theory Methods:
From New-Physics Searches in Beta Decays to Strong Interactions

Maria Dawid

Chair of the Supervisory Committee:
Vincenzo Cirigliano
Physics

The Standard Model (SM), while having been confirmed experimentally with remarkable accuracy, faces both theoretical and experimental challenges. Beta decay serves as a stringent probe for potential physics beyond the SM. To enhance its utility, advances are required in three key aspects of beta decays: enhancing the sensitivity of the experiments, improving the precision of the SM calculations, and developing theoretical frameworks capable of accommodating new physics. In this thesis, all three paths were investigated and discussed, with Effective Field Theory (EFT) providing the central framework. We employ the Standard Model EFT (SMEFT) to parametrize possible new interactions at energies above the electroweak scale and connect them to low-energy observables. Furthermore, we employed Chiral Effective Field Theory to systematically include higher-order corrections and suppress theoretical uncertainties, a key step toward enabling CKM unitarity tests with a precision at the 10^{-4} level.

In addition to precision tests of the Standard Model through beta decay, the research advances the theoretical description of strongly interacting many-body systems using Chiral Effective Field Theory (ChEFT). ChEFT is an effective field theory that systematically describes the interactions of pions and nucleons, allowing the construction of nuclear forces. While two-body potentials provide the largest contributions to these interactions, three-nucleon (3N) forces can play an important role in systems like nuclei or neutron stars. The

current derivation of the 3N force does not take into account the effects of interactions that involve four nucleons and two pions, with a coefficient proportional to the square of the pion mass, momentum, or energy. Although suppressed in conventional power counting, renormalization arguments promote these interactions to leading order. When the pions are integrated out, we find that these operators induce a sizable, previously unaccounted-for contribution to the 3N force.

TABLE OF CONTENTS

Page

LIST OF FIGURES

ACKNOWLEDGMENTS

First of all, I would like to sincerely thank my Ph.D. advisor, Prof. Vincenzo Cirigliano, for his guidance, mentorship, and most of all, patience. I am grateful for the time he always found for the discussions on physics. I especially thank him for teaching me a thoughtful approach to physics, one that is not solely based on performing increasingly complicated calculations but seeks deeper insight in physics. I am also grateful for his support during the more difficult moments of my Ph.D., which helped me continue moving forward.

I would also like to thank Prof. Chen-Yu Liu, who was my advisor at Indiana University. I am deeply grateful for her guidance and support; without her, I would not be where I am today. Her advice and perspective were invaluable to me, both scientifically and personally. I am especially thankful for the many inspiring conversations we had, which reminded me why physics is exciting and helped me stay motivated to continue in research.

I would like to thank all my collaborators from the University of Washington, Indiana University, and the UCNτ collaboration, whithout whom my resarch would not have been possible. I am especially grateful to Prof. Wouter Dekens, whose help was essential throughout my work. I learned a lot from him, and I truly appreciate both our friendship and the many discussions on physics that deepened my understanding and guided my work.

I would like to thank my family and friends for their constant support throughout my time in graduate school. I am especially grateful to my parents and siblings for always being there for me. I would also like to thank my friends – Krzysztof, Katherine, Krystyna, Leandro, Patrick, Piotr, Daniel, Sangsik, Sebastián, Yukari, Hsuan-Chu, and Dan – for their companionship and encouragement. I deeply value the time we shared, and I am thankful for their friendship, support, and understanding throughout this journey.

Finally, I would like to thank my beloved husband Sebastian, for his love and support. He has been my closest companion through every stage of this journey, sharing both the

challenges and the accomplishments with me. I am especially grateful for his understanding and for the countless ways he made this time more manageable and meaningful. Without his support, completing this Ph.D. would not have been possible.

.

DEDICATION

In memory of my father.

Chapter 1

INTRODUCTION

Effective Field Theory (EFT) is a comprehensive and widely used framework in modern theoretical physics. It provides a systematic and model-independent approach to describing physical systems that manifests a separation of energy scales [10, 11]. By focusing on the relevant low-energy degrees of freedom and organizing interactions according to symmetry principles and power counting – which orders interaction terms by their expected size based on the expansion parameter – EFT enables reliable predictions even when the underlying high-energy dynamics are unknown or unmanageable [12, 13]. This dissertation explores, analyzes, and improves the various EFT methods by applying them to two central, nuclear problems: precision studies of nuclear and neutron beta decays and the theoretical description of nuclear many-body interactions.

The first topic explored in this thesis – beta decay – is an important tool for probing physics beyond the Standard Model (SM). The SM is the theory describing the interactions of all known elementary particles, with its predictions confirmed by experimental data up to the TeV energy scale [14]. While the SM has been extensively validated, it fails to account for several well-established phenomena, such as neutrino masses, the existence of dark matter, and the observed matter–antimatter asymmetry of the universe. In addition, the SM faces unresolved theoretical challenges, including the hierarchy problem, the strong CP problem, and the unexplained flavor structure of the CKM and PMNS matrices [15]. This suggests that the SM is incomplete and, if the new physics resides at a high mass scale, it should be seen as the leading term of an effective field theory [10].

The resulting theory is the Standard Model Effective Field Theory (SMEFT) [16, 17], which extends the SM with higher-dimensional operators that are suppressed by inverse powers of a new physics scale (Λ). This theoretical framework allows for a systematic exploration of potential deviations from the SM predictions in terms of new physics of

ultraviolet origin.

In this thesis, we identify the SMEFT operators that induce the largest loop-level contributions to charged-current (CC) processes, such as beta decays of the neutron, nuclei, and mesons [18]. These include four-quark and semileptonic four-fermion operators, each involving two third-generation quarks. These interactions do not contribute to beta decay at tree level but can enter indirectly through loop-level quantum corrections. These contributions can be probed without making assumptions about flavor symmetries and are constrained by precision observables at energy scales approaching $\Lambda \sim 8$ TeV.

To use beta decay as a sensitive BSM probe within this framework, it is essential to reduce both experimental and theoretical uncertainties. This interplay between precision measurements and the theoretical description using EFT methods is a central theme of the first part of this thesis. In this thesis, we contributed to both experimental and theoretical efforts aimed at improving the precision of beta decay studies.

On the experimental side, this thesis presents results from the UCNτ experiment [19], which is designed to measure the neutron lifetime with unprecedented precision. A precise determination of the neutron lifetime and correlation coefficients is critical for extracting the axial coupling constant g_A and V_{ud} CKM matrix element, testing the consistency of the SM weak interaction, and probing potential signatures of BSM physics.

On the theoretical side, we present the first step to improved accuracy of radiative corrections within the framework of chiral perturbation theory (ChPT). In particular, our efforts focused on refining the theoretical inputs needed for the extraction of the CKM matrix element V_{ud} from superallowed beta decays. These improvements are essential for enabling future tests of CKM unitarity at the 10^{-4} level, which is the current experimental uncertainty that we'd like to match theoretically, hence increasing the sensitivity of beta decay observables to potential new physics effects.

The second focus of this thesis is the structure of nuclear forces, which emerge from the strong interaction among nucleons. While Quantum Chromodynamics (QCD) provides the fundamental description of quarks and gluons, its strongly coupled behavior at low energies makes direct calculations in nuclear systems challenging. Chiral Effective Field Theory (ChEFT), based on the symmetries of QCD, enables a controlled expansion of nuclear

interactions in terms of nucleons and pions and nucleons, allowing the construction of nuclear forces.

Two-body potentials, which describe interactions between two nucleons, provide the largest contributions to the nuclear forces. However, the three-nucleon (3N) force can play an important role in dense systems like nuclei or neutron stars. The current derivation of the 3N force does not take into account the effects of the so-called d_2 operator. Although this interaction is suppressed in conventional power-counting estimates, Kaplan, Savage, and Wise [20] showed that renormalization requires this quark mass-dependent term already at the leading order. There are also two analogous operators that are proportional to the pion momentum and energy rather than to m_π^2. In this thesis, we investigate the consequences of the d_2 operator for the 3N force, finding that it leads to a significant contribution that has not been accounted for so far [21].

1.1 Beta decay

One of the key nuclear phenomena that has been studied in this thesis is beta decay. Beta decay is a weak interaction process in which a neutron, either free or bound in an atomic nucleus, decays into a proton, while emitting an electron and an electron antineutrino

$$n \to p + \bar{\nu}_e + e^- \tag{1.1}$$

This weak process is illustrated in Fig. 1.1.

In the full electroweak Standard Model, beta decay arises from the exchange of a virtual W^- boson between quarks and leptons. The relevant charged-current interaction responsible for $d \to u$ is given by the Lagrangian

$$\mathcal{L}_{\rm CC} = -\frac{g}{2\sqrt{2}} \left[\bar{u}_i \gamma^\mu (1-\gamma^5) V_{ij} d_j + \bar{\nu}_\ell \gamma^\mu (1-\gamma^5) \ell\right] W_\mu^+ + \text{h.c.}, \tag{1.2}$$

where g is the $SU(2)_L$ gauge coupling and V_{ij} is the Cabibbo-Kobayashi-Maskawa (CKM) quark mass mixing matrix. The fields u_i and d_j denote up- and down-type quarks, while ℓ and ν_ℓ represent charged leptons and neutrinos, respectively, and W^+ is the charged weak gauge boson.

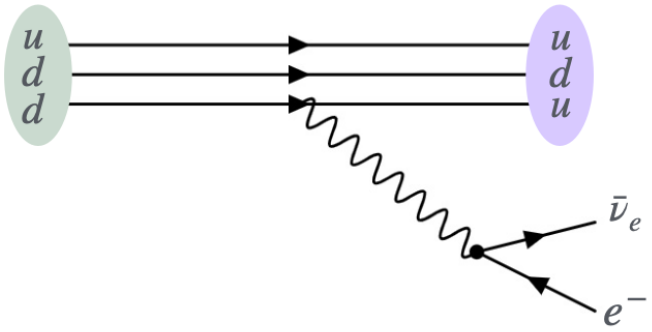

Figure 1.1: Feynman diagram illustrating neutron beta decay at the quark level. The down quark inside the neutron (udd) undergoes a weak transition to an up quark, mediated by a virtual W^- boson, resulting in a proton (uud) and the emission of an electron (e^-) and electron antineutrino ($\bar{\nu}$).

At energies much lower than the electroweak scale, the W boson can be integrated out, yielding an effective four-fermion interaction. This results in Fermi theory [22] description of beta decay

$$\mathcal{L}_{e\nu du} = -\sqrt{2} G_F V_{ud} \bar{e}\gamma_\mu \nu_L \cdot \bar{u}\gamma^\mu(1-\gamma^5)d + h.c.\ , \tag{1.3}$$

where $G_F = 1.1663788(6)\times 10^{-5}$ GeV^{-2} is the Fermi constant determined with high precision from muon decay. A more detailed discussion of this effective field theory description is provided in Section 2. Within this framework, all other parameters governing beta decay are either well-known or can be precisely calculated, allowing one to extract the fundamental SM parameter V_{ud} from experiment. Precise determination of V_{ud} is important for testing the unitarity of the CKM matrix, and consequently, the Standard Model itself.

Before the full electroweak theory was developed, beta decay was described effectively by the Lee-Yang Lagrangian [23–26],

$$\begin{aligned}\mathcal{L}_{\text{Lee}-\text{Yang}} = &-\bar{p}\gamma^\mu n\left(C_V^+ \bar{e}\gamma_\mu \nu_L + C_V^- \bar{e}\gamma_\mu \nu_R\right) - \bar{p}\gamma^\mu\gamma_5 n\left(C_A^+ \bar{e}\gamma_\mu \nu_L - C_A^- \bar{e}\gamma_\mu \nu_R\right) \\ &- \bar{p}n\left(C_S^+ \bar{e}\nu_L + C_S^- \bar{e}\nu_R\right) - \frac{1}{2}\bar{p}\sigma^{\mu\nu} n\left(C_T^+ \bar{e}\sigma_{\mu\nu}\nu_L + C_T^- \bar{e}\sigma_{\mu\nu}\nu_R\right) \\ &+ \bar{p}\gamma_5 n\left(C_P^+ \bar{e}\nu_L - C_P^- \bar{e}\nu_R\right) + \text{h.c.}\ ,\end{aligned} \tag{1.4}$$

where C_X^+ (C_X^-) are Lee-Yang effective coupling constants describing right (left)-handed interactions. The generality of this Lagrangian, including all terms allowed by Lorentz symmetry (scalar (S), vector (V), tensor (T), axial-vector (A), and pseudoscalar (P)), eventually revealed the V-A structure of the weak interactions, and is nowadays used to probe BSM effects.

At hadronic energies, where quarks are confined inside nucleons, Eq. (1.3) must be translated into hadronic degrees of freedom. The effective interaction becomes

$$\mathcal{L}_{e\nu np} = -\sqrt{2}G_F V_{ud}\bar{e}\gamma_\mu\nu_L \cdot \bar{p}\gamma^\mu(g_V + g_A\gamma^5)n + h.c. \ , \tag{1.5}$$

where p and n are proton and neutron fields, g_V and g_A are respectively the vector and axial-vector couplings. The conservation of the vector current implies that $g_V = 1$, as the vector current is protected by an exact symmetry in the isospin limit. In contrast, the axial coupling g_A is not symmetry-protected and receives significant renormalization from strong interactions.

Precise determination of V_{ud} from neutron beta decay, which is sensitive to V and A currents, therefore requires accurate knowledge of the ratio $\lambda = g_A/g_V$. The dependence of V_{ud} on the measured neutron lifetime and the axial coupling is expressed as

$$|V_{ud}|^2 \propto \frac{1}{\tau_n(1+3\lambda^2)} \ , \tag{1.6}$$

emphasizing the importance of both experimental and theoretical precision of neutron decay for testing the Standard Model [27, 28].

Neutron beta decay provides a clean tool for studying the weak interaction at low energies. The neutron is electrically neutral and only subject to weak and strong forces, hence it avoids complications arising from electromagnetic and nuclear many-body interactions that affect nuclear beta decays. This makes neutron decay a valuable tool for determining fundamental parameters such as the axial-vector coupling ratio $\lambda = g_A/g_V$, and the CKM matrix element V_{ud}, as well as for testing the unitarity of the CKM matrix and the validity of the Standard Model.

The most relevant terms in the differential decay rate of a polarized neutron to unpolar-

ized final states are as follows [28–31]:

$$\begin{aligned}\left(\frac{d\Gamma}{dE_e d\Omega_e d\Omega_\nu}\right)_0 &= \tfrac{(G_F V_{ud})^2}{(2\pi)^5} F(E_e)|\vec{p}_e|E_e(E_0-E_e)^2(1+3\lambda^2)g_V^2\left(1+\tfrac{\alpha_{\rm em}}{2\pi}\delta^{(1)}(E_e)\right)\\ &\times\left(1+(a+\delta a_r)\left(1+\tfrac{\alpha_{\rm em}}{2\pi}\delta^{(2)}(E_e)\right)\tfrac{\vec{p}_e\cdot\vec{p}_\nu}{E_e E_\nu}+b\tfrac{m_e}{E_e}\right.\\ &\left.+\hat{\sigma}\cdot\left[(A+\delta A_r)\left(1+\tfrac{\alpha_{\rm em}}{2\pi}\delta^{(2)}(E_e)\right)\tfrac{\vec{p}_e}{E_e}+(B+\delta B_r)\tfrac{\vec{p}_\nu}{E_\nu}+D\tfrac{\vec{p}_e\times\vec{p}_\nu}{E_e E_\nu}\right]\right)\ ,\end{aligned} \tag{1.7}$$

where $\hat{\sigma}$ is the unit neutron polarization vector, and $E_0 = (M_n^2 - M_p^2 + m_e^2)/(2M_n)$ is the end-point energy, corresponding to the maximum electron energy. E_e, E_ν are the energies and, $\vec{p}_e$, $\vec{p}_\nu$ are momenta of respectively the electron and antineutrino. $F(E_e)$ is the Fermi function accounting for the Coulomb interaction between the final-state proton and the emitted electron. m_e is the mass of the electron.

The correlation coefficients a, b, A, B, D encode the angular and spin correlations between the decay products and are defined as follows:

- a: Electron–antineutrino angular correlation coefficient. Sensitive to the axial-vector to vector coupling ratio, $\lambda = g_A/g_V$.

- A: Electron asymmetry parameter. Measures the angular distribution of the electron with respect to the neutron spin.

- B: Neutrino asymmetry parameter. Analogous to A but for the antineutrino.

- D: Triple correlation coefficient. Probes time-reversal (T) violation; it involves the scalar triple product of momenta and spin.

- b: Fierz interference term. Sensitive to non-Standard Model scalar or tensor couplings.

The terms $\delta a_r, \delta A_r, \delta B_r$ represent recoil-order corrections (of order $\sim 1/M$) generated by e.g., the nucleon magnetic moment. $\delta^{(1)}$ and $\delta^{(2)}$ are radiative corrections from the virtual photon and bremsstrahlung effects, their expressions might be found in Ref. [32].

1.1.1 History of experiments of beta decay

The first experiments on radioactivity occurred at the turn of the 20th century, marking the beginning of a new field in physics. The earliest study of beta decay is considered to be Rutherford's experiment in 1899, in which he identified new particles emitted from radioactive material known today as beta-particles [33]. In 1900, Henri Becquerel recognized that these particles are in fact electrons by measuring the mass to charge m/s ratio [34]. Following experimental observations revealed that electrons emitted in beta decay had a continuous energy distribution, which violates energy conservation [35–37]. In order to explain this energy spectrum, Wolfgang Pauli postulated the existence of a light neutral particle that is emitted together with the electron [38]. This was explained by Enrico Fermi in 1933, who formulated a theory of beta decay in terms of a contact interaction between four fermions [22]. Fermi's theory introduced the concept of the weak interactions and provided a remarkably successful description of beta decay rates and spectra, laying the groundwork for the later electroweak theory. This is explained in more detail in Section 2.

In the meantime, in 1932 Chadwick discovered the neutron, showing the existence of a neutral particle with a mass similar to, but slightly larger than that of the proton, suggesting the possibility of its decay [39]. Soon after, it was found by Gamow and Teller [40] that the form of the interaction had to be generalized to include spin-dependent interactions.

The most general form of the interaction Hamiltonian term is

$$H = \sum_i C_i \int d^3x (\bar{u}_p \, \hat{O}_{1i} \, u_n)(\bar{u}_e \, \hat{O}_{2i} \, u_\nu) \ , \tag{1.8}$$

where u_p, u_n, u_e, and u_ν denote the wave functions of the four particles, and the operators allowed by (Lorentz) symmetry are $\hat{O}_{1,2i} \in (1, \gamma_\mu, \sigma_{\mu\nu}, i\gamma^5\gamma_\mu, \gamma^5)$, which corresponds to scalar (S), vector (V), tensor (T), axial vector (A), and pseudoscalar (P), respectively. In the non-relativistic limit, S and V reduce to the Fermi interaction, while T and A reduce to Gamow-Teller [41].

The major experimental breakthrough took place in 1957. Wu, Ambler, Hayward, Hoppes, and Hudson [42] experimentally demonstrated parity violation in the beta decay of polarized cobalt-60 nuclei, a possibility that was first proposed by Lee and Yang [23]. One year later, Goldhaber et al. [43] measured the helicity of the neutrino and confirmed it is

left-handed. This result provided evidence supporting the vector minus axial-vector (V–A) structure of the weak force.

These two key findings challenged the existing symmetric models and pointed toward a chiral structure of the weak force. In response, Marshak and Sudarshan [44] and later Feynman and Gell-Mann [45], proposed the V–A theory, postulating that the weak interaction couples only to left-handed components of fermion fields and the right-handed components of antifermion fields. This theory predicts that the weak charged current has a specific combination of vector (V) and axial-vector (A) couplings with equal magnitude and opposite sign.

Between 1961 and 1967, Glashow [46], Weinberg [47], and Salam [48] developed the electroweak theory, which unifies the weak and electromagnetic interactions in a single theory described by a gauge symmetry that is unbroken at high energies above the electroweak scale, ~ 100 GeV. The first experimental verification of this theory came in 1973 from the Gargamelle experiment at CERN, which discovered neutral currents. [49]. A definitive confirmation followed in 1978 with electron-scattering experiments at SLAC, leading to the first determination of the weak mixing angle[50].

In charged-current interactions the next experimental efforts were focused on improving the precision of beta decay measurements, mainly with the use of superallowed transition $0^+ \to 0^+$. These experiments have been collected in several surveys [51–53]. The superallowed decays are purely Fermi transitions, meaning they are mediated only by the vector component of the weak interaction, and involve no change in nuclear spin or parity. As a result, beta decays provide a clean and theoretically well-understood tool for testing the conservation of the vector weak current and extracting the CKM matrix element V_{ud}. However, reaching sub-percent precision in V_{ud} is limited by nuclear-structure effects, which remain a significant source of theoretical uncertainty. Addressing these challenges motivates efforts such as our project, aimed at improving the calculation of δ_{NS}. This in turn allows to test unitarity of the CKM matrix. Further details on probing the Standard Model with the use of the CKM unitarity are provided in the following section.

Simultaneously, neutron lifetime measurements were started shortly after the development of neutron sources from nuclear reactors. Initial lifetime results showed the neutron

lifetime to be around $10 - 30$ min. The first approximate measurement was performed by Robson et al. in 1951, where they reported a neutron half-life to be 1108 ± 216 s [54]. In 1972, Christensen et al. improved precision using magnetic spectrometry to reduce the acceptance systematic errors and reported $\tau_n = 918 \pm 14$ s [55]. These first measurements were performed using beam-based experiments, in which neutrons decay while traveling through a well-collimated beam. The resulting decay products – protons – are detected downstream, allowing the decay rate to be determined. An alternative to beam-based experiments involves the use of ultracold neutrons (UCNs), which are characterized by extremely low kinetic energies, typically below a few hundred nanoelectronvolts. This allows them to be stored in magnetic or gravitational traps for extended periods, making them well-suited for precise lifetime measurements [56]. A comparison of neutron lifetime results from several experiments performed since the early 1980s is shown in Fig. 1.2. These methods, together with the explanation of the neutron lifetime anomaly, are described in detail in section 3.1.

The first experiments were subject to large measurement errors due to low UCN densities in traps, which lead to losses of neutrons losses in the apparatus. These losses, in turn, complicated the extrapolation of the trap storage time to the true neutron lifetime, introducing additional systematic errors [56]. In the following years, the probability of neutron loss decreased from $\sim 30\%$ [57] to $\sim 1\%$ [58] among other things, thanks to using an open gravitational trap.

Up to 2004, the two main methods of experiments – beam [59] and bottle type agreed. In 2004, Serebrov et al. found the neutron lifetime to be $\tau_n = 878.5 \pm 0.7_{stat} \pm 0.3_{sys}$, using a novel gravitational trap technique. [60]. This result differed from the then-current Particle Data Group (PDG) world average by approximately 6.4σ, sparking significant debate and skepticism within the community due to the unexpectedly large discrepancy. The next measurements with the use of magnetic trapping techniques confirmed this shorter lifetime with significantly improved precision [61–64], while the results from beam-based experiments have remained consistently higher, converging around $\tau_n \approx 888$ s [65] as illustrated in Fig. 1.2. This discrepancy is widely known as the neutron lifetime anomaly, and could be a hint of BSM physics.

In 2017, the Los Alamos National Laboratory published the first neutron lifetime result

using a magneto-gravitational trap for UCNs, reporting $\tau_n = 877.7 \pm 0.7_{stat} \pm 0.3_{sys}$ as part of the UCNτ experiment [66] that aligns with the smaller value of the neutron lifetime. The result was later significantly improved in 2021, incorporating better control over systematics, improved neutron counting, and extended data-taking. The updated result was: $\tau_n = 877.75 \pm 0.28_{stat}\,^{+0.22}_{-0.16}\,_{sys}$, making it the most precise single measurement of the neutron lifetime to date [19]. This particular experiment is explained in more detail in Chapter 3, as it is one of the main topics of this thesis.

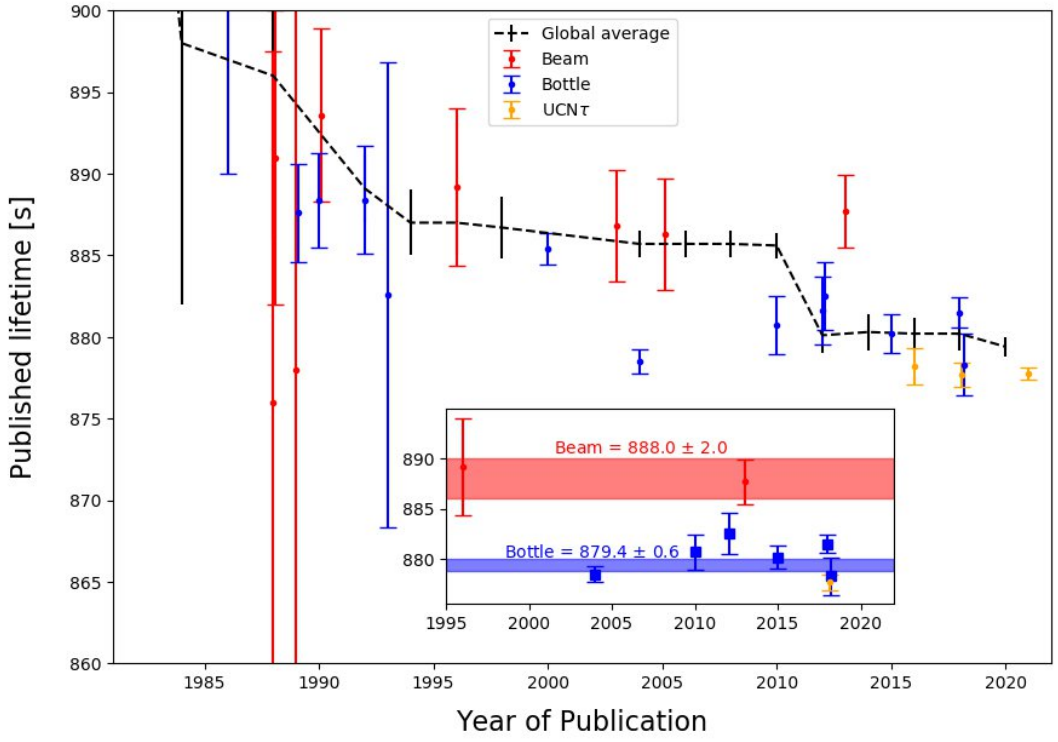

Figure 1.2: A comparison of neutron lifetime results from several experiments performed since the early 1980s. Beam experiments shown in red, and bottle in blue. The UCNtau project's recent results are shown in yellow.

In addition to measuring the neutron lifetime, correlation coefficients appearing in the neutron decay rate (see Eq. 1.7) have also been experimentally probed. Some of the notable experiments are PERKEO II/III at the Institute Laue-Langevin, which used a cold

neutron beam, and reported the neutrino asymmetry parameter $B = 0.9802(50)$ [67], and the proton asymmetry parameter $C = -0.2377(26)$ [68]. Complementary measurements were performed by the Ultracold Neutron Asymmetry (UCNA, UCNA+) experiment at Los Alamos National Laboratory, which used ultracold neutrons (UCNs) to minimize systematic uncertainties and improve control over the neutron polarization [69, 70], reporting $A_0 = -0.12015(34)_{stat}(63)_{syst}$ and $\lambda = g_A/g_V = -1.2772(20)$. The experiment measuring the electron-antineutrino a-coefficient in free neutron decay was measured by the aCORN experiment at the National Institute of Standards and Technology. The most recent reported result is $a = -0.10779 \pm 0.00125_{stat} \pm 0.00133_{sys}$, and $\lambda = g_A/g_V = -1.2712 \pm 0.0061$ [71] that improved aSPECT result [72]. There is a mild tension between values of g_A extracted from measurements of the electron–antineutrino correlation coefficient a and those obtained from beta asymmetry parameter A, an issue currently under investigation in precision beta-decay studies.

1.1.2 Probing beyond the Standard Model physics through beta decays

Beta decay is particularly important for probing physics beyond the Standard Model (BSM) from multiple perspectives. Due to the high precision achieved in both experiments and theoretical calculations, it enables tests of fundamental predictions of the SM, such as the unitarity of the CKM quark mixing matrix as described below.

The unitarity of the Cabibbo–Kobayashi–Maskawa (CKM) [73, 74] quark mixing matrix requires

$$V_{\mathrm{CKM}} V_{\mathrm{CKM}}^{\dagger} = \begin{pmatrix} V_{ud} & V_{us} & V_{ub} \\ V_{cd} & V_{cs} & V_{cb} \\ V_{td} & V_{ts} & V_{tb} \end{pmatrix} \begin{pmatrix} V_{ud}^{*} & V_{cd}^{*} & V_{td}^{*} \\ V_{us}^{*} & V_{cs}^{*} & V_{ts}^{*} \\ V_{ub}^{*} & V_{cb}^{*} & V_{tb}^{*} \end{pmatrix} = 1 \ , \tag{1.9}$$

which implies the unitarity of the first row

$$|V_{ud}|^2 + |V_{us}|^2 + |V_{ub}|^2 = 1 \ . \tag{1.10}$$

The matrix element V_{ud} describes the strength of the weak interaction that converts a down quark into an up quark and is probed from nuclear, neutron, and pion beta decays. The

current best-fit value is $V_{ud} = 0.97378(26)$ [75]. The element V_{us} tells about the quark up to quark strange transition and is mainly determined from leptonic and semileptonic kaon decays with a current constraint of $V_{us} = 0.22422(36)$ [75]. The element V_{ub} represents the transition of the quark up to quark bottom, and is determined from rare semileptonic B-meson decays. Its squared value is approximately $|V_{ub}|^2 \simeq 1.5 \times 10^{-5}$, which is smaller than the uncertainties of the other elements and therefore neglected in the first-row unitarity test.

There is a discrepancy between these determinations, which is depicted in Fig. 1.3, that shows constraints in the V_{ud} – V_{us} plane. The black solid line represents the unitarity circle, while the yellow ellipse is 68% confidence level (C.L.) of all four combined measurements. These two do not intersect, leading to a hint for a deviation from unitarity $\Delta_{CKM} \equiv |V_{ud}|^2 + |V_{us}|^2 + |V_{ub}|^2 - 1 = -1.48(53) \times 10^{-3}$ at $\sim 3\sigma$.

These results have generated scrutiny of the SM prediction [75–87] as well as beyond the SM (BSM) studies [88–101], in the context of explicit models of new physics, in the EFT setting below the weak scale, and in the SMEFT at tree level.

Apart from the above-mentioned BSM signals, the ultracold neutron beta decay experiment UCNτ might open a window on BSM physics, via the neutron lifetime anomaly and the observation of sidereal and annual modulations in the decay rate. Although such effects cannot be generated by the SMEFT, they could be effects could be driven by dark matter (DM) or by new interactions that violate Lorentz symmetry.

Realizing the full potential of β decay experiments demand a joint theoretical and experimental effort, producing accurate theoretical calculations and thorough experimental data analysis. This challenge must be addressed by making progress on three parallel fronts:

1. Advancing theoretical frameworks for BSM

2. Improving the precision of SM calculations

3. Enhancing the accuracy of experimental analyses.

In this thesis, all three approaches are employed to improve the sensitivity of beta decay experiments to potential signatures of BSM physics with the use of EFT.

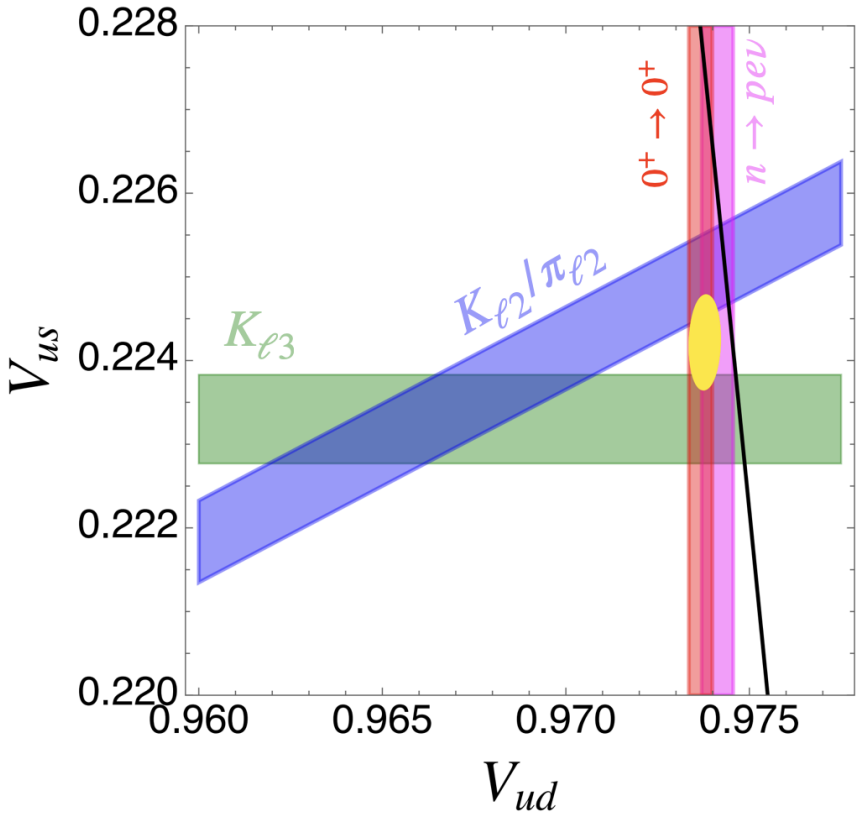

Figure 1.3: Constraints in the $V_{ud} - V_{us}$ plane. The green bar corresponds to V_{us} constrained from Kaon decay ($K \to \pi l \nu_l$) [1], the blue bar corresponds to the ratio V_{us}/V_{ud} obtained from the branching ratio $\Gamma(K \to l\nu_l)/\ \Gamma(\pi \to \mu\nu_\mu)$ [2], vertical line comes from beta decay: red from superallowed ($0^+ \to 0^+$) beta decay [3] and pink from neutron decay rate [4]. The black line denotes the unitarity circle, while the yellow ellipse is 68% C.L. of all four combined measurements. Figure taken from Ref. [5]

1.2 Nuclear forces

Nuclear forces refer to interactions occurring between two or more nucleons (protons and neutrons). The fundamental theory describing these interactions is quantum chromodynamics (QCD), which governs the behavior of quarks and gluons. QCD has an impact on nuclear forces in two primary ways. First, it dictates the dynamics of quarks and gluons within in-

dividual nucleons, and second, it gives rise at longer distances to the effective interactions between nucleons themselves [102]. These interactions are responsible for binding nucleons together to form atomic nuclei.

There are several reasons why we want to study the nature of nuclear forces. First of all, nuclear interactions describe all properties of nuclear systems such as binding energies, radii, shapes, and excitation spectra of nuclei, as well as their stability and decay modes [103, 104]. A proper understanding of these forces allows for the construction of actual nuclear interactions, which can describe and predict the behavior of both stable and exotic nuclei in the nuclear chart. Moreover, nuclear forces govern the equation of state of dense neutron-rich matter, which is essential for describing the interior structure and evolution of neutron stars [105]. Constraints on these forces, particularly at high densities, are crucial for interpreting astrophysical observations, such as gravitational wave signals from neutron star mergers [106]. Finally, precise knowledge of nuclear interactions is needed to provide a clean laboratory for probing physics beyond the Standard Model. Nuclear observables, especially those measured with high precision in beta decay, neutrinoless double beta decay, parity violation experiments, or searches for electric dipole moments, can be sensitive to subtle signatures of new interactions. Interpretation of these experimental signals requires understanding BSM effects in nuclear environments, making nuclear physics a necessary tool in the search for new fundamental forces and particles.

There are several important properties of strong interactions that need to be reproduced by an Effective Field Theory description to provide an accurate low-energy description. First, as the name suggests, they are the strongest out of all four known fundamental forces acting in nature [107]. Despite its strength, their range is of the order of $\sim 1-2$ fm, corresponding roughly to the size of a nucleon [103]. This might be explained by the fact that in the low-energy regime, the nuclear force between nucleons emerges as a residual interaction due to pion exchanges and processes at shorter distances.

Nuclear forces are approximately charge independent. That means to a good approximation, the interactions between neutron-neutron, which are charge neutral, neutron-proton and proton-proton pairs are the same once electromagnetic effects are removed [108]. This reflects the approximate isospin symmetry of QCD, which treats protons and neutrons as

two states of the same nucleon isospin doublet up to small effects due to the quark mass difference.

However, these forces are spin-dependent. The nuclear forces vary with the relative spin orientation of nucleons – it is stronger for parallel aligned spins, and weaker for anti-aligned. A well-known example illustrating this effect is the deuteron, a bound state of a proton and neutron, which exists only in the spin-triplet channel.

One of the important consequences of the properties of nuclear forces discussed above is the saturation property of nuclei. This phenomenon is related to the fact that the size of nuclei increases proportionally to the number of nucleons within it, and its approximately constant for the binding energy per nucleon is constant for different mass numbers of nuclei, which is crucial for the stability of matter [109, 110]. Physically, this arises because the nuclear force is both short-ranged and strongly repulsive at very short distances, preventing nucleons from clustering too tightly, but attractive at larger distances. First evidence of this property was observed in the deuteron, which has a non-vanishing quadrupole moment. Moreover, the Pauli exclusion principle for fermions (protons and neutrons) further limits the phase-space overlap among nucleons. An EFT displays this behavior, typically through the contact interactions and one-pion exchange terms that capture both the short-range repulsion and intermediate-range attraction between two nucleons, characteristic of the nuclear potential [111, 112]. The existence of a maximum in the nuclear binding energy per nucleon (E/A) near iron, corresponding to the saturation density of symmetric nuclear matter, is known as saturation. In effective field theory (EFT), this phenomenon arises from the interplay between two-nucleon (2N) and 3N forces.

Nuclear forces in EFTs

The development and application of effective field theory (EFT) methods to low-energy nuclear processes has had a profound impact on our understanding of nuclei and dense nuclear matter encountered in neutron stars [111, 112]. Pioneering work by Weinberg laid the foundations for describing interactions between nucleons in a systematic EFT approach [102, 113] that exploits the separation of energy scales and is consistent with the symmetries

of QCD. Chiral EFT describes interactions between nucleons at energy scales comparable to the pion mass but much smaller than the mass of the heavier mesons, such as the ρ meson. This theory organizes the operators involving nucleon and pion fields in a momentum expansion in which higher-order terms are suppressed by powers of (p/Λ_B or m_π/Λ_B), where p is the typical momentum scale of the considered process, m_π is the pion mass, and Λ_B is the breakdown scale associated with an EFT. The numerical values of the coefficients of the operators in the expansion, called the Low Energy Constants (LECs), are fixed by matching to experiments, or possibly from lattice QCD. A particularly attractive feature of the EFT approach to nuclear interactions is that it includes many-body forces naturally and organizes them in a useful hierarchy that is consistent with the momentum expansion of the two-nucleon force (2NF).

The 3N force plays a critical role in describing observables [114, 115] such as the nuclear binding energies and radii [116–128], the saturation properties of nuclear matter [129–131], and the equation of state (EOS) of dense neutron-rich matter in neutron stars [8, 132–135]. Although the magnitude of its contribution to these quantities depends on the resolution or regularization scale of the calculation, often defined by the momentum cut-off denoted by Λ, for the typical values of $\Lambda \simeq 450 - 500$ MeV, the 3N force is essential to stabilize both nuclei and neutron stars. Without the 3N force, the nuclear binding energy and saturation density would be too high, and the maximum mass and neutron star radii would be too low.

1.2.1 Outline of this thesis

This thesis is organized as follows. In Chapter 2, we introduce the theoretical frameworks used in the thesis. It reviews the general philosophy and construction of effective field theories and presents two specific examples, relevant for the subsequent discussion: the Standard Model Effective Field Theory (SMEFT) 2.1, used for model-independent analysis of new physics, and Chiral Perturbation Theory (ChPT) 2.2, which describes low-energy QCD and nuclear forces. The operator classification, symmetries, and power counting schemes relevant to both theories are discussed in detail.

Chapter 3 focuses on the application of EFT methods to neutron and nuclear beta decay.

We start with the description of the UCNτ experiment that measured the neutron lifetime. We subsequently describe the neutron lifetime anomaly as a window for probing physics BSM. Then, in Subsection 2.1, we describe and present the formalism for incorporating SMEFT contributions to beta decay observables at the one loop level and the renormalization group evolution of operators relevant for low-energy observables. Apart from describing BSM effects, we pay particular attention to radiative corrections to the SM predictions, which are crucial for reducing theoretical uncertainties in tests of CKM unitarity.

In the chapter 4, we present our research on three-nucleon forces in chiral EFT. It identifies a previously neglected operator—the so-called d_2, f_2, and e_2 term—as an essential component for the renormalization of the three-body system. The chapter analyzes the consequences of promoting this operator to leading order, including its impact on nuclear and neutron matter, and discusses its relevance for the chiral expansion of many-body nuclear interactions. In the last Chapter 5 we summarize the main findings of this work, highlight their implications for both theory and experiment, and outline potential directions for future research.

Chapter 2

EFFECTIVE FIELD THEORIES

Effective Field Theories are theoretical frameworks that describe low-energy physics, where "low" is defined relative to a certain high-energy scale Λ representing the boundary of our ignorance, beyond which the details of the underlying physics are "integrated out" [10, 12]. This means that the dynamics at low energies do not depend on the specific details of high-energy physics, allowing for a controlled and model-independent description of relevant phenomena as long as the energy of a process E is smaller than Λ. When $E \sim \Lambda$ the effective theory breaks down. In practice, an EFT is formulated as an effective Lagrangian containing an infinite series of local operators constructed from the relevant low-energy fields, organized as an expansion in powers of the ratio of the small parameter to the high-energy scale E/Λ. The effects of fields with masses heavier than Λ are now encoded in coupling constants of these operators, capturing their impact without explicitly including them as propagating states [136]. This approach is based on the observation that the non-analytic properties of scattering amplitudes come from intermediate processes in which physical particles can exist on-shell. Consequently, if virtual particles are too heavy to be physically produced, their contributions to the amplitude can be systematically expanded in powers of p^2/M^2, where M is the energy of the heavy particle, and p represents the typical momentum scale of the process [137].

This concept is well illustrated by an example of the use of an EFT, which is Fermi's effective theory of beta decay, formulated before the development of the electroweak theory of weak interactions [22]. Beta decay, one of the central topics of this thesis, is a weak interaction process in which a neutron decays into a proton, an electron, and an electron antineutrino as in Eq.1.1. In the Standard Model, this process is mediated by the W^- boson, whose mass is approximately 80 GeV, which is significantly larger than the typical momentum transfer $Q \sim$ MeV involved in the decay. At such low energies, the W^- boson

propagator can be approximated by a local contact interaction

$$\frac{-g_{\mu\nu} + q_\mu q_\nu / M_W^2}{q^2 - M_W^2} \quad \xrightarrow{q^2 << M_W^2} \quad \frac{g_{\mu\nu}}{M_W^2} \ . \tag{2.1}$$

This yields the effective Lagrangian with a contact interaction

$$\mathcal{L}_F = -\frac{1}{\sqrt{2}} G_F J^\mu J_\mu^\dagger \ , \tag{2.2}$$

with the charged weak current

$$J_\mu = \sum_{ij} \bar{u}_i \gamma_\mu (1 - \gamma_5) V_{ij} d_j + \sum_l \bar{\nu}_l \gamma_\mu (1 - \gamma_5) l \ , \tag{2.3}$$

where V_{ij} is the Cabibbo-Kobayashi-Maskawa mixing matrix, and the Fermi coupling constant is given by

$$\frac{G_F}{\sqrt{2}} = \frac{g^2}{8 M_W^2} \ . \tag{2.4}$$

This approach captures all low-energy effects of weak interactions without including explicitly the details of W^- boson exchange, showing how heavy degrees of freedom can be systematically integrated out at low energies. In this case, the underlying theory is known to be the Standard Model, making it an example of a top-down effective field theory (EFT). Here, the EFT is derived directly from the high-energy theory by integrating out heavy degrees of freedom, yielding an effective description valid at lower energies. In contrast, Fermi's original theory of weak interactions was formulated before the Standard Model was established and thus represents a bottom-up EFT, constructed without assuming detailed knowledge of the underlying high-energy theory.

EFTs offer several advantages. They simplify calculations by focusing only on the relevant degrees of freedom and interactions at a given energy scale. This allows one to work within only a single scale at a time. EFTs are also model-independent. It is not necessary to know the details of the underlying fundamental high-energy theory, but it can still include the effects of new physics in terms of coefficients of the effective Lagrangian. This was illustrated above by Fermi's effective theory of weak interactions. Nowadays, a similar framework is employed to describe physics BSM through effective interactions formulated within an EFT. An exapmle of such a theory is the Standard Model Effecitive Field Theory (SMEFT). EFTs

can also be used to describe a known underlying theory when direct calculations within it are too complex. A well-known example is Chiral Perturbation Theory (ChPT), which will be discussed in detail later.

Furthermore, EFTs are systematically improvable; calculating higher-order corrections improves the precision of predictions [10, 136].

Constructing an EFT follows a general strategy formulated in the so-called "EFT theorem", formulated by Weinberg [138], which involves three key steps:

1. Identify the relevant energy scales, in particular the high energy scale Λ, together with the relevant expansion parameter,

2. Determine the appropriate degrees of freedom active below Λ,

3. Write down all operators consistent with the symmetries of the system, organized according to a power-counting scheme.

This procedure ensures that the resulting theory captures all low-energy physics allowed by symmetry while parameterizing possible new high-energy effects.

Figure 2.1 illustrates the examples of EFTs that work at different energy regimes and describe different precision tests of the Standard Model and searches for new physics. At the highest energies, beyond the Standard Model (BSM) physics is parameterized by new degrees of freedom with characteristic masses at or above a scale Λ. Examples of theoretical frameworks describing physics at that scale include Supersymmetry, which stabilizes the Higgs mass and provides a dark matter candidate, or the previously mentioned the seesaw mechanism, which explains the smallness of neutrino masses via heavy states.

Below the scale Λ, the heavy fields introduced by the BSM frameworks are integrated out leading to the SMEFT at energies below the new-physics scale. Examples of processes that can be described within the SMEFT framework include high-energy collider experiments such as those at the LHC. In this case, the EFT description is valid only if the scale of new physics Λ is sufficiently higher than the typical energy reach of the experiment. Before applying SMEFT to LHC data, one must first ensure that there are no signals from direct

searches (such as resonant "bumps") indicating new particles within kinematic reach, and subsequently verify that the fitted EFT scale is not so low as to undermine the expansion's validity [139, 140].

At the electroweak scale, the heavy SM fields (the $W^{\pm}$, Z, Higgs boson, and top quark) are also integrated out, leading to the Low-Energy Effective Field Theory (LEFT). This framework is used to interpret precision low-energy observables such as $(g-2)_{e,\mu}$, B, and τ decays.

At energies below the characteristic Λ_χ scale of order $\mathcal{O}(1$ GeV), the relevant degrees of freedom pions, nucleons, and other particles with masses smaller that Λ_χ rather than quarks and gluons, and their dynamics are described by Chiral Perturbation Theory. Originally developed as a low-energy effective theory of QCD for processes involving pions and nucleons, ChPT provides a controlled expansion in powers of momenta and pion masses, and serves as the foundation for describing both strong and electroweak processes at hadronic scales. When applied to few-nucleon systems, Chiral EFT extends ChPT by incorporating nucleon-nucleon and three-nucleon forces generated by pion exchange and short-range contact interactions, enabling a unified treatment of nuclear structure and reactions from the same symmetry principles that underlie QCD.

Below the energy scale of order $\mathcal{O}(100$ MeV), pions are integrated out, leading to pionless nuclear EFT for few- and many-body nuclear systems. These two latter theories describe processes such as nuclear beta decay, neutrinoless double beta decay, or electric dipole moments of nuclei.

One can move along the energy scale within an EFT using renormalization group equations (RGEs), which describe how theoretical parameters evolve as the characteristic scale changes.

The Renormalization Group (RG) is a set of mathematical techniques used in quantum field theory (QFT) and statistical physics to quantify the scale dependence of the theoretical description of a given physical phenomenon. Every physical theory is defined at some characteristic scale μ, e.g., of energy, momentum, or length. In most QFTs, such a scale must be introduced in the process known as "regularization", to regulate the ultraviolet (UV) divergences that appear in the theory, both at the perturbative and non-perturbative level.

Regularization deals with the divergences, but requires the introduction of an arbitrary dimensional parameter μ. In the process of renormalization, this parameter gains an interpretation of the theory energy scale, and parameters of the theory become μ-dependent. The parameters of interest are usually couplings and masses, and RGEs appear under the name of the Callan-Symanzik equations for the correlation functions of the quantum fields. From them, one obtains differential equations for the couplings and masses. These equations are equivalent to the condition that the physical predictions of the theory shall not depend on μ, once the initial values of all parameters for a particular μ_0 are established. Consequently, the parameters of the theory become μ-dependent in such a way that the observables stay μ-independent [141].

In the context of an EFT, RGEs play an additional role by describing how operators evolve and mix when running from one energy scale to another. When moving between theories with different particle content, such as integrating out heavy degrees of freedom when transitioning from the Standard Model Effective Field Theory (SMEFT) to the Low-Energy Effective Field Theory (LEFT), one employs the matching procedure. Matching requires that the amplitudes computed in the higher and lower energy theories of physical processes be equal at the energy scale where the two effective field theories meet. Together, the RGEs and matching procedure enable a consistent connection between new-physics effects at high energies and precision observables at low energies. These two procedures are crucial in the Section 2.1.

In the next sections of this chapter, we focus on two EFTs central to this thesis: the Standard Model Effective Field Theory (SMEFT) and Chiral Perturbation Theory (ChPT). SMEFT provides a systematic framework for searching for physics beyond the Standard Model through precision studies of low-energy processes, including beta decay. ChPT, on the other hand, is essential for describing hadronic and nuclear interactions at low energies, particularly the many-body forces that govern nuclear structure and dense matter. In the following sections, we review the formulation and key features of each theory, providing the theoretical background for the original research presented in later chapters.

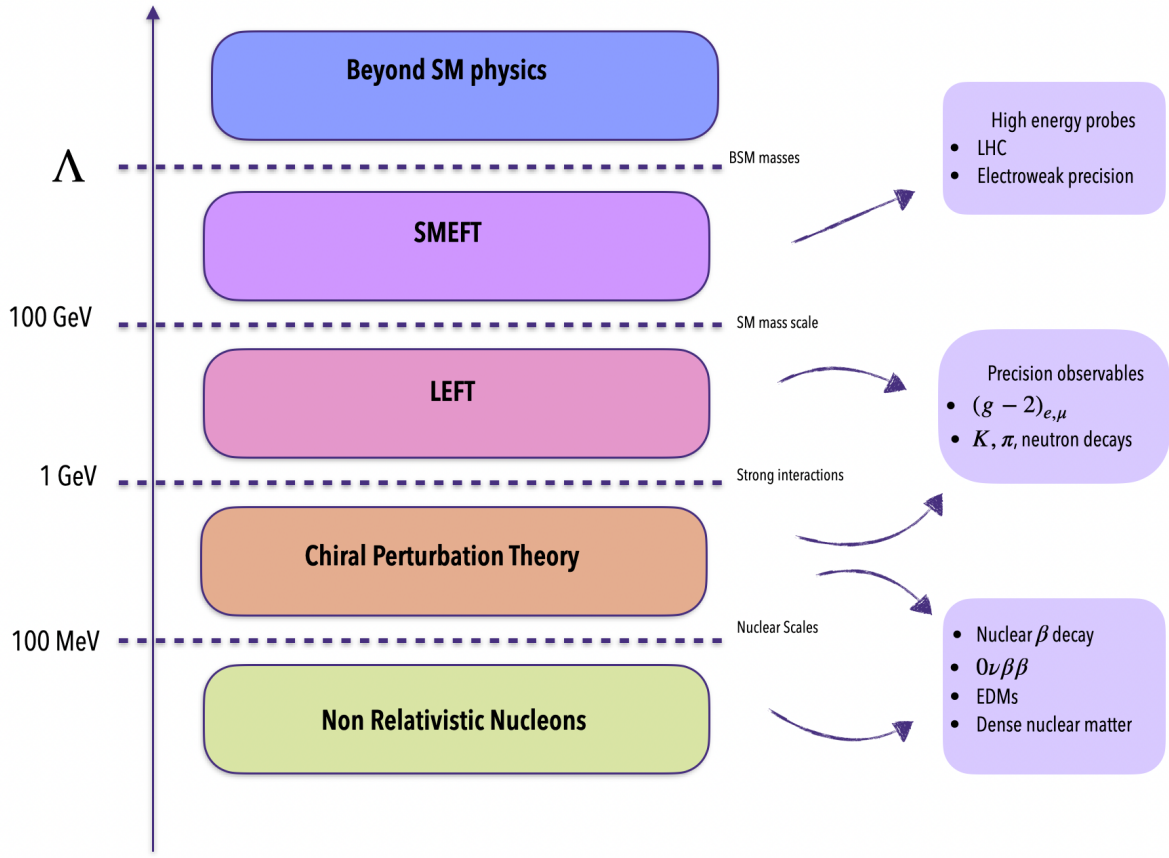

Figure 2.1: Hierarchy of effective field theories across energy scales. At the highest energies (Λ), new physics beyond the Standard Model may appear. Between the BSM and electroweak scales ($\sim$ 100 GeV), SMEFT provides a systematic description of possible new physics effects. Below the electroweak scale, LEFT captures the dynamics of Standard Model particles after integrating out heavy electroweak fields. Around the QCD scale ($\sim$ 1 GeV), Chiral Perturbation Theory describes pion–nucleon dynamics and nuclear forces, while at nuclear scales ($\sim$ 100 MeV), pionless EFT describes systems of non-relativistic nucleons.

2.1 Standard Model Effective Field Theory

The shortcomings of the SM suggest that it is an incomplete description of nature. One of the most compelling issues is the masslessness of the SM neutrinos, which contradicts neutrino

oscillation experiments. Another unfavorable issue with the SM is called the hierarchy problem. According to the theory, the mass of the Higgs particle acquires large quantum perturbative corrections from the virtual quanta which are coupled to the Higgs boson drive its mass to values much larger than observed, requiring unnatural fine-tuning. Furthermore, there is a lack of satisfying description of the dark matter and dark energy within the SM. Cosmological observations indicate that about 27% of the Universe mass comes from the dark matter, and about 67% from the dark energy, leaving only about 5% for the visible matter described by the SM.

If the new physics resides at a mass scale much higher than current experimental energies, its effects at low energies can be captured using an effective field theory (EFT) expansion, with the SM appearing as the leading term [16, 142, 143]. The resulting theory is the Standard Model Effective Field Theory, is an EFT constructed from the Standard Model fields and invariant under the full $SU(3)_C \times SU(2)_L \times U(1)_Y$ gauge symmetry of the SM. In addition to the renormalizable (dim $\leq$ 4) interactions, SMEFT includes higher-dimensional operators that encode the virtual effects of heavy particles, suppressed by inverse powers of a new physics scale (Λ). This theoretical framework allows for a systematic exploration of possible deviations from Standard Model predictions, originating from high-scale (ultraviolet) new physics [17, 144].

The SMEFT Lagrangian contains the regular SM Lagrangian $\mathcal{L}_{\text{SM}}$, which is treated now as a leading order of the SMEFT, along with the higher-dimensional operators as assured by the Appelquist–Carazzone decoupling theorem [145]

$$\mathcal{L}_{\text{SMEFT}} = \mathcal{L}_{\text{SM}} + \frac{1}{v} C^{(5)} Q^{(5)} + \frac{1}{v^2} \sum_k C_k^{(6)} Q_k^{(6)} + \dots \,. \tag{2.5}$$

Here $Q_k^{(i)}$ denotes all possible effective operators of canonical mass dimension i and $C_k^{(i)}$ are the corresponding effective constants called here Wilson coefficients [16, 17]. For convenience, we have defined the coefficients to be dimensionless, so that they scale as $C_k^{(i)} \sim (v/\Lambda)^{i-4}$, where $v \simeq 246$ GeV is the Higgs vacuum expectation value.

The first operator appearing above the renormalizable Standard Model terms has mass dimension five. At this order, there exists only a single possible gauge-invariant operator

that can be constructed from Standard Model fields, given by

$$\mathcal{L}^{(5)} = \frac{1}{v} C^{(5)}_{rs} \epsilon^{ij} \epsilon^{kl} (l^T_{ir} C l_{ks}) H_j H_l + h.c. \ , \tag{2.6}$$

where, r, s are flavor indices, and $i,\ j,\ k,\ l$ are $SU(2)_L$ gauge indices. This term is known as the Weinberg operator [142]. After electroweak symmetry breaking, where the Higgs field H acquires its vacuum expectation value $H \to (0, v)/\sqrt{2}$, this operator generates a Majorana mass term for the left-handed neutrinos ν_L

$$\mathcal{L}^{(5)} \to C^{(5)} \frac{v}{2} \bar{\nu}^c_L \nu_L \ . \tag{2.7}$$

This operator violates total lepton number by two units; it provides a natural and elegant explanation for the smallness of observed neutrino masses, linking their scale directly to the suppression factor v^2/Λ (recall that $C^{(5)} \sim v/\Lambda$). This operator is the EFT description of the seesaw mechanism, in which, for example, heavy right-handed neutrinos are integrated out, leaving behind a low-energy effect consistent with observed neutrino properties.

2.1.1 Dimension-six operators in the SMEFT

The first interactions relevant to this work arise at mass dimension six ($dim = 6$). At this order, the SMEFT includes all gauge-invariant, dimension-six operators constructed from Standard Model fields. This analysis employs a general flavor structure and adopts the widely used Warsaw basis [17], which provides a complete and non-redundant set of such operators.

These operators can be classified into eight distinct types based on their field content

$$X^3,\ H^6,\ H^4D^2,\ X^2H^2,\ \psi^2H^3,\ \psi^2XH,\ \psi^2H^2D \text{ and } \psi^4 \tag{2.8}$$

where X denotes a field-strength tensor, H the Higgs doublet, D a covariant derivative, and ψ a generic fermion field. In the absence of flavor indices (i.e., for a single generation), the Warsaw basis contains 59 independent baryon-number-conserving operators, all of which fall into one of the categories listed above. However, when all possible flavor combinations are included, the number of independent operators grows to 2,499 [146]. This complete flavor treatment is essential for capturing the full range of potential BSM effects, particularly in

processes involving first-generation quarks and leptons, as well as loop-level contributions from heavy flavors.

In the following, we discuss several representative examples of dimension-six operators relevant to this work. We begin with four-fermion operators of the ψ^4 class. In particular, we focus on four-quark operators, which can contribute to charged-current processes through loop-level effects within SMEFT.

There are four possible independent gauge-invariant color and weak isospin structures for the interactions with four left-handed quarks that can appear in the bilinears, which can be written schematically as:

$$\mathbf{1} \otimes \mathbf{1}, \quad \tau^a \otimes \tau^a, \quad T^A \otimes T^A, \quad \tau^a T^A \otimes \tau^a T^A, \tag{2.9}$$

where τ^a are the $SU(2)_L$ generators and T^A are the $SU(3)_C$ generators. These structures determine the transformation properties of the operators under the SM gauge group and dictate how they mix under renormalization and contribute to physical processes. Now using Fierz identities, such as

$$(\bar{\psi}_1 \gamma_\mu P_L \psi_2)(\bar{\psi}_3 \gamma^\mu P_L \psi_4) = (\bar{\psi}_1 \gamma_\mu P_L \psi_4)(\bar{\psi}_3 \gamma^\mu P_L \psi_2) \tag{2.10}$$

together with the group-theoretical identity

$$[T^A]^\alpha_\beta [T^A]^\lambda_\sigma = \delta^\alpha_\sigma \delta^\lambda_\beta - 1/(2N) \delta^\alpha_\beta \delta^\lambda_\sigma \ , \tag{2.11}$$

one finds that the only non-redundant color and isospin structures are the singlet $1 \otimes 1$, and triplet $\tau^a \otimes \tau^a$. N is a number of colors.

These structures correspond to different contractions of the quark bilinears and give rise to distinct classes of four-quark operators in the SMEFT. For example, the operators

$$Q^{(1)}_{\substack{qq \\ prst}} = (\bar{q}_p \gamma_\mu \tau q_r)(\bar{q}_s \gamma^\mu q_t), \tag{2.12}$$

$$Q^{(3)}_{\substack{qq \\ prst}} = (\bar{q}_p \gamma_\mu \tau^I q_r)(\bar{q}_s \gamma^\mu \tau^I q_t), \tag{2.13}$$

where color indices summed over and not explicitly displayed. These operators preserve chiral structure and can mix into semileptonic operators under renormalization group (RG) evolution. In particular, $Q^{(3)}_{qq}$ can contribute indirectly to charged-current observables such

	fermions					scalars
field	l_p^j	e_p	q_p^j	u_p	d_p	H^j
$(\dim[SU(3)_C], \dim[SU(2)_W], Y)$	$(1,2,-\frac{1}{2})$	$(1,1,-1)$	$(3,2,\frac{1}{6})$	$(3,1,\frac{2}{3})$	$(3,1,-\frac{1}{3})$	$(1,2,\frac{1}{2})$

Table 2.1: The SM matter content.

as beta decay, even if its Wilson coefficient is zero at the low scale, due to operator mixing involving top and bottom quarks.

The SM matter content is summarized in Tab. 2.1 with isospin, and generation indices denoted by $j = 1, 2$, and $p = 1, 2, 3$, respectively. Chirality indices (L, R) of the fermion fields will be skipped in what follows. Complex conjugate of the Higgs field will always occur either as $H^\dagger$ or $\tilde{H}$, where $(\tilde{H})^j = \epsilon_{jk}(H^k)^\star$, and ϵ_{jk} is totally antisymmetric with $\epsilon_{12} = +1$.

Similarly, for four-lepton operators, one may construct only the singlet and triplet

$$Q_{\substack{ll \\ prst}} = (\bar{l}_{ip}\gamma_\mu l_r^i)(\bar{l}_{js}\gamma^\mu l_t^j) \quad , \tag{2.14}$$

$$Q^{(3)}_{\substack{ll \\ prst}} = (\bar{l}_{ip}\gamma_\mu [\tau^a]^i_j l_r^j)(\bar{l}_{ks}\gamma^\mu [\tau^a]^k_m l_t^m) \quad . \tag{2.15}$$

Using Fierz identity 2.10 together with $SU(2)$ version of Eq. (2.11)

$$[\tau^a]^i_j \; [\tau^a]^k_m = 2\delta^i_m \; \delta^k_j - \delta^i_j \delta^k_m \tag{2.16}$$

the triplet 2.15 becomes

$$\begin{aligned} Q^{(3)}_{\substack{ll \\ prst}} &= (\bar{l}_{ip}\gamma_\mu [\tau^a]^i_j l_r^j)(\bar{l}_{ks}\gamma^\mu [\tau^a]^k_m l_t^m) \\ &= 2(\bar{l}_{ip}\gamma_\mu l_r^j)(\bar{l}_{js}\gamma^\mu l_t^i) - (\bar{l}_{ip}\gamma_\mu l_r^i)(\bar{l}_{js}\gamma^\mu l_t^j) \\ &= 2Q_{\substack{ll \\ ptsr}} - Q_{\substack{ll \\ prst}} \quad . \end{aligned} \tag{2.17}$$

This shows that the triplet $Q^{(3)}_{ll}$ is not independent, but it is a linear combination of singlet-type operators. Hence, only one of them needs to be retained in a minimal operator basis.

However, this simplification does not hold for mixed lepton-quark operators, where Fierz rearrangement does not lead to any relation that can be used to elmininate any operator. For example, the Warsaw basis includes

$$Q_{\substack{lq \\ prst}} = (\bar{l}_{ip}\gamma_\mu l_r^i)(\bar{q}_{js}\gamma^\mu q_t^j) \ , \tag{2.18}$$

$$Q^{(3)}_{\substack{lq \\ prst}} = (\bar{l}_{ip}\gamma_\mu [\tau^a]^i_j l_r^j)(\bar{q}_{ks}\gamma^\mu [\tau^a]^k_m q_t^m) \ . \tag{2.19}$$

In this case, singlet and triplet structures are genuinely independent and must both be included in the operator basis.

The other class of operators used in this thesis is of the form $\psi^2 H^2 D$, consisting of two fermion doublets, two Higgs doublets, and a covariant derivative containing the electroweak gauge bosons. The two Higgs fields can form either an isospin singlet or a triplet, leading to two independent sets of operators. These operators involve either two left-handed leptons or two left-handed quarks. For the isospin singlet case, the operators read

$$Q^{(1)}_{\substack{Hl \\ pr}} = (H^\dagger i \overleftrightarrow{D}_\mu H)(\bar{l}_p \gamma^\mu l_r) \ , \tag{2.20}$$

$$Q^{(1)}_{\substack{Hq \\ pr}} = (H^\dagger i \overleftrightarrow{D}_\mu H)(\bar{q}_p \gamma^\mu q_r) \ , \tag{2.21}$$

and for the isospin triplet

$$Q^{(3)}_{\substack{Hl \\ pr}} = (H^\dagger i \overleftrightarrow{D}^I_\mu H)(\bar{l}_p \tau^I \gamma^\mu l_r) \ , \tag{2.22}$$

$$Q^{(3)}_{\substack{Hq \\ pr}} = (H^\dagger i \overleftrightarrow{D}_\mu H)(\bar{q}_p \gamma^\mu q_r) \ . \tag{2.23}$$

Here, the gauge-covariant derivative is defined as

$$D_\mu = I\,\partial_\mu + i g_3 T^A G^A_\mu + i g_2 \frac{\tau^I}{2} W^I_\mu + i g_1 Y B_\mu \tag{2.24}$$

where, T^A are the $SU(3)$ generators, $\tau^I/2$ are the $SU(2)$ generators, Y is the $U(1)$ hypercharge, while B_μ, G^A_μ, and W^I_μ are the gauge fields with corresponding couplings g_1, g_2, g_3. The Higgs field in the unitary gauge is given by $H = \sqrt{1/2}(0,\, h+v)^T$, with $\widetilde{H} = i\tau_2 H^*$. Finally, the combinations of covariant derivatives are given by $\overleftrightarrow{D}_\mu = \overrightarrow{D}_\mu - \overleftarrow{D}_\mu$ and $\overleftrightarrow{D}^I_\mu = \tau^I \overrightarrow{D}_\mu - \overleftarrow{D}_\mu \tau^I$, while the subscripts $p,\ r$ represent flavor indices.

These operators are directly involved in beta decay, as they correct the W-boson interactions with quarks and leptons with either leptons or quarks. In the weak basis, the

operators with flavor indices $p = r = 1$ contribute at tree level. In addition, loop-level insertions of these operators with different flavor indices can contribute to beta decay via quantum corrections.

The presence of the two Higgs fields H^2 ensures gauge invariance under the full electroweak symmetry $SU(2)_L \times U(1)_Y$. After electroweak symmetry breaking, these Higgs fields are replaced by their vacuum expectation values and effectively shift the couplings of the electroweak gauge bosons to fermions. As a result, the W-mediated charged-current interaction relevant for beta decay receives additional contributions, even though no physical Higgs bosons appear as external particles in the process.

To connect the high-energy Standard Model Effective Field Theory (SMEFT) description to low-energy observables, these operators must be evolved down to the experimental scale using renormalization group equations (RGEs). Below the electroweak scale, heavy fields such as the W, Z, top quark, and Higgs boson are integrated out, resulting in the Low-Energy Effective Field Theory (LEFT), which contains only light quarks, leptons, gluons, and photons [147]. This step is essential for incorporating QCD and QED corrections and provides the starting point for the low-energy Lagrangian.

The SMEFT is later used in this thesis in Section 2.1.

2.2 Chiral Perturbation Theory

At energies well below the QCD confinement scale, $\Lambda_\chi \sim 1$ GeV, quarks and gluons are confined inside hadrons, and perturbative QCD methods cannot be applicable. In this non-perturbative regime, it is useful to utilize the approximate symmetries of QCD rather than attempt direct calculations with quark and gluon degrees of freedom.

For the two lightest quarks (up and down), the smallness of their masses compared to Λ_χ gives rise to an approximate chiral symmetry, which turns out to be very useful in describing theory for describing low-energy hadron dynamics [12]. The QCD Lagrangian for these two lightest quark flavors reads

$$\mathcal{L}^{(0)}_{QCD} = -\frac{1}{4}Tr(G_{\mu\nu}G^{\mu\nu}) + i\bar{q}_L\gamma^\mu D_\mu q_L + i\bar{q}_R\gamma^\mu D_\mu q_R - \bar{q}_L M q_R - \bar{q}_R M q_L \ , \tag{2.25}$$

where $q_{L,R} = (1 \mp \gamma_5)q/2$ are respectively left and right quarks, and M is the quark mass

matrix.

$$q = \begin{pmatrix} u \\ \\ d \end{pmatrix} , \qquad M = \begin{pmatrix} m_u & 0 \\ \\ 0 & m_d \end{pmatrix} . \tag{2.26}$$

In the limit of vanishing quark masses $M \to 0$, this Lagrangian exhibits a global $U(2)_L \times U(2)_R$ symmetry, corresponding to independent unitary transformations of the left- and right-handed quark fields. This symmetry can be decomposed into

$$U(2)_L \times U(2)_R = SU(2)_L \times SU(2)_R \times U(1)_V \times U(1)_A \ . \tag{2.27}$$

Here $SU(2)_L \times SU(2)_R$ represents independent isospin rotation of left- and right-handed quarks, under which

$$q_{Li} \to L_{ij} q_{Lj} \ , \quad q_{Rj} \to R_{ij} q_{Rj} \ , \tag{2.28}$$

where R and L are independent SU(2) matrices. $U(1)_V$ is a vector symmetry whose conserved current is the difference between the number of quarks and antiquarks, called baryon number; and $U(1)_A$ corresponds to axial rotations. The $U(1)_A$ symmetry, however, is explicitly broken by the Adler–Bell–Jackiw anomaly [148, 149], leaving the symmetry group

$$SU(2)_L \times SU(2)_R \times U(1)_V \tag{2.29}$$

The $SU(2)_L \times SU(2)_R$ part is not fully realized in the physical spectrum. Instead, only its vector subgroup $SU(2)_V$, defined by transformations where the left- and right-handed rotations are equal (associated with taking $R = L$). This subgroup is known as isospin, under which hadrons can be classified according to their transformation properties: for instance, the proton and neutron form an isospin doublet, while the three pions form an isospin triplet. Isospin symmetry is, however, only approximate, as evidenced by small mass splittings within these multiplets, primarily due to the difference $m_u \neq m_d$ and electromagnetic effects.

The axial supgroup, defined by transformations with $R = L^\dagger$, is not realized in the hadronic spectrum. If this axial symmetry were exact, one would expect hadrons to have degenerated multiplets with opposite parity, which is not observed in experiments. The absence of such degeneracy indicates that the chiral symmetry is spontaneously broken to

its vector subgroup $SU(2)_V$. This spontaneous breaking gives rise to massless Goldstone bosons, identified with the pions in the limit of vanishing quark masses [150].

According to Goldstone's theorem [151, 152], the spontaneous breaking of the global chiral symmetry implies the existence of three massless Nambu–Goldstone bosons, identified with the lightest pseudoscalar mesons, the pions. Their small but nonzero masses originate from the explicit breaking induced by the quark mass matrix in the QCD Lagrangian [12, 153]. The spontaneous symmetry breaking is characterized by a nonvanishing quark condensate, which acts as the order parameter:

$$\langle 0|\bar{q}q|0\rangle \neq 0 \ , \tag{2.30}$$

where q denotes the light quark fields. This object transform as a $(2, \bar{2})$ under $SU(2)_L \times SU(2)_R$

$$\langle 0|\bar{q}_{R_j} q_{L_i}|0\rangle \ \rightarrow \ L_{im} \ \langle 0|\bar{q}_{R_n} q_{L_m}|0\rangle \ R^{\dagger}_{nj} = E^3 (L R^{\dagger})_{ij} = E^3 \ U_{ij} \ , \tag{2.31}$$

here E is a dimensionful parameter and characterizes the strength of the quark condensate. If $L = R$ then $U_{ij} = \delta_{ij}$, and the vacuum preserves the diagonal subgroup $SU(2)_V$ symmetry. In this case, the condensate is invariant under vector transformations and thus leaves the $SU(2)_V$ symmetry unbroken. However, if $L \neq R$ then U_{ij} corresponds to a different vacuum orientation from Eq. (2.31), and if it wasn't for the explicit breaking of $SU(2)_L \times SU(2)_R$ all these vacua would be physically equivalent. In the absence of explicit symmetry-breaking terms—such as the quark mass matrix in the QCD Lagrangian—all such vacua would be physically equivalent, forming a degenerate manifold. The presence of small but nonzero quark masses lifts this degeneracy, explicitly breaking $SU(2)_L \times SU(2)_R$ and selecting a unique vacuum aligned with the mass terms. This is the reason that $< \bar{q}q > \neq 0$, while $< \bar{q}\gamma^5 q >= 0$.

A convenient way to parameterize the vacuum orientation and pion fields is via the unitary matrix

$$U \rightarrow U(x) \equiv \exp(2i\phi(x)/F_\pi) \ , \tag{2.32}$$

where $F_\pi \simeq 92$ MeV is the pion decay constant and

$$\phi(x) = \phi_a(x) T_a = \frac{1}{\sqrt{2}} \begin{pmatrix} \frac{\pi^0}{\sqrt{2}} & \pi^+ \\ \pi^- & -\frac{\pi^0}{\sqrt{2}} \end{pmatrix} , \tag{2.33}$$

collects the pion fields. This provides a natural basis for constructing the chiral effective Lagrangian, however, to do so, one must first specify the transformation properties of $U(x)$ under the chiral group [154]:

$$U(x) \to L U(x) R^\dagger \ . \tag{2.34}$$

2.2.1 The ChPT Lagrangian at the lowest order

At this stage, one may construct the ChPT Lagrangian by following the general strategy used for any effective field theory (EFT) [10, 12, 136]. This involves three key steps: (i) identifying the relevant degrees of freedom, (ii) specifying the symmetries that govern their dynamics, and (iii) determining the small parameter that organizes the perturbative expansion. With these elements specified, one writes down the most general Lagrangian consistent with the symmetries, with interactions ordered according to their importance in powers of the expansion parameter. In the case of ChPT, the relevant degrees of freedom are the pseudo–Nambu–Goldstone bosons, associated with the spontaneous breaking of chiral symmetry, namely the pions, along with other particles whose masses are smaller than the QCD scale $\Lambda_\chi \sim 1$ GeV. These include, for instance, light leptons and, when considering baryonic sectors, nucleons treated within the heavy baryon formalism [155, 156]. The symmetries of the ChPT Lagrangian include the spontaneously broken chiral symmetry. Lorentz symmetry is preserved in the mesonic sector. In the heavy-baryon formulation, Lorentz symmetry is only preserved order-by-order in the EFT expansion at the level of observables. In ChPT, there are three distinct energy regimes: (i) in processes such as beta decay, a low-energy scale appears, corresponding with external momenta q_{ext} of the order of electron mass, $m_e \sim 1$ MeV; (ii) the nuclear scale p, set by the mass of pion m_π, k_F (the typical momentum of nucleon bound in a nucleus), and the pion decay constant $F_\pi \sim 100$ MeV; (iii) the hadronic scale, associated with the QCD scale $\Lambda_\chi \sim m_N \sim 1$ GeV. The ChPT expansion parameter is

given by the ratio of the low to the higher energy scale. This gives the expansion parameters

$$q_{ext} \;<<\; p \;<<\; \Lambda_\chi \;<<\; M_W \;. \tag{2.35}$$

where, $\Lambda_\chi \sim 4\pi F_\pi \sim 1$ GeV.

Therefore, from the hierarchy of energy scales, one can identify three distinct expansion parameters:

$$\epsilon_{recoil} = \mathcal{O}\left(\frac{q_{ext}}{m_\pi}\right) \;, \qquad \epsilon_{\not\pi} = \mathcal{O}\left(\frac{q_{ext}}{\Lambda_\chi}\right) \;, \qquad \epsilon_\chi = \mathcal{O}\left(\frac{p}{\Lambda_\chi}\right) \;. \tag{2.36}$$

For nuclear forces, achieving sub-percent theoretical accuracy requires going beyond the leading chiral interactions and including recoil and electromagnetic effects. For example, accurately describing binding energies requires including $O(\epsilon_\chi)$ corrections.

In electroweak processes such as beta decay, the needed precision calculations involve contribution of order $O(\alpha)$, $O(\alpha\ \epsilon_\chi)$, $O(\alpha\ \epsilon_{recoil})$,$O(\alpha\ \epsilon_{\not\pi})$ as well as selected leading effects at $O(\alpha^2)$, where $\alpha = e^2/(4\pi)$ is the fine-structure constant. As mentioned before, such corrections are required to match the experimental sensitivity at the 10^{-4} level of CKM unitarity tests [27, 157, 158].

With the relevant building blocks identified, one can now construct the ChPT Lagrangian. The degrees of freedom include the pions, collected in the matrix-valued field $U(x)$, and the nucleon isospin doublet

$$N = \begin{pmatrix} p \\ \\ n \end{pmatrix} \tag{2.37}$$

where p and n denote the proton and neutron fields, respectively.

At lowest orders, the Lagrangian separates into mesonic, pion–nucleon, and nucleon–nucleon contributions [12, 102, 103, 111]

$$\mathcal{L}_{\pi\pi} = \frac{1}{2}\partial_\mu\pi\cdot\partial^\mu\pi - \frac{1}{2}M_\pi^2\pi^2 + \frac{1}{2F_\pi^2}(\pi\cdot\partial_\mu\pi)(\pi\cdot\partial^\mu\pi) + \dots \;, \tag{2.38}$$

$$\mathcal{L}_{\pi N} = N^\dagger(i\partial_0 + \frac{\vec{\nabla}^2}{2m})N - \frac{1}{2F_\pi^2}N^\dagger\tau\cdot(\pi\times\dot{\pi})N + \frac{g_A}{2F_\pi}N^\dagger\vec{\sigma}\tau\cdot\vec{\nabla}\pi N + \dots \;, \tag{2.39}$$

$$\mathcal{L}_{NN} = -\frac{1}{2}C_S(N^\dagger N)(N^\dagger N) - \frac{1}{2}C_T(N^\dagger\vec{\sigma}N)(N^\dagger\vec{\sigma}N) + \dots \;, \tag{2.40}$$

where F_π is the pion decay constant, g_A is the nucleon axial-vector coupling, and C_S, C_T are low-energy constants parameterizing short-range nucleon–nucleon interactions.

These terms represent, respectively, the pion dynamics, the leading pion–nucleon couplings, and contact interactions between nucleons. Higher-order corrections, organized by Weinberg's power counting, introduce additional derivatives and pion fields but are suppressed by powers of ∂/Λ_χ.

2.2.2 The Weinberg power counting scheme

Power counting (PC) provides a systematic method to determine which terms in the effective Lagrangian are dominant and to organize calculations in a controlled, order-by-order manner [102, 111, 113]. Specifically, it establishes a hierarchy among operators based on the suppression by powers of a small parameter p/Λ_χ. In addition, PC provides a way to estimate the relative importance of different Feynman diagrams, providing a consistent truncation scheme for nuclear interactions.

For a given diagram, the amplitude scales as

$$\mathcal{A} = \left(\frac{p}{\Lambda}\right)^\nu \ , \tag{2.41}$$

where the power ν is determined from the topology of the diagram and the order of its vertices. Weinberg's analysis yields the formula

$$\nu = \sum_i V_i d_i - 2I_p - I_n + 4L \ , \tag{2.42}$$

- V_i is the number of vertices of type i,
- d_i is the number of derivatives of each vertex,
- I_π and I_N are respectively the numbers of internal pion and nucleon lines,
- L is the number of loops.

The factors -2 for the internal pion line account for the propagator momentum dependence (two powers of momenta in a denominator), and -1 for the internal nucleon line account

for the propagator momentum dependence in heavy baryon ChPT (one power of momenta in a denominator). This formula enables one to assign an unambiguous chiral order to any given diagram, providing the basis for organizing nuclear forces and electroweak operators within ChPT.

Using topology properties of Feynman diagrams Eq. 2.41 can be reformulated in the following useful form, since no internal propagators are taken into account

$$\nu = \sum_i V_i(d_i + \frac{1}{2}n_i - 2) + 2L + 2 - \frac{1}{2}E_n \ , \tag{2.43}$$

where n_i is the number of nucleon fields in the vertex of type i and E_n number of external nucleon lines. For fixed E_n, the expansion proceeds in positive powers, since chiral symmetry imposes the constraint $d_i + \frac{1}{2}n_i - 2 \ \geq \ 0$, which guarantees that no negative powers arise when adding more derivatives of powers of the quark mass in a vertex.

2.2.3 Many body potential

In a system of interacting nucleons, the many-body Hamiltonian can be expressed as the sum of kinetic energy contributions and a hierarchy of interaction terms organized by the number of nucleons involved. This expansion starts with two-body potential and three-body potential, up to n-body potential, where n is the number of nucleons in the system. It reads

$$H = \sum_i T_i + \sum_{i<j} V_{ij} + \sum_{i<j} V_{ijk} + ... \ , \tag{2.44}$$

where T_i is kinetic energy part of the nucleon i, V_{ij} is the two-body potential between nucleons i and j, V_{ijk} is three-body potential between nucleons i, j and k, and so on.

A natural consequence of Weinberg's power counting scheme is that interaction terms involving fewer nucleons are less suppressed in the chiral expansion. As a result, two-body forces appear at the leading order, while three-body forces enter at higher orders and are subleading. Four-body interactions are further suppressed, making them increasingly less important. This hierarchy of interactions is shown in Fig. 2.2 and will be discussed in subsequent sections.

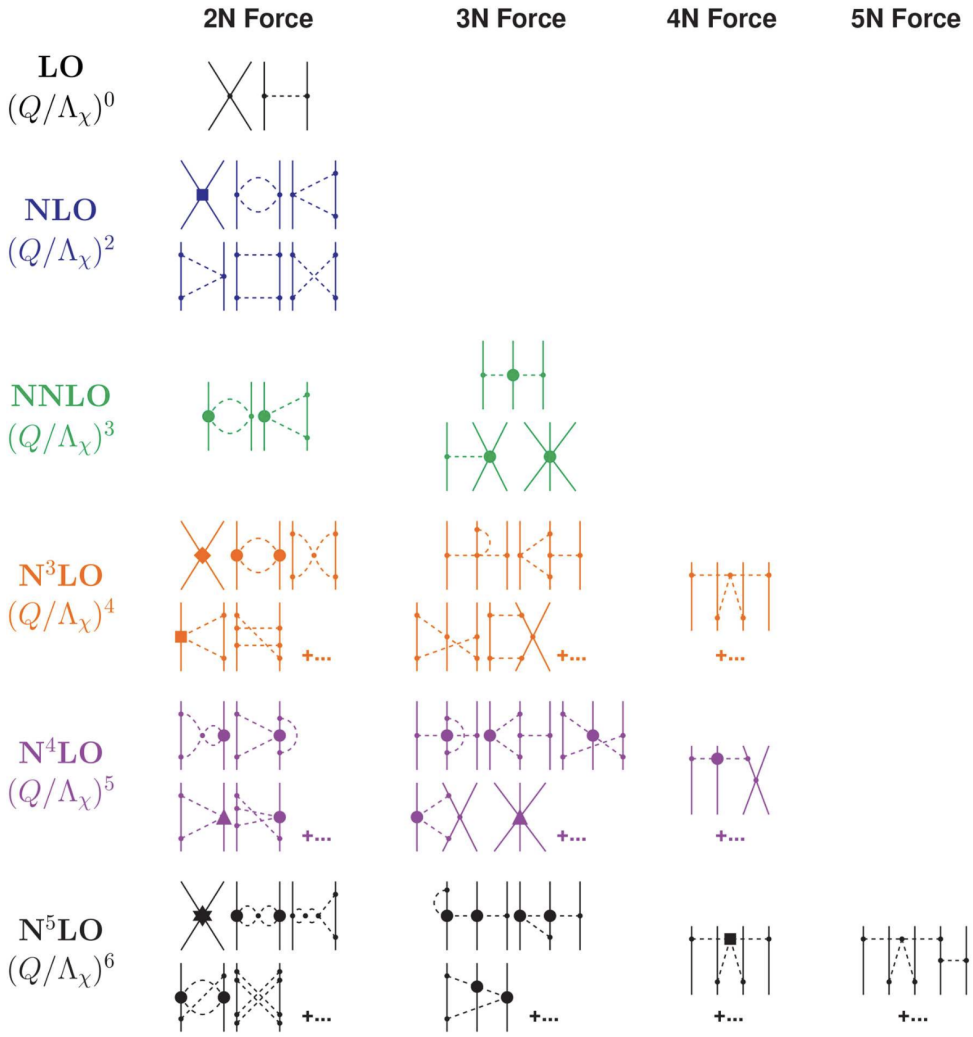

Figure 2.2: Hierarchy of nuclear forces up to N5LO in ChPT. Solid lines represent nucleons and dashed lines represent pions. This figure is taken from [6]

.

Weinberg's approach to construct nuclear forces within Chiral EFT is based on computing the sum of all irreducible diagrams – that means, diagrams which cannot be generated through the Lippmann-Schwinger equation. These irreducible terms define the nuclear potential, which is then inserted into the Lippmann–Schwinger equation to resum the reducible diagrams and obtain the full scattering amplitude [113, 159]. Examples of reducible and ir-

reducible diagrams are shown in Fig. 2.3.

(a) Irreducible diagram

(b) Reducible diagram

Figure 2.3: Irreducible diagrams cannot be separated by cutting only nucleon lines and represent single interaction events. Reducible diagrams can be split by such a cut, corresponding to intermediate nucleonic states, and are generated by iterating the potential in the Lippmann–Schwinger equation.

Eq. (2.42) implies that the leading order of the many-body potential appears for $\nu = 0$. At this order, there are only two distinct topologies contributing to the two-body interaction: a contact interaction without derivatives and a one-pion exchange (OPE) diagram. In momentum space, the resulting potential is given by

$$V_0 = C_S + C_T \vec{\sigma}_1 \cdot \vec{\sigma}_2 - \frac{g_A^2}{4F_\pi^2} \frac{(\vec{q} \cdot \vec{\sigma}_1 \vec{q} \cdot \vec{\sigma}_2)(\vec{\tau}_1 \cdot \vec{\tau}_2)}{\vec{q}^2 + m_\pi^2} \ , \tag{2.45}$$

where the indices 1 and 2 label the nucleons, $g_A \simeq 1.25$ is the axial coupling constant, $F_\pi \simeq 186$ MeV is the pion decay constant here, and $\vec{\sigma}$ and $\vec{\tau}$ are the spin and isospin operators. The low-energy constants C_S and C_T parameterize short-range physics in the spin-independent and spin-dependent channels, respectively, with no momentum dependence. These LECs are not determined by symmetry, and must be fixed from experiments such as the NN phase shift [115, 160].

For the S-wave channels, the spin and isospin projectors allow the momentum-independent contact interaction to be expressed in terms of two independent combinations of the low-energy constants C_S and C_T. For the spin-singlet channel ($^1S_0$), the spin operator satisfies $\vec{\sigma}_1 \cdot \vec{\sigma}_2 = -3$, yielding the effective contact interaction

$$C_0^{^1S_0} = C_S - 3C_T \ . \tag{2.46}$$

For the spin-triplet channel ($^3S_1$), one has $\vec{\sigma}_1 \cdot \vec{\sigma}_2 = 1$ leading to

$$C_0^{^3S_1} = C_S + C_T \ . \tag{2.47}$$

These two combinations parameterize all leading-order short-range effects in the S-wave channels, while the one-pion exchange term in Eq.(2.45) provides the dominant long-range contribution [113]. The contact interaction C_0 is of order $4\pi/(m_N Q)$, which is of the same order as the one-pion exchange term, proportional to $1/F_\pi^2$.

2.2.4 Three-nucleon forces

As illustrated in Fig. 2.2, there are no contributions to the three-nucleon force at next-to-leading order (NLO). It was shown in Ref. [113] that all potential contributions at this order vanish.

Therefore, the leading 3N forces appears at the next-to-next-to-leading order ($\mathrm{N^2LO}$) in the EFT expansion [114, 161, 162]. These contributions are shown in Fig 2.4. At this order, the 3N force consists of (i) a long-range contribution in which two pions are exchanged between nucleons, (ii) an intermediate-range one-pion exchange interaction, and (iii) a short-range contribution. The LECs associated with the intermediate- and short-range topologies, called c_D and c_E respectively, can be fit to several observables, including the binding energies and radii of tritium and helium, the tritium decay rate, $n-d$ scattering, or by using heavier nuclei or saturation properties [133, 162–166]. Interestingly, the LECs associated with the leading long-range part of the 3N force, which is well known as the Fujita Miyazawa force [167], can be determined by the analysis of pion-nucleon scattering in Chiral perturbation theory and do not rely on data from multi-nucleon systems.

The momentum-space potentials associated with the one-pion-exchange contact and the pure contact 3N force topologies are given by

$$V_D = -\frac{g_A}{8F_\pi^2}\frac{c_D}{F_\pi^2\Lambda_\chi}\sum_{i\neq j\neq k}\frac{\sigma_j\cdot\vec{q}_j}{q_j^2+m_\pi^2}(\vec{\tau}_i\cdot\vec{\tau}_j)(\vec{\sigma}_i\cdot\vec{q}_j)\ , \tag{2.48}$$

$$V_E = \frac{c_E}{2F_\pi^4\Lambda_\chi}\sum_{j\neq k}(\tau_j\cdot\tau_k)\ . \tag{2.49}$$

The low-energy constants $c_1,\ c_3,$ and c_4, which are associated with long-range two-pion exchange interactions, are the only LECs from the three-nucleon force that contribute to pure neutron matter at N2LO. These LECs are well-known and determined by pion-nucleon scattering data, being well constrained independently of multi-nucleon data [168, 169]. As a result, their uncertainties are relatively small, and their impact on observables in neutron-rich systems, such as the equation of state for neutron matter, is particularly robust. The momentum-space potential arising from this long-range two-pion exchange takes the form

$$V_c = \frac{1}{2}\left(\frac{g_A}{2F_\pi}\right)^2\sum_{i\neq j\neq k}\frac{(\vec{\sigma}_i\cdot\vec{q}_i)(\vec{\sigma}_j\cdot\vec{q}_j)}{(q_i^2+m_\pi)(q_j^2+m_\pi)}F_{ijk}^{\alpha\beta}\tau_i^\alpha\tau_i^\beta\ , \tag{2.50}$$

where

$$F_{ijk}^{\alpha\beta} = \delta^{\alpha\beta}[-\frac{4c_1m_\pi^2}{F_\pi^2}+\frac{2c_3}{F_\pi^2}\vec{q}_i\cdot\vec{q}_j]+\sum_\gamma\frac{c_4}{F_\pi^2}\epsilon^{\alpha\beta\gamma}\tau_k^\gamma\vec{\sigma}_k\cdot(\vec{q}_i\times\vec{q}_j)\ . \tag{2.51}$$

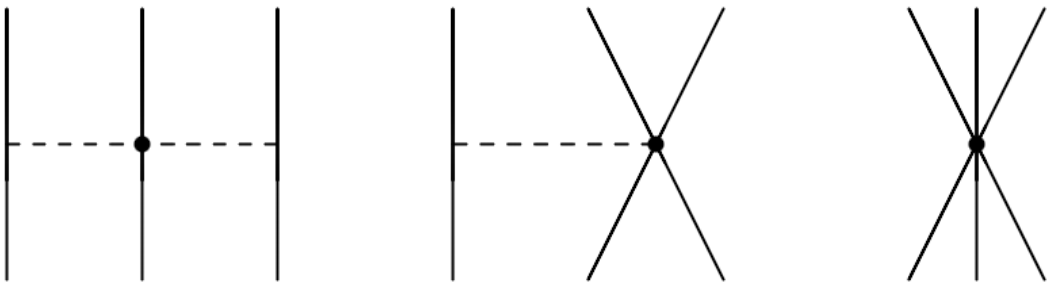

(a) Two-pion exchange (b) One-pion exchange (c) Contact term

Figure 2.4: Feynman diagrams of the leading three-nucleon force at next-to-next-to-leading order (N2LO) in chiral effective field theory.

At next-to-next-to-next-to-leading order (N3LO) additional topologies contribute to the 3N force, as illustrated in Fig 2.2. Importantly, no new LECs are introduced in this order that require additional constraints. All contributions are fully determined by parameters fixed at lower orders, along with loop diagrams that arise within the chiral expansion.

Chapter 3

BETA DECAY

3.1 Neutron lifetime experiment

In the Section 1.1.1 we discussed the history of beta decay. In this section, we focus on the most precise result of measurement of the neutron lifetime τ_n [19] using the $UCN\tau$ apparatus at the Los Alamos Neutron Science Center, and present the result together with the description of the apparatus and the method.

The decay $n \to p + e^- + \bar{\nu}_e$ is the simplest example of β-decay involving baryons. The mean neutron lifetime τ_n provides a key input for predicting primordial light element abundances [170]. The lifetime, combined with decay correlations, tests the V-A structure of the weak interaction in the standard model (SM) at low energy while avoiding nuclear structure corrections [171]. Recent and forthcoming neutron β-decay experiments can be used to extract the magnitude of the Cabibbo-Kobayashi-Maskawa (CKM) matrix element V_{ud} with a precision approaching that from studies of superallowed $0^+ \to 0^+$ nuclear transitions. Furthermore, these tests can probe beyond the SM interactions at energy scales higher than 10 TeV, which are hard to detect at colliders [172, 173].

The so-called inner electroweak radiative correction to τ_n contains model-dependent hadronic structure and short-distance QCD physics and is the dominant source of theoretical uncertainty in the prediction [174]. A recent re-assessment of the inner correction using a data-driven dispersion relation approach shifts the value of $|V_{ud}|$ extracted from superallowed $0^+ \to 0^+$ decays resulting in a $\sim 3\sigma$ deviation from unitarity in the top row of the CKM matrix [175–177]. This tension between the standard model and experiments has sparked a renewed urgency to independently examine these corrections. Studies of neutron decay, with increasing precision, are becoming a theoretically and experimentally robust standard model test [176, 177].

3.1.1 UCNτ method

A significant part of this thesis is devoted to the most precise neutron lifetime measurement performed by the UCNτ collaboration [19], of which I was a member. My contributions to this effort included performing Monte Carlo simulations with the *PENTrack*, assisting in the construction and commissioning of the experimental apparatus, and contributing to the data analysis, in particular the search for sidereal modulations in the neutron lifetime.

The used apparatus is shown in Fig. 3.1. The Ultra Cold Neutrons are produced in the Los Alamos Neutron Science Center's proton- beam-driven solid deuterium UCN source [178], and they are pumped to the apparatus from the left side of the sketch, with kinetic energy lower than $E < 180$ neV. The important feature of UCNs for the theoretical analysis is that they are polarized by a 5.5 T superconducting solenoid, spin-flipped into the trappable low-field-seeking spin state using an adiabatic fast-passage spin flipper [179] and loaded into the UCNτ bowl-shaped Halbach array [180] over $t_{load} = 150$ s.

A Halbach array is a specific arrangement of permanent magnets shaped like an asymmetric bathtub, in which the magnetization direction of each element is rotated relative to its neighbors. This configuration creates an asymmetric magnetic field that increases with the distance from the bathtub center, forming a magneto-gravitational potential well trapping neutrons [181].

Once the UCNs are loaded into the magneto-gravitational trap, the bottom of the Halbach array is closed. The arrangement and shape of the electromagnetic coils, which provide magnetic field prevents UCNs from depolarizing. Then neutrons with kinetic energy $E > 38$ neV are removed from the apparatus [7, 182–184]. The potential of this trap is quite shallow and equal to $V_T \sim 50$ neV. The UCNs remain stored in the trap for an additional 20 to 1550 s. This is why this approach is known as the "bottle" method, as neutrons live and die within the magnetic walls of the trap, and meet their inevitable decay, as though imprisoned in a bottle. During this whole time, neutrons decay and at the end the surviving neutrons are counted by ^{10}B-coated-ZnS scintillator UCN counter [184] in 210 s intervals. Simultaneously, the higher-energetic neutrons are still being removed from the array, preventing any ultracold neutrons from escaping the trap.

A key feature of the experiment, crucial both for standard neutron lifetime measurements and for searches for physics BSM, is the use of two storage cycles – short ($t_{store} \leq 500$ s) and long ($t_{store} \geq 500$ s). Thanks to that, one can extract the neutron lifetime τ_n

$$\tau_n = \frac{t_l - t_s}{\log(Y_s/Y_l)} \ , \tag{3.1}$$

where t_s (t_l) denotes short (long) time of the run, while $Y_i = (D_i - B_i)$ is the number of neutrons remaining after storage time t_i. The choice of storage times should be relatively close to one another, ensuring sensitivity to potential annual or sidereal variations in the neutron decay rate.

UCNs in the loading volume are monitored by four ^{10}B-coated ZnS detectors (M1-M4 in Fig 3.1) coupled to PMTs [185]. These detectors normalize primary counter data, correcting for changes in UCN source intensity and spectrum, which can vary with source heat load and crystal quality [186]. Their signals are processed with thresholds that reject background, and all channels are recorded by a 1.25 GHz scaler.

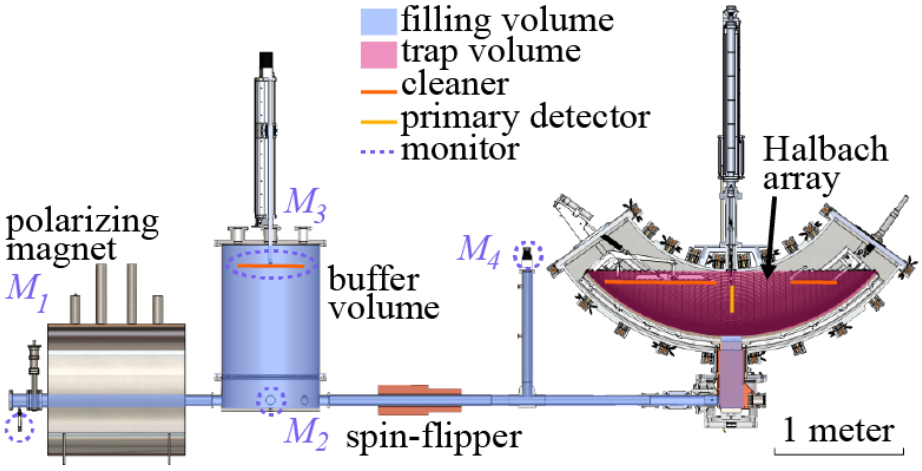

Figure 3.1: The scheme of the UCNτ apparatus configuration, with the volumes occupied by UCNs, cleaner surfaces, primary detector, and monitors highlighted. The polarizing magnet selects the high-field-seeking UCNs. UCNs are then "precleaned" in the buffer volume, spin-flipped to the trappable low-field-seeking spin state, and loaded into the trap. The 2017 configuration was the same as that of Ref. [7].

Data analysis

We performed three analyses A, B, and C. Initially, no extracted values of τ_n were shared between analyzers, so that analyses developed separately and the data were blinded by shifting τ_n within a ± 15 s window, by the same factor. After sharing blinded values, we performed run-by-run comparisons of extracted monitor counts, primary detector counts, and background estimates between analyzers. The data were unblinded when the three extracted τ_n values agreed to within 0.1 s. Each analysis separately assessed systematic effects and potential statistical biases.

All analyses proceeded in the following stages. Run quality criteria are developed to reject runs with poor or abnormal experimental conditions. For each remaining run j, primary detector events are formed. These events and monitor counts are time binned as in Fig. 3.2, and rate-dependent corrections are applied to counts in each bin. Corrected primary detector counts $d_j(t)$ are summed during the counting phase to give an UCN signal D_j. A combination of the rates from background runs proximal in time to j, as well as counts during storage and after counting, are used to estimate background counts B_j during the three counting stages. The monitor detector counts $m_{k,j}(t)$ are time weighted by a function $w(t)$ and summed for $0 < t < t_{\text{fill}}$ to find monitor signals $M_{k,j}$. These are reduced to a single normalization factor using a regression model $f\left(M_{k,j}\right) \rightarrow N_j$. The quantities D_j, B_j, and N_j are then used to find τ_n as discussed below.

Analyses identified and removed runs with significant fluctuations of the LANSCE proton beam during filling and excessive electronic noise while moving the cleaners and primary detector.

An UCN event in the primary detector is characterized by the presence of coincident single photoelectron (PE) between the two primary counters (PMTs) within time t_c (ranging from 50 to 100 ns among analyzers). Thereafter, subsequent PE are counted for a time t_w ranging from 600 to 1400 ns, and this time window is extended if additional PEs are found in the current window. Total counting times vary between $t_{\text{event}} \sim 500$ and 4000 ns. Analysis A (B) requires $n_p \geq 8$ (6) PEs in an initial 1000 ns (600 ns) window. All analyses varied these parameters to test the sensitivity of τ_n. Reference [7] used the raw PE rates (referred to as

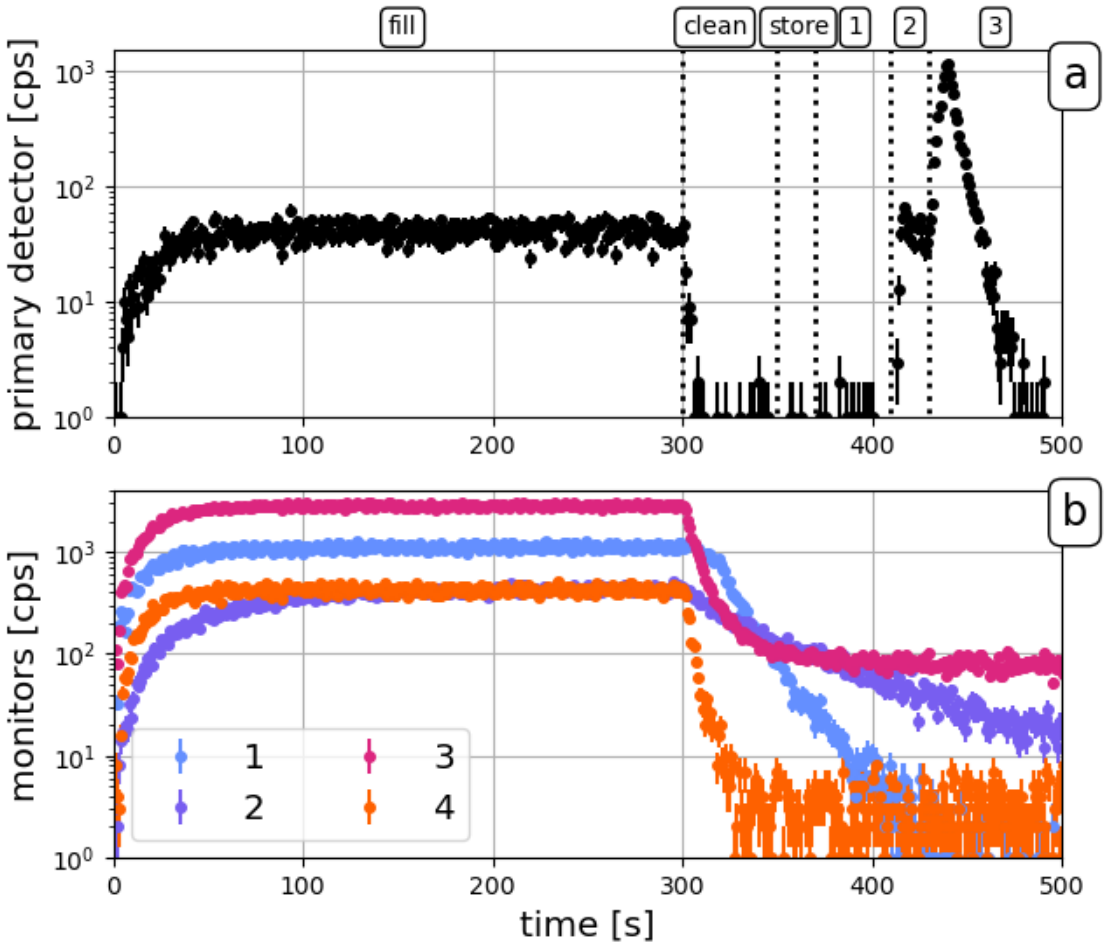

Figure 3.2: (a) Primary detector coincidence counts from analysis A for a typical $t_{\text{store}} = 20$ s run cycle. From left to right, the dotted vertical lines mark the time windows for filling, cleaning, storing, and three counting stages. (b) The count rate during the run cycle for the monitors deployed in the 2018 analysis.

Analysis	$w(t)$	f	Comments
A	$\exp(\kappa t)$	$c_{1\mathrm{A}}M_{l,j} + c_{2\mathrm{A}}M_{u,j}$	$l = 1(2)$ and $u = 4(3)$ in 2017 (2018)
B	$\left[1+\exp\left(-\frac{t-(t_{\mathrm{fill}}/\alpha)}{t_{\mathrm{fill}}/\beta}\right)\right]^{-1}$	$c_{0B} + c_{1\mathrm{B}}\tilde{M}_{1,j} + c_{2\mathrm{B}}\tilde{M}_{2,j}$	$\alpha = 2$, $\beta = 10$, $\tilde{M}_{k,j}$ from PCA of z-scored $M_{k,j}$
C	$\sum_{m=1}^{20} A_m U\left(t\middle\vert(m-1)t_{\mathrm{fill}}, mt_{\mathrm{fill}}\right)$	$c_{1\mathrm{C}}M_{l,j} + c_{2\mathrm{C}}M_{u,j}$	A_m chosen to minimize variance in $M_{k,j}$

Table 3.1: The monitor detector weighting functions $w(t)$ and function $f(M_{k,j})$ used to find run-by-run normalization factor N_j. Analysis B z-scores the $M_{k,j}$ over a range of j and performs a principal component analysis (PCA) to find the two dominant principal components $\tilde{M}_{1/2,j}$. $U(t|a,b)$ is the uniform distribution over (a,b). Note that the coefficients c vary over different subsets of runs (see text).

a "singles analysis" therein) to determine the number of UCNs, which had the advantage of smaller rate-dependent effects and the disadvantage of poorer signal to background. This treatment is inappropriate for the current data due to slow drifts in single PE background rates over the course of the measurement campaign.

This coincidence method gives signal to background for short t_{store} runs as high as 10^3. However, ZnS[Ag]'s long scintillation time constants makes this method subject to rate-dependent systematic effects from dead time, pileup, and accidental event retriggering due to delayed scintillation light. Analysis C maintained a time-averaged rate from previous UCN events within a given run and varied n_p event by event using the known time distribution of the ZnS scintillation. This reduces the possibility of a previous event contributing delayed PEs to the current event, thereby selecting an otherwise underthreshold event. Upon time binning events during t_{count}, analysis C tabulates the sum of t_{event} in each bin and performs an analytic correction to the number of counts in the bin as a function of instantaneous event rate. Analyses A and B used the measured ZnS scintillation time dependence and typical UCN count rates to generate pseudo-datasets. These pseudo-data were analyzed and compared to the true number of simulated counts to develop corrections for rate-dependent effects.

The choices of $w(t)$ and $f(M_{k,j})$ for each analysis are given in Table 3.1. In general, the

given choices of $w(t)$ deweight counts early in the filling phase, which better predicts the number of trapped UCNs. Indeed, because the duration of the filling phase is several times longer than the characteristic time for UCNs to fill the guides and apparatus, a fluctuation in UCN source output occurring early in the filling phase is less likely to influence the number occupying the trap by time t_{fill}. Runs are generally grouped into week- or month-long subsets between melt and refreezes and other discrete changes to the apparatus or the source. The coefficients c thus vary among subsets. Analysis B uses a principal component analysis of the z-scored monitor signals for all monitors [187]. In practice, two components dominate and are used in the normalization: the first component tracks the coarse, overall changes in source output, while the second captures changes in the relative amount of trappable lower-energy UCNs compared to untrappable higher-energy UCNs.

As was done in Ref. [7], all analyses use the mean arrival time $\bar{t}_j = \int t d_j(t) dt$ over the counting phase rather than the nominal t_{store}. This corrects for potential run-by-run or t_{store}-dependent variation of the characteristic timescale with which UCNs are absorbed by the primary detector during counting. Using the nominal t_{store} shifts τ_n by 0.01–0.03 s.

Extraction of τ_n. We determine τ_n by both a "paired" and a "global" analysis. In the former, pairs of short ($j \equiv s$) and long ($j \equiv l$) storage time runs proximal in time are used to compute Eq. (3.1). A bias-corrected weighted average over pairs p gives the final result. This method is less sensitive to potential time drifts in backgrounds or detector response. However, the paired method is less statistically sensitive to τ_n than the global method discussed below, as the pairing process reduces the number of runs used in the analyses. This method finds τ_n in agreement with that of the global analysis.

The global method instead maximizes the likelihood of observing the data $\mathbf{O} = \{D_j, B_j, M_{k,j}, \bar{t}_j\}$ given parameters τ_n, $\mathbf{p}$:

$$\mathcal{L}\left(\mathbf{O}|\tau_n, \mathbf{p}\right) = \prod_j \mathcal{P}\left(\lambda_j, \mathbf{p}|\mathbf{O}\right) \prod_h \pi_{h,j}\left(p_{h,j}\right) \tag{3.2}$$

with $\lambda_j = \tau_n^{-1} + \lambda_{\text{up},j} + \lambda_{\text{dp}} + \lambda_{\text{escape}}$ the loss rate including β decay, residual gas up-scattering rate $\lambda_{\text{up},j}$, depolarization rate λ_{dp}, and escape rate λ_{escape} described below. The probability distribution $\mathcal{P}$, the collection of nuisance parameters $\mathbf{p}$, and their constraints $\pi(p_h)$ vary

Effect	Correction	uncertainty
UCN event definition	...	± 0.13
Normalization weighting	...	± 0.06
Depolarization	...	$+0.07$
Uncleaned UCN	...	$+0.11$
Heated UCN	...	$+0.08$
Al block	$+0.06$	± 0.05
Residual gas scattering	$+0.11$	± 0.06
Uncorrelated sum	$0.17^{+0.22}_{-0.16}$ s	

Table 3.2: Systematic corrections with uncertainties to τ_n in seconds. The total is an uncorrelated combination of all systematic corrections. The non-zero corrections here are applied to the final result. Only the UCN event definition and normalization effects can decrease the measured τ_n.

between analyses. Analysis A computed the Poisson-distributed probability of observing the primary detector counts D_j for a predicted mean number of counts $N_j \exp(-\lambda \bar{t}_j) + B_j$. The `EMCEE` Markov-chain Monte Carlo algorithm [188] was used to marginalize over $c_{1A,j}$, $c_{2A,j}$, and B_j to find τ_n with uncertainty [189]. Analysis B modeled the D_j as quasi-Poisson distributed [190] with the parameters in the normalization model and extra scaling parameter in the variance to account for non-statistical fluctuations treated as free nuisance parameters. A profile likelihood provides τ_n with uncertainty [191]. Analysis C instead minimizes the χ^2 of the yields Y_j with uncertainties over τ_n, normalization parameters, and a free scaling parameter in the variance of the yields. Correlations in the parameter uncertainties are

incorporated to find τ_n with uncertainty.

Systematic effects. All systematic corrections and their uncertainties are summarized in Table 3.2. During 2017, accounting for $\sim 34\%$ of the full dataset, a block-shaped $2.5 \times 2.5 \times 1.3$ cm^3 aluminum structural component from one of the cleaning surfaces fell into the trapping volume, leading to an additional loss channel for UCNs due to up-scattering and absorption on the Al surface. The effect of the aluminum block's additional material loss was assessed in a separate, dedicated run wherein the block was covered in polyethylene foil and reinserted into the same location in the trap. Polyethylene up scatters virtually all UCNs incident upon the surface, thus providing an estimate of the rate of UCNs impinging upon the aluminum block. This introduces an additional ~ 424 s decay component to the yields Y_j versus $\bar{t}_j$. Analysis B uses an estimate of UCN velocity-and-angle-averaged loss per bounce of $(2 \pm 1) \times 10^{-4}$ for aluminum, leading to a 0.15 ± 0.07 s correction to this subset of data. The other analyses perform similar assessments, and independent checks using our Monte Carlo framework [192] are consistent with this estimate. Further, this is consistent with a comparison of paired τ_n during this period to the rest of the paired τ_n values. The value in Table 3.2 is this correction's contribution to the final τ_n for all data.

If UCNs with $E > 51$ neV (corresponding to the 50 cm height of the trap) are not removed during the cleaning phase, and yet reside in the trap for times $\lambda_{\text{escape}}^{-1}$ similar to τ_n before escaping, the extracted τ_n will be systematically lower. Data were obtained in 2018 wherein the cleaner was never lowered into the trap. For these runs, the cleaner detector and primary detector both register counts at positions above the cleaning height during the counting phase, and the extracted τ_n lowered by ~ 15 s, implying an escape rate $\lambda_{\text{escape}} = 2 \times 10^{-5}$ s^{-1}. Assuming a linear relation between λ_{escape} and observed counts in either the cleaner or primary detector, we use the nonobservation of counts in the first counting phase in the primary datasets to constrain the size of the effect. Similarly, as was done in Ref. [7], the nonobservation of counts at the highest primary detector position for $t_{\text{store}} > 500$ s runs in the primary data are used to constrain the effect of initially trappable UCNs, increasing their total energy due to vibration of the Halbach array or any other time dependence in the trapping potential.

The choice of UCN event definition can change the extracted τ_n. Each analysis reextracted τ_n for a range of n_p, t_w, and any other adjustable parameters to assess the associated systematic uncertainty. The three analyses observe a variance similar in magnitude (see Table 3.2).

The sensitivity of the extracted lifetime to choice of weighting function $w(t)$ was assessed by defining appropriate model parameter ranges consistent with accurately modeling the initially loaded UCN populations (e.g., α, β for analysis B), and varying the parameters within these ranges to probe the effect on the extracted lifetime. Taking the most conservative assessment among analyses results in an uncertainty in the lifetime of 0.090 s in 2017 and 0.047 s in 2018 for a combined uncertainty 0.06 s. The nearly 50% reduction in uncertainty in 2018 is largely due to the buffer volume smoothing over variations in UCN production while filling.

Depolarization and residual gas up-scattering losses and associated uncertainties were treated as in Ref. [7]. The toroidal ambient magnetic field strength is unchanged from Ref. [7], and we assign a depolarization rate of $\lambda_{\mathrm{dp}} = 0.0^{+1.0}_{-0.0} \times 10^{-7}$ s^{-1}. The residual gas up-scattering rate was computed run by run using the measured absolute pressure and periodic residual gas analysis of the trap. The relative amounts of water, air, and hydrocarbon molecules were tracked throughout the run campaigns. The up-scattering rate is computed from these data and from the known UCN-gas molecule cross sections measured in Refs. [193, 194]. We assign a conservative 15% uncertainty on the absolute pressure and cross-section uncertainty on water and air from the uncertainties in Refs. [193, 194]. Because of uncertainty in the relative abundance of hydrocarbons, we apply a 70% uncertainty, which spans the full range of measured cross sections in Refs. [193, 194].

Results. The extracted τ_n values with statistical uncertainties for 2017 and 2018 for the different analyses are shown in Table 3.3. Table 3.2 shows the systematic corrections and most conservative uncertainties among the three analyses. Because of differing run selection, UCN event definition, normalization models, and background estimates, the statistical uncertainties between the analyses are not 100% correlated. We explored multiple ways of averaging the three analyses, with little benefit or difference when using optimized estimator

Analysis	A	B	C
Paired	877.77 ± 0.31	877.87 ± 0.32	877.60 ± 0.29
2017	877.68 ± 0.30	877.78 ± 0.34	877.74 ± 0.33
2018	878.06 ± 0.49	877.80 ± 0.46	877.55 ± 0.55
With Al	877.17 ± 0.38	876.81 ± 0.43	877.69 ± 0.40
Full	877.78 ± 0.26	877.79 ± 0.27	877.69 ± 0.28
Combined	877.75 ± 0.28		

Table 3.3: The resulting τ_n (s) for the three analyses with statistical uncertainties. The first row shows paired results for the full dataset. Below are the global fit results for the 2017 and 2018 subsets, and the subset for which the Al component was present in the trap. "Full" refers to the global maximum likelihood fit of all production data. An unweighted average of the three global analyses and largest uncertainty gives the final result.

averaging procedures (similar to Ref. [195]). Ultimately, as in the previous result [7], we perform an unweighted average of the three central values and choose the largest statistical uncertainty, giving $\tau_n = 877.75 \pm 0.28\ _{\text{stat}} + 0.22/-0.16\ _{\text{syst}}$ s, in agreement with Ref. [7].

With 0.039% total uncertainty, this is the first experiment to determine the neutron lifetime with uncertainty smaller than the average 0.09(2)% shift predicted from recent theoretical work [175–177] on radiative corrections. This result, combined with forthcoming experimental and lattice QCD determinations of the axial coupling constant, will independently probe the disagreement in first-row CKM unitarity while avoiding theoretically complicated nuclear structure corrections required for superallowed nuclear decays.

3.1.2 Neutron lifetime anomaly and neutron lifetime variations

The neutron lifetime anomaly is a discrepancy between the two types of methods measuring neutron lifetime. This is illustrated in Fig. 1.2 The current puzzle [196] due to the discrepancy between "beam" [65] and "bottle" [60, 61, 63, 197–199] methods of τ_n measurement indicates either the existence of new physics leading to a neutron decay channel without protons in the final state or the presence of inadequately assessed or unidentified systematic effects in either of the techniques.

The main differences between these two methods crucial for studying the anomaly are shown in Table 3.4.

The observed anomaly could point to an interaction between neutrons and a background dark sector field or particle. Such a field would establish a preferred reference frame in the universe, which does not coincide with the Earth-based laboratory frame. As the Earth rotates, the orientation of neutron spins or momenta relative to this preferred frame changes continuously. This could also lead to a time-dependent modulation of observables, such as decay rates or spin-precession frequencies, with a sidereal period. In this way, a coupling to the dark sector could manifest itself through daily variations in experimental signals, offering a sensitive probe of new physics beyond the Standard Model.

The observed anomaly could point to an interaction between neutrons and a background dark sector field or particle. Such a field would establish a preferred reference frame in the universe, distinct from the Earth-based laboratory frame. If present, this coupling could also induce characteristic time-dependent modulations in observables—such as decay rates or spin-precession frequencies—arising from the Earth's rotation and the resulting change in the relative orientation of neutron spins or momenta. In this way, the anomaly and possible sidereal modulations represent complementary signatures of a dark sector interaction, offering two independent approaches for probing new physics beyond the Standard Model.

The dark matter interpretation was also briefly examined, in particular through axion-like candidates. However, due to the extremely small coupling constants governing their interactions with neutrons, these scenarios can be excluded as viable explanations. Looking ahead, more exotic dark matter candidates—such as dark matter blobs with stronger effective

couplings—could be considered as alternative possibilities.

Another well-studied framework for interpreting anomalies is the Standard Model Extension (SME). The SME provides a systematic, effective field theory description of all possible Lorentz- and CPT-violating operators that can be added to the Standard Model [200]. For neutron physics, such effects could lead to observable consequences in beta decay rates, spin-precession experiments, or storage-lifetime measurements, depending on the type and size of the SME coefficients. Importantly, the SME allows one to formulate model-independent searches, where experimental observables can be mapped directly onto well-defined operator coefficients. In this way, the SME offers a systematic path to constrain possible Lorentz- and CPT-violating effects that could underlie the observed discrepancies.

An example of how an external background field could affect neutron beta decay is through modifications of the W^- boson propagator. In the Standard Model, the propagator takes the Lorentz-invariant form proportional to $g_{\mu\nu}$. However, in the presence of Lorentz-violating effects, one can parametrize deviations by introducing an additional tensor $\chi_{\mu\nu}$, such that

$$< W_\mu W_\nu >= \frac{-i}{M_W^2}(g_{\mu\nu} + \chi_{\mu\nu}) \ , \tag{3.3}$$

where tensor $\chi_{\mu\nu}$ encodes possible background-induced symmetry breaking and represents the coupling of the W^- boson to a preferred spacetime direction or structure. Such a modification would propagate directly into the effective four-fermion interaction governing beta decay, leading to potentially measurable deviations in decay rates, angular correlations, or spin-asymmetry parameters.

To model this potential signal, we assume that the neutron lifetime receives a small periodic correction due to interactions with a dark sector. The modified lifetime for a given run i is expressed as:

$$\tau_i^{DM} = \tau \left(1 + a \sin(2\pi \frac{\Upsilon}{P} + \Phi)\right) \ , \tag{3.4}$$

where τ_{DM} is the neutron lifetime with a dark matter correction and τ is the lifetime without the correction, a is the amplitude of the lifetime change due to dark matter interactions, Υ_i is sidereal time for run i, Φ is the phase of the correction, and P is the harmonic period

relating to the sidereal time. The term

$$b = a \sin\left(2\pi \frac{\Upsilon}{P} + \Phi\right) , \tag{3.5}$$

represents the dimensionless fractional correction to the lifetime, with $b \ll 1$. If Y_i^P is the calculated lifetime yield with a periodic correction, the parameters a and Φ as a function of P can be obtained by minimizing the χ^2 function

$$\chi^2 = \sum_i \left(\frac{Y_i - Y_i^P}{\delta_i}\right)^2 , \tag{3.6}$$

where the δ is a variance. The calculated yield as a function of holding time is given by

$$Y_i^{cal} = \exp \frac{-T_i}{\tau_n} , \tag{3.7}$$

where T_i is the holding time for run i. To investigate this possibility, a sinusoidal function (Eq. (3.4)) was fit to neutron lifetime values from data presented above. Results show a significant peak in the amplitude of the lifetime variation as large as

$$a = 1.34 \pm 0.28s . \tag{3.8}$$

This result could be a hint of an interaction between neutrons and a background dark sector field or particle, modulated by Earth's rotation relative to the dark sector frame. Further investigation with higher statistics and improved control of systematics is necessary to assess the robustness of this potential signal.

3.1.3 Possible BSM explanations

A long-standing discrepancy of approximately 10 seconds exists between the neutron lifetime measured using the "beam" method and the "bottle" method. One intriguing possibility is that this difference arises from neutron decays into final states involving particles beyond the Standard Model (BSM), which would evade detection in beam experiments that only count β-decay products. In such scenarios, the total decay rate of the neutron is the sum of the Standard Model beta-decay rate and an additional BSM decay rate:

$$\frac{1}{\tau_n^{total}} = \frac{1}{\tau_\beta} + \frac{1}{\tau_{\mathrm{BSM}}} , \tag{3.9}$$

Table 3.4: Comparison of the bottle and beam methods for measuring the neutron lifetime.

Aspect	**Bottle Method**	**Beam Method**
Principle	Traps ultracold neutrons (UCNs) and counts how many survive after a given time.	Counts decay products (usually protons) from a well-defined neutron beam.
Measured Quantity	Surviving neutrons as a function of time.	Number of decay protons per neutron.
Neutron Source	Ultracold neutrons stored in a physical or magnetic trap.	Cold neutron beam from a reactor or spallation source.
Strengths	Direct measurement of neutron disappearance. Long storage times possible.	Independent of UCN storage systematics. High statistics possible.
Systematic Challenges	Losses due to wall collisions or magnetic field imperfections. Requires extrapolation to ideal trap.	Requires precise knowledge of neutron flux and detection efficiency.
Typical Lifetime Measured	Around 878–880 s.	Around 888–890 s.
Discrepancy	suggests a possible missing decay channel or underestimated systematics.	Consistently higher than bottle method by ∼8–10 s.

where τ_n^{total} is the total neutron lifetime (as measured in bottle experiments), τ_β is the beta-decay lifetime (as measured in beam experiments), and τ_{BSM} corresponds to the lifetime

associated with non-standard decay channels.

Recent theoretical work has proposed that the discrepancy between the neutron lifetimes measured by bottle and beam methods may originate from non-standard decay channels. Fornal and Grinstein first suggested that neutrons could decay into undetected dark matter particles, providing a natural explanation for the shorter lifetimes observed in bottle experiments. [201]. Following this idea, Cline and Cornell explored the possibility of neutron decay into a dark Dirac fermion χ and a dark photon A', further enriching the landscape of exotic decay modes [202].

If such dark decay modes are indeed allowed, they should also occur in certain nuclei, particularly those with low neutron separation energies. Pfutzner and Riisager [203] identified the neutron-rich nucleus ^{11}Be as a promising candidate for such studies, noting that the βp decay channel of ^{11}Be behaves effectively as a quasi-free neutron decay.

Experimental searches, however, have placed stringent constraints on these hypothetical decay modes. Two independent groups have excluded the radiative decay mode $n \to \chi + \gamma$ with 97% confidence [204], and have ruled out a contribution greater than 1% to the decay mode $n \to \chi + e^+e^-$. at the 95% confidence level [205]. In parallel, Dubbers et al [206] have argued that the neutron lifetime anomaly is unlikely to be explained by exotic decay channels, based on both theoretical considerations and experimental data.

While these beyond-the-Standard-Model explanations are theoretically appealing, the neutron lifetime discrepancy is more plausibly attributed to unresolved systematic effects in the two experimental techniques. In beam experiments, for instance, protons produced by neutron decay may be lost due to charge-exchange collisions with residual gas in the magnetic trap, resulting in an overestimation of the lifetime. In bottle experiments, it has been proposed that the inverse quantum Zeno effect (IZE)—where repeated measurements can accelerate decay—might lead to artificially shortened neutron lifetimes [199].

An alternative explanation involves the so-called mirror matter theory, which postulates the existence of a hidden sector consisting of mirror counterparts to all Standard Model particles. Originally introduced as a solution to the dark matter problem, this framework has been revisited in the context of the neutron lifetime puzzle. In this scenario, approximately 1% of ordinary neutrons oscillate into mirror neutrons, which subsequently decay via $n' \to$

$p'e'\bar{\nu}'$ [207]. What is particularly compelling about this model is that the neutron oscillation serves as the sole bridge between the visible and mirror sectors, enabling matter exchange despite the absence of other interactions.

Ultimately, resolving this discrepancy will require the development of new experimental methods capable of eliminating or controlling these sources of systematic uncertainty. Improved measurements will be essential to determine whether the neutron lifetime anomaly reflects novel physics or experimental artifacts.

3.2 SMEFT

The second crucial component in fully leveraging beta decays as probes of BSM physics—thereby making full use of the results in Section 3.1—is the advancement of theoretical frameworks capable of accommodating potential new-physics effects. For that, we use SMEFT described in Sec. 2.1. We identify the SMEFT operators that induce the largest loop-level contributions to charged-current processes. These include four-quark and four-fermion semileptonic operators involving two third-generation quarks.

3.2.1 Formalism

The Standard Model EFT Lagrangian consists of the $SU(3)_C \times SU(2)_L \times U(1)_Y$-invariant operators incorporating the Standard Model fields. It contains the Standard Model Lagrangian $\mathcal{L}_{\text{SM}}$ along with higher-dimensional operators that capture the effects of heavy degrees of freedom with masses greater than Λ. Focusing on dimension-6 operators, we have

$$\mathcal{L}_{\text{SMEFT}} = \mathcal{L}_{\text{SM}} + \frac{1}{v^2}\sum_k C_k^{(6)} Q_k^{(6)} \ . \tag{3.10}$$

Here $Q_k^{(i)}$ denotes all possible operators of canonical dimension i and $C_k^{(i)}$ are the corresponding Wilson coefficients. For convenience, we have defined the coefficients to be dimensionless, so that they scale as $C_k^{(i)} \sim v^{4-i}/\Lambda^{4-i}$, where $v \simeq 246$ GeV is the Higgs vacuum expectation value. In this work, we exclusively focus on dimension-6 operators, as higher-order operators are further suppressed by higher powers of $1/\Lambda$, making their contributions less significant relative to those of dimension six. Our approach includes a general flavor structure and employs the so-called Warsaw basis [17], which contains 2499 independent operators [146].

The SMEFT Lagrangian is written in a weak eigenstate basis, where the fermion mass matrices are not diagonal. We work in the weak basis in which the mass matrices take the form [208] [1]

$$M_u = \text{diag}(m_u, m_c, m_t) \ , \ M_d = \text{diag}(m_d, m_s, m_b) \cdot V^\dagger \ , \ M_e = \text{diag}(m_e, m_\mu, m_\tau) \ , \quad (3.11)$$

where V is the unitary CKM matrix. In this basis, the left-handed down-type quarks flavor fields are given by Vd_L in terms of the CKM matrix V and the mass eigenfields d_L. Hence, the fermion fields can be written in terms of the mass eigenstate fields as follows

$$q_i = \begin{pmatrix} u_L \\ \\ Vd_L \end{pmatrix}_i , \qquad l_i = \begin{pmatrix} \nu_L \\ \\ e_L \end{pmatrix}_i , \qquad u_i = u_{R_i}, \qquad d_i = d_{R_i}, \qquad e_i = e_{R_i} \ .$$

As discussed in Chapter 2, the complete set of dimension-six SMEFT operators contributing to β decay (and more generally to semileptonic CC processes) at tree level is given by [25]

Four-fermion operators:

$$Q^{(3)}_{\substack{lq \\ prst}} = (\bar{l}_p \gamma_\mu \tau^I l_r)(\bar{q}_s \gamma^\mu \tau^I q_t)$$

$$Q_{\substack{ledq \\ prst}} = (\bar{l}^j_p e_r)(\bar{d}_s q_{tj})$$

$$Q^{(1)}_{\substack{lequ \\ prst}} = (\bar{l}^j_p e_r)\epsilon_{jk}(\bar{q}^k_s u_t)$$

$$Q^{(3)}_{\substack{lequ \\ prst}} = (\bar{l}^j_p \sigma_{\mu\nu} e_r)\epsilon_{jk}(\bar{q}^k_s \sigma^{\mu\nu} u_t) \ .$$

Vertex corrections:

$$Q^{(3)}_{\substack{Hl \\ pr}} = (H^\dagger i \overleftrightarrow{D}^I_\mu H)(\bar{l}_p \tau^I \gamma^\mu l_r) \quad (3.12a)$$

$$Q^{(3)}_{\substack{Hq \\ pr}} = (H^\dagger i \overleftrightarrow{D}_\mu H)(\bar{q}_p \gamma^\mu q_r) \quad (3.12b)$$

$$Q_{\substack{Hud \\ pr}} = i(\widetilde{H}^\dagger D_\mu H)(\bar{u}_p \gamma^\mu d_r) \quad (3.12c)$$

(3.12d)

Here $D_\mu = I\,\partial_\mu + ig_3 T^A G^A_\mu + ig_2 \frac{\tau^I}{2} W^I_\mu + ig_1 Y B_\mu$ is the gauge covariant derivative, T^A are the $SU(3)$ generators, $\tau^I/2$ are the $SU(2)$ generators, Y is the $U(1)$ hypercharge, while B_μ, G^A_μ, and W^I_μ are the gauge fields and g_1, g_2, g_3 the corresponding gauge couplings. The Higgs field in the unitary gauge is given by $H = \sqrt{1/2}(0,\, h + v)^T$, with $\widetilde{H} = i\tau_2 H^*$. Finally, the combinations of covariant derivatives are given by $\overleftrightarrow{D}_\mu = \overrightarrow{D}_\mu - \overleftarrow{D}_\mu$ and $\overleftrightarrow{D}^I_\mu = \tau^I \overrightarrow{D}_\mu - \overleftarrow{D}_\mu \tau^I$, while the subscripts $p,\ r,\ s,\ t$ represent flavor indices.

[1] We neglect the effects induced by neutrino masses. These are induced at dimension-5 in SMEFT [142], but are negligible for our purposes.

3.2.2 Low-scale Effective Lagrangian and tree level bounds

In order to describe the new physics contributions to semileptonic CC decays of mesons, neutron, and nuclei, we need to evolve the effective Lagrangian involving the operators in Eq. (3.12a) down to a scale of $O(\text{GeV})$. To do so, at the weak scale $\mu \sim m_W$, we match the SMEFT to the so-called low-energy Effective Field Theory (LEFT) [147], which is invariant under $SU(3)_c \times U(1)_{em}$ and contains the Standard Model fields except for the heavy W, Z, and h bosons as well as the top quark. The LEFT Lagrangian for the semileptonic $d_j \to u$ transitions, with $d_1 = d$ and $d_2 = s$, is given by [25, 98, 209, 210] [2]

$$\begin{aligned}
\mathcal{L}_{\text{LEFT}} = \; & - \frac{G_F V_{ud_j}}{\sqrt{2}} \Big[\left(1 + \epsilon_L^{\beta d_j} - \epsilon_L^{\mu}\right) \, \bar{e}\gamma_\mu(1-\gamma_5)\nu_e \cdot \bar{u}\gamma^\mu(1-\gamma_5)d_j \\
& + \epsilon_R^{d_j} \, \bar{e}\gamma_\mu(1-\gamma_5)\nu_e \cdot \bar{u}\gamma^\mu(1+\gamma_5)d_j \\
& + \epsilon_S^{d_j} \, \bar{e}(1-\gamma_5)\nu_e \cdot \bar{u}d_j - \epsilon_P^{d_j} \bar{e}(1-\gamma_5)\nu_e \cdot \bar{u}\gamma_5 d_j \\
& + \epsilon_T^{d_j} \, \bar{e}\sigma_{\mu\nu}(1-\gamma_5)\nu_e \cdot \bar{u}\sigma^{\mu\nu}(1-\gamma_5)d_j \Big] \; + \text{h.c.} \; ,
\end{aligned} \tag{3.13}$$

where G_F is the Fermi constant and the BSM contributions are encoded in the dimensionless couplings ϵ_i. ϵ_L^μ arises from the SMEFT correction to G_F as extracted from muon decay and is given by

$$\epsilon_L^\mu = -C_{\substack{ll \\ 1221}} + \left(C^{(3)}_{\substack{Hl \\ 11}} + C^{(3)}_{\substack{Hl \\ 22}} \right) \; , \tag{3.14}$$

in terms of leptonic vertex corrections introduced above and the coefficient associated with the purely leptonic operator (note that $C_{\substack{ll \\ prst}} = C_{\substack{ll \\ stpr}}$)

$$Q_{\substack{ll \\ prst}} = (\bar{l}_p \gamma_\mu l_r)(\bar{l}_s \gamma^\mu l_t) \; .$$

In order to connect the Wilson coefficients of SMEFT and LEFT, we require the equality of the $d_j \to u e^- \bar{\nu}_e$ amplitudes at the energy scale $\mu \sim m_W$. The resulting matching

[2] We write here only the operators involving electrons and their neutrinos. The inclusion of the second family of leptons is straightforward. Our analysis below assumes lepton family universality.

conditions are [25]

$$\epsilon_L^{\beta d_j} = C^{(3)}_{\substack{Hl\\11}} + \frac{[C^{(3)}_{Hq}V]_{1j}}{V_{ud_j}} - \frac{[C^{(3)}_{lq}V]_{1j}}{V_{ud_j}} \ , \tag{3.15a}$$

$$\epsilon_R^{d_j} = \frac{1}{2}\frac{[C_{Hud}]_{1j}}{V_{ud_j}}, \tag{3.15b}$$

$$\epsilon_S^{d_j} = -\frac{[C^{\dagger}_{ledq} + C^{(1)\dagger}_{lequ}V]_{1j}}{2\ V_{ud_j}} \ , \tag{3.15c}$$

$$\epsilon_P^{d_j} = \frac{[C^{\dagger}_{ledq} - C^{(1)\dagger}_{lequ}V]_{1j}}{2\ V_{ud_j}} \ , \tag{3.15d}$$

$$\epsilon_T^{d_j} = -\frac{[C^{(3)\dagger}_{lequ}V]_{1j}}{2\ V_{ud_j}} \ . \tag{3.15e}$$

Semileptonic decays depend on the individual effective couplings $\epsilon^{d_j}_{R,S,P,T}$ and on the linear combination $\epsilon_L^{(d_j)} \equiv \epsilon_L^{\beta d_j} - \epsilon_L^{\mu}$, which can be written as follows in terms of the SMEFT Wilson coefficients:

$$\epsilon_L^{(d_i)} = \frac{[C^{(3)}_{Hq}V]_{1j}}{V_{ud_j}} - \frac{[C^{(3)}_{lq}V]_{1j}}{V_{ud_j}} + C_{\substack{ll\\1221}} - C^{(3)}_{\substack{Hl\\22}} \ . \tag{3.16}$$

From the above equation, it follows that contributions of $C^{(3)}_{\substack{Hl\\11}}$ from muon and β decay cancel each other.

The rotation to the mass basis generates Wilson coefficients involving all family indices, e.g., $[C^{(3)}_{Hq} \cdot V]_{11} = C^{(3)}_{\substack{Hq\\11}}V_{11} + C^{(3)}_{\substack{Hq\\12}}V_{21} + C^{(3)}_{\substack{Hq\\13}}V_{31}$. In our analysis, we omit terms involving off-diagonal CKM matrix elements, as their contributions are suppressed by one or more powers of the Wolfenstein parameter $\lambda \equiv |V_{us}| \sim 0.22$. Hence, we identify the set of of Wilson coefficients associated with the operators that contribute to semileptonic decays of mesons, baryons, and nuclei at a tree-level ($j = 1, 2$):

$$C_\beta = \{C^{(3)}_{\substack{lq\\111j}}, C_{\substack{ledq\\11j1}}, C^{(1)}_{\substack{lequ\\11j1}}, C^{(3)}_{\substack{lequ\\11j1}}, C^{(3)}_{\substack{Hl\\11}}, C^{(3)}_{\substack{Hl\\22}}, C^{(3)}_{\substack{Hq\\1j}}, C_{\substack{Hud\\1j}}, C_{\substack{ll\\1221}}, C_{\substack{ll\\2112}}\}. \tag{3.17}$$

Finally, to assess their impact on low-energy CC processes, the ϵ_i couplings need to be evolved from the weak scale down to hadronic scales, $\mu_0 \simeq 2$ GeV. This leads to significant effects for the scalar and tensor operators, which have nonzero $\mathcal{O}(\alpha_s)$ anomalous dimensions. At one loop in QCD, we find $\epsilon_{S,P}(\mu_0) \simeq 1.64\,\epsilon_{S,P}(\mu_W)$ and $\epsilon_T(\mu_0) \simeq 0.85\,\epsilon_T(\mu_W)$, for $\mu_W = 246$ GeV. The remaining couplings are subject to smaller, %-level, effects due to QED loops, see Ref. [211] for more details.

3.2.3 Operator Mixing

In the previous section, we expressed the effective couplings ϵ_i in terms of the SMEFT Wilson coefficients at the matching scale $\mu_W \sim M_W$ between SMEFT and LEFT. The next step is to evolve the SMEFT coefficients from the high energy scale Λ to μ_W using the Renormalization Group Equations (RGEs).

This is motivated by: (i) The high precision reached by the experiment and SM theory predictions for β decays of mesons, hadrons, and nuclei. In a tree-level analysis, the current per-mille level precision corresponds to probing effective scales up to $\Lambda \sim 20$ TeV.

(ii) The emergence of tensions with the Cabibbo universality test, related to the unitarity of the Cabibbo-Kobayashi-Maskawa (CKM) matrix, which requires $\Delta_{\rm CKM} \equiv |V_{ud}|^2 + |V_{us}|^2 + |V_{ub}|^2 - 1 = 0$. The current hints of $\Delta_{\rm CKM} \neq 0$ at $\sim 3\sigma$ have generated scrutiny within the SM [75–87] as well as beyond the SM (BSM) studies [88–101], in the context of explicit models of new physics, in the EFT setting below the weak scale, and in the SMEFT at tree level.

As the renormalization scale μ changes, the effective interactions mix, leading to the emergence of new operators in the beta decay analysis at the loop level. The RGEs for the Wilson coefficients of the relevant operators take the following form

$$\begin{bmatrix} \dot{C}_\beta \\ \\ \dot{C}_x \end{bmatrix} = \begin{bmatrix} \gamma_{\beta\beta} & \gamma_{\beta x} \\ \\ \gamma_{x\beta} & \gamma_{xx} \end{bmatrix} \begin{bmatrix} C_\beta \\ \\ C_x \end{bmatrix} , \tag{3.18}$$

where $\dot{C}_i = 16\pi^2 \mu \frac{dC_i}{d\mu}$ and $\gamma_{\beta\beta}$, $\gamma_{\beta x}$, γ_{xx} are matrices of anomalous dimensions. C_β is the array of Wilson coefficients associated with operators that contribute to semileptonic processes at the tree level, defined explicitly in Eq. (3.17). C_x contains all the remaining Wilson coefficients that can mix onto the C_β's, i.e. for which $\gamma_{\beta x} \neq 0$. Inspection of the one-loop RGEs [146, 208, 212] shows that mixing occurs through the gauge and Yukawa interactions (we retain only the top- and bottom-quark Yukawa couplings). Numerically, the largest mixing occurs for coefficients C_x belonging to these classes:

$$C_x \in \{C_{lq}^{(3)}, C_{ll}, C_{Hl}^{(3)}, C_{Hq}^{(3)}, C_{qq}^{(1)}, C_{qq}^{(3)}, C_{H\Box}\} , \tag{3.19}$$

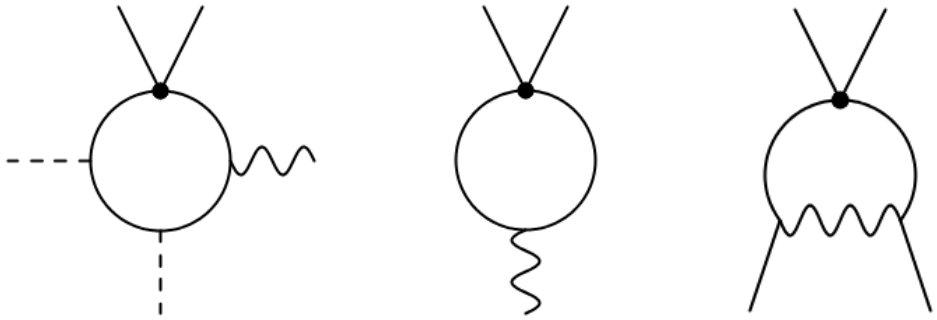

Figure 3.3: Diagrams illustrating the loop contributions of Q_x operators to Q_β. Black circles represent the insertion of Q_x operators. Solid lines denote fermions, dashed lines represent Higgs bosons, and wavy lines stand for gauge bosons.

with various combinations of family indices, as discussed below. The most relevant one-loop diagram topologies are given in Fig. 3.3.

The coefficients $C_\beta(\mu_W)$ at a low scale close to the weak scale, expressed in terms of $C_x(\Lambda)$, take the form

$$C_{\beta i}(\mu_W) = \sum_k U_{ik}(\mu_W, \Lambda) C_{xk}(\Lambda) \ , \tag{3.20}$$

where the matrix $U(\mu_W, \Lambda)$ is obtained by solving the RGEs. Consequently, by combining the mixing induced by RGE running with the matching in Eq. (3.15), we can represent the effective couplings ϵ_i in terms of the C_x coefficients as

$$\epsilon_i(\mu_W) = \sum_j \kappa_{ij}(\mu_W, \Lambda) C_{xj}(\Lambda) \ . \tag{3.21}$$

This formula, together with the experimental determination of the ϵ_i, allows us to obtain constraints on $C_x(\Lambda)$. In this work, we take $\Lambda = 5$ TeV for the initial scale of the RG evolution [3]. The results are presented and discussed in the following section.

[3]Larger (smaller) values of Λ will make the bounds we discuss below stronger (weaker). The dependence on Λ is logarithmic, hence relatively weak.

3.2.4 Results

We find that the largest impact of operator running and mixing manifests in the low-energy coupling $\epsilon_L(\mu_W)$. The mixing contributions to $\epsilon_{R,S,P,T}$ are less prominent and lead to weaker constraints on the C_x.

Right-handed current, scalar, pseudoscalar, and tensor terms

For this class of couplings, most of the non-zero mixings are small because of the appearance of the numerically suppressed y_b Yukawa coupling. As an example, consider the evolution of the Wilson coefficient C_{Hud} associated with the right-handed quark current operator defined in Eq. (3.12c). The corresponding RGE term describing this evolution is

$$\dot{C}_{\substack{Hud \\ 11}} \supset 4(C^{(1)}_{\substack{ud \\ 1331}} + \frac{4}{3} C^{(8)}_{\substack{ud \\ 1331}})[Y_u Y_d^\dagger]_{33} \tag{3.22}$$

By solving the RGEs, we obtain a bound of $O(1)$ for the coefficients $C^{(1),(8)}_{\substack{ud \\ 1331}}$, implying a rather weak limit on the BSM scale, $\Lambda \gtrsim v$. Analogous or even weaker bounds occur for the other C_x coefficients that do not generate the left-handed currents.

The numerical results for $\epsilon_i^{(d)}$ at the scale $\mu_W = 246$ GeV in terms of C_β and C_x SMEFT coefficients at $\Lambda = 5$ TeV are given by

$$\epsilon_R^{(d)} = 0.950\ C_{\substack{Hud \\ 11}} - 0.001\ C^{(1)}_{\substack{ud \\ 1331}} - 0.0011\ C^{(8)}_{\substack{ud \\ 1331}} \ . \tag{3.23}$$

$$\epsilon_P^{(d)} = 0.603\ C^{(1)}_{\substack{lequ \\ 1111}} - 0.600\ C_{\substack{ledq \\ 1111}} + 0.143\ C^{(3)}_{\substack{lequ \\ 1111}} \ . \tag{3.24}$$

$$\epsilon_S^{(d)} = -0.603\ C^{(1)}_{\substack{lequ \\ 1111}} - 0.600\ C_{\substack{ledq \\ 1111}} + 0.143\ C^{(3)}_{\substack{lequ \\ 1111}} \ . \tag{3.25}$$

$$\epsilon_T^{(d)} = 0.003\ C^{(1)}_{\substack{lequ \\ 1111}} - 0.465\ C^{(3)}_{\substack{lequ \\ 1111}} \ . \tag{3.26}$$

Operators involving left-handed currents

The RGEs induce contributions from several Wilson coefficients to ϵ_L. The coefficients of these operators are collected in C_x in Eq. (3.19). Of the appearing operators, Q_{ll}, $Q^{(3)}_{lq}$, $Q^{(3)}_{Hl}$,

$Q^{(3)}_{Hq}$ are found within the set of Q_β operators in Eqs. (3.12a)-(3.12d), but with a distinct flavor content from the operators that contribute at the tree level. The other three operators are

$$Q^{(1)}_{\substack{qq\\prst}} = (\bar{q}_p\gamma_\mu\tau q_r)(\bar{q}_s\gamma^\mu q_t), \tag{3.27a}$$

$$Q^{(3)}_{\substack{qq\\prst}} = (\bar{q}_p\gamma_\mu\tau^I q_r)(\bar{q}_s\gamma^\mu\tau^I q_t), \tag{3.27b}$$

$$Q_{H\Box} = (H^\dagger H)\Box(H^\dagger H)\ . \tag{3.27c}$$

In particular, the largest contributions to ϵ_i, namely with $\kappa_{ij} \geq 10^{-2}$, see (3.21) arise from $C^{(3)}_{\substack{qq\\1133}}$, $C^{(3)}_{\substack{qq\\1331}}$,$C^{(1)}_{\substack{qq\\1331}}$, $C_{\substack{ll\\1122}}$, $C^{(3)}_{\substack{lq\\2233}}$, $C^{(3)}_{\substack{lq\\1111}}$, $C^{(3)}_{\substack{lq\\1122}}$,$C^{(3)}_{\substack{lq\\1133}}$, $C^{(3)}_{\substack{lq\\2211}}$, and $C^{(3)}_{\substack{Hq\\11}}$, $C^{(3)}_{\substack{Hq\\22}}$, $C^{(3)}_{\substack{Hq\\33}}$.

The numerical results for the RG evolution matrix $U_{ik}(\mu_W, \Lambda)$ connecting $C_{xk}(\Lambda)$ to $C_{\beta i}(\mu_W)$ (see Eq. (3.20)) can be found in Table A.1 in Appendix A. Upon matching on the LEFT coefficients (see Eqs.((3.15)) we find that the $\epsilon^{(d,s)}_L$ at the scale $\mu_W = 246$ GeV in terms of SMEFT coefficients at $\Lambda = 5$ TeV are given by

$$\begin{aligned}\epsilon^{(d)}_L &= 0.946\ C^{(3)}_{\substack{Hq\\11}} - 1.052\ C^{(3)}_{\substack{lq\\1111}} + 1.012\ C_{\substack{ll\\1221}} - 0.965\ C^{(3)}_{\substack{Hl\\22}} \\ &+ 0.198\ C^{(3)}_{\substack{qq\\1133}} - 0.026\ C^{(3)}_{\substack{qq\\1331}} + 0.026\ C^{(1)}_{\substack{qq\\1331}} - 0.0471\ C_{\substack{ll\\1122}} - 0.100\ C^{(3)}_{\substack{lq\\2233}}\ ,\end{aligned} \tag{3.28}$$

$$\begin{aligned}\epsilon^{(s)}_L &= \frac{0.942}{\lambda}\ C^{(3)}_{\substack{Hq\\12}} - \frac{1.052}{\lambda}\ C^{(3)}_{\substack{lq\\1112}} + 1.010\ C_{\substack{ll\\1221}} - 0.960\ C^{(3)}_{\substack{Hl\\22}} \\ &+ \frac{0.198}{\lambda}\ C^{(3)}_{\substack{qq\\1233}} - \frac{0.028}{\lambda}\ C^{(3)}_{\substack{qq\\1332}} + \frac{0.026}{\lambda}\ C^{(1)}_{\substack{qq\\1332}} - 0.099\ C^{(3)}_{\substack{lq\\2233}} - 0.047\ C_{\substack{ll\\1122}} \\ &+ 0.0144\ (C^{(3)}_{\substack{Hq\\11}} + C^{(3)}_{\substack{Hq\\22}} + C^{(3)}_{\substack{Hq\\33}}) - 0.016\ (C^{(3)}_{\substack{lq\\1111}} + C^{(3)}_{\substack{lq\\1122}} + C^{(3)}_{\substack{lq\\1133}})\ .\end{aligned} \tag{3.29}$$

Here $\lambda \equiv |V_{us}| \sim 0.22$. To arrive at the expressions above, we used the symmetry under the exchange of the fermion bilinears, $C^{(1),(3)}_{\substack{qq\\prst}} = C^{(1),(3)}_{\substack{qq\\stpr}}$, $C_{\substack{ll\\prst}} = C_{\substack{ll\\stpr}}$. Note that $\epsilon^{(d)}_L$ and $\epsilon^{(s)}_L$ have similar dependencies on the C_x Wilson coefficients in the first two lines of Eqs. (3.28) and (3.29), with appropriate replacements of the first and second family indices. The small %-level differences arise from two-loop level effects captured by the RGEs in the leading-log approximation.

The expressions in Eqs. (3.23)-(3.26) as well as (3.28) and (3.29) are in principle modified by one-loop corrections to the tree-level matching in Eq. (3.15). As we do not control all

contributions at this order, i.e. one-loop terms without large logarithms $\sim \ln(\Lambda/m_W)$, they are beyond the precision of our leading-log analysis. Nevertheless, using the results of Ref. [213], we estimated the order of magnitude of these terms, finding that they do not lead to large contributions of new Wilson coefficients in the above equations. In addition, the corrections to the C_x contributions found above tend to be small compared to our leading-log results. For example, the loop-level matching affects the contributions of $[C_{qq}^{(3)}]_{1j33}$ in Eqs. (3.28) and (3.29) by $\mathcal{O}(10\%)$.

To impose constraints on the difference $\epsilon_L^{(d_j)} = \epsilon_L^{\beta d_j} - \epsilon_L^{\mu}$, we employ the analysis of [101]. That reference utilized the first-row unitarity relation for the Cabibbo-Kobayashi-Maskawa (CKM) matrix by incorporating data from kaon, pion, and β decay, following Refs. [98, 210]. Apart from these low-energy CC processes, this analysis included electroweak precision measurements and collider observables, thereby allowing for a nearly model-independent analysis of SMEFT operators. However, as argued above, the effects of the C_x coefficients mostly induce the left-handed interactions governed by $\epsilon_L^{(d_j)}$. Therefore, we perform a simpler analysis in which only these couplings are turned on. The constraints on $\epsilon_L^{(s,d)}$ are dominated by the CKM unitarity test, which implies

$$\Delta_{\rm CKM} = 2|V_{ud}|^2\epsilon_L^{(d)} + 2|V_{us}|^2\epsilon_L^{(s)}\,. \tag{3.30}$$

From Eqs. (3.29) and (3.30) one sees that C_x's that contribute to $\epsilon_L^{(s)}$ appear in $\Delta_{\rm CKM}$ with at least one extra power of λ compared to the C_{xk} that contribute to $\epsilon_L^{(d)}$. So in what follows, we focus on the strongest constraints on the C_{xk}'s appearing in Eq. (3.28) provided by

$$\epsilon_L^{(d)} = (-8.3 \pm 2.5) \times 10^{-4}\,. \tag{3.31}$$

The constraints on the coefficients appearing in (3.29) can be obtained via rescaling by λ.

While Eq. (3.28) provides the general contributions, we explore below the simplified scenario in which only one coefficient is nonzero at the high energy scale Λ. This leads to conservative constraints on the C_x operators, as long as there are no significant cancellations between different SMEFT operators. The most stringent constraints (corresponding $\delta C_x \leq 5 \times 10^{-2}$) are graphically illustrated in Fig. 3.4 and reported in Table 3.5, along with a comparison to the limits obtained from other observables.

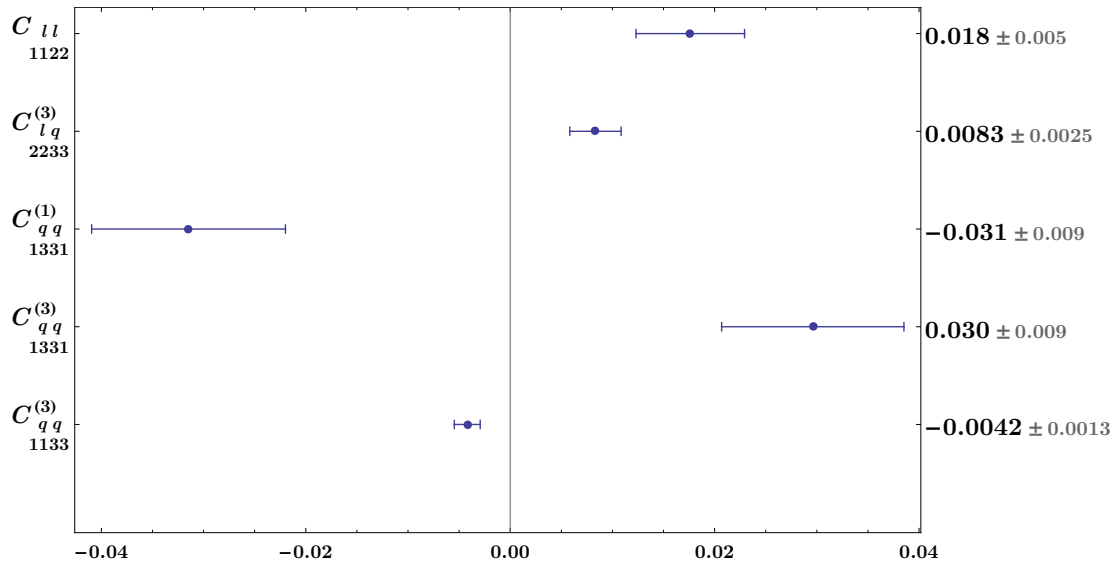

Figure 3.4: Summary of the strongest low-energy CC constraints on the coefficients $C_{xk}(\Lambda)$ (68% C.L.). We only show results for the most strongly constrained coefficients, with a threshold of $\delta C_{xk} < 5 \times 10^{-2}$.

As can be seen from the Table, low-energy CC processes probe some of the Wilson coefficients at the permille level. For the purely leptonic operator, this leads to a sensitivity comparable to that of muon pair production. For semileptonic operators involving the top quark, the constraints of low-energy CC processes are stronger than the ones from top production, but weaker than the ones from rare $\Delta F = 1$ meson decays and the $K_L - K_S$ mass difference. It should be noted, however, that the constraints from the $\Delta F = 1$ and $\Delta F = 2$ processes depend on the flavor structure of the Wilson coefficients. In particular, defining the Wilson coefficients in a basis where M_d, instead of M_u, is diagonal would lead to far less stringent constraints from these probes, while those from low-energy CC measurements would be mostly unchanged. We provide details on our analysis of $\Delta F = 1$ and $\Delta F = 2$ processes in Section 3.2.4.

$C_x(\Lambda = 5\,\text{TeV})$	Constraint from β decays	Strongest constraints from other processes	Process
$C^{(3)}_{qq\ 1133}$	-0.004 ± 0.0013	$-0.0073 \pm 0.006^{(1)}$ $\pm 0.00002^{(2)}$	Top production [214] $K \to \pi\nu\bar{\nu}$
$C^{(3)}_{lq\ 2233}$	0.008 ± 0.0025	$-0.00024 \pm 0.00021^{(2)}$	B decays (R_K) [215]
$C_{ll\ 1122}$	0.018 ± 0.005	-0.0018 ± 0.0029	Muon pair production [216]
$C^{(1)}_{qq\ 1331}$	-0.031 ± 0.009	$-0.035 \pm 0.027^{(1)}$ $\pm 0.0009^{(2)}$	Top production [214] Δm_K [217]
$C^{(3)}_{qq\ 1331}$	0.03 ± 0.009	$-0.042 \pm 0.024^{(1)}$ $\pm 0.00004^{(2)}$	Top production [214] $K \to \pi\nu\bar{\nu}$

Table 3.5: Summary of the strongest loop-level constraints from β decays, defined by the threshold $\delta C_{xi}(\Lambda = 5\ \text{TeV}) \leq 0.05$. We display the relevant SMEFT Wilson coefficients (first column), the 68% C.L. constraint from β decays (second column), and the strongest 68% C.L. constraints from other processes (third and fourth columns). The superscript $^{(1)}$ indicates that the fit was performed assuming $U(3)_l \times U(3)_e \times U(3)_d \times U(2)_u \times U(2)_q$ symmetry. The superscript $^{(2)}$ indicates that the constraint would disappear if one used the weak basis in which the down-type quark mass matrix M_d is diagonal. See the text for details on how the bounds from "other processes" have been obtained.

Table 3.5 also shows that, due to the current deviation from the CKM unitarity, β and meson decays prefer nonzero values for the dimension-six interactions at the $\sim 3\sigma$ level. For some of the Wilson coefficients, the size needed to address CKM unitarity is in conflict with other measurements. For example, the current value of $\Delta_{\rm CKM} \neq 0$ could be explained with nonzero values of the four-quark Wilson coefficients, $[C_{qq}^{(1,3)}]_{1331} \simeq 0.03$. However, these relatively large coefficients are in tension with the kaon mass difference, Δm_K. Therefore, should the current anomaly in CKM unitarity be confirmed, an explanation in terms of the Wilson coefficients in Table 3.5 would require a scenario involving multiple operators at a time.

In the following subsections, we provide details about the operator mixing, as well as the constraints on the C_x from other observables.

$C_{qq,\ 3311}^{(3)}$

The most precise constraints obtained from the above analysis are for the coefficients of four-quark operators, $C_{qq}^{(3)}$. The flavor structures that contribute to β decays contain two first-family quarks and two third-family quarks. In the context of beta decay, these quarks are up, down, top, and bottom. These operators primarily contribute to $C_{\substack{Hq\\11}}^{(3)}$ via the SM Yukawa or gauge couplings. The corresponding one-loop contributions are illustrated in Fig. 3.3 (left and middle diagrams) and lead to the following RGE

$$\dot{C}_{\substack{Hq\\11}}^{(3)} \supset 2N_c\big(C_{\substack{qq\\1133}}^{(3)} + C_{\substack{qq\\3311}}^{(3)}\big)\left(\frac{1}{3}g_2^2 - [Y_u{}^\dagger Y_u]_{33}\right) \ . \tag{3.32}$$

Furthermore, these operators also generate $Q_{\substack{lq\\1111}}^{(3)}$ as shown in the middle diagram in Fig. 3.3 after attaching a lepton line (not shown) to the gauge boson. The RGE terms describing this contribution are

$$\dot{C}_{\substack{lq\\1111}}^{(3)} \supset \frac{2}{3}g_2^2 N_C C_{\substack{qq\\1133}}^{(3)} + \frac{2}{3}g_2^2 N_C C_{\substack{qq\\3311}}^{(3)} \ . \tag{3.33}$$

This, together with the bound on ϵ_L, leads to

$$C_{\substack{qq\\3311}}^{(3)} \ , \ C_{\substack{qq\\1133}}^{(3)} = (-4 \pm 1.3) \times 10^{-3} \, . \tag{3.34}$$

In addition, the $Q^{(3)}_{\substack{qq\\1133}}$ and $Q^{(3)}_{\substack{qq\\3311}}$ operators play a significant role in various other processes at tree-level, particularly in top quark production. Multiple global fits have been performed in order to constrain the operators' coefficients; see, e.g., Refs. [214, 218, 219]. The most stringent constraint was obtained in Ref. [214], which performed a fit assuming $U(2)_q \times U(2)_u \times U(2)_d$ symmetry. This resulted in a constraint on the following linear combination of SMEFT coefficients, $c^{3,1}_{Qq} = C^{(3)}_{\substack{qq\\ii33}} + \frac{1}{6}(C^{(1)}_{\substack{qq\\i33i}} - C^{(3)}_{\substack{qq\\i33i}})$, where the index i is summed over the first and the second families. In a global analysis, the constraint on this linear combination is (-0.0048 ± 0.0122) with 95% confidence level (CL) intervals. Assuming only a single Wilson coefficient from the Warsaw basis to be present at a time, one obtains

$$C^{(3)}_{\substack{qq\\3311}}\ ,\ C^{(3)}_{\substack{qq\\1133}} = (-0.0073 \pm 0.0053)\,, \tag{3.35}$$

at 68% CL, implying the loop level constraint from β decays are approximately five times more sensitive.

Finally, the strong but basis-dependent constraints from $\Delta S = 1$ and $\Delta S = 2$ FCNC processes are discussed in Section 3.2.4.

$C^{(3)}_{lq,2233}$

The next-best constraint arising from our analysis relates to the operator $Q^{(3)}_{lq}$, with two second-family leptons and two third-family quarks, as shown in Eq. (3.12a). This operator generates $Q^{(3)}_{\substack{Hl\\22}}$ that characterizes the vertex for muon decay. The analogous operator involving the first generation, $Q^{(3)}_{\substack{Hl\\11}}$, is also generated by $C^{(3)}_{lq,1133}$ (however, as shown in Eq. (3.16) such effects cancel in $\epsilon^{(d,s)}_L$). The $Q^{(3)}_{\substack{lq\\2233}}$ contribution to $Q^{(3)}_{\substack{Hl\\22}}$ is shown in the left diagram in Fig. 3.3. The RGE term that generates the dominant contribution reads:

$$\dot{C}^{(3)}_{\substack{Hl\\22}} \supset 2N_c C^{(3)}_{\substack{lq\\2233}} \left(\frac{1}{3}g_2^2 - [Y_u^\dagger Y_u]_{33}\right)\,. \tag{3.36}$$

After solving the above RGE and imposing the CC constraints, we obtain

$$C^{(3)}_{\substack{lq\\2233}} = (8 \pm 2.5) \times 10^{-3}\,. \tag{3.37}$$

The same operator also plays a role in B decays at a tree level. In a single-coupling analysis, the comparison of $b \to c\mu\nu$ and $b \to ce\nu$ transitions can constrain the relevant coefficient,

leading to an allowed range of $[-0.0005, 0.022]$ at $\mu = 1$ TeV [220]. This bound is approximately one order of magnitude weaker compared to what was obtained from β decay.

A stronger constraint can be obtained from $B \to K\ell\ell$ decays, to which $C^{(3)}_{\substack{lq \\ 2233}}$ contributes at tree level after performing the CKM rotation to the mass basis in $Q^{(3)}_{\substack{lq \\ 2233}}$. Ref. [215] performed a fit at $\mu = 1$ TeV, assuming that only operators involving top quarks are present at $\mu = 1$ TeV, while the lepton flavor structure was left arbitrary. The dominant constraint comes from the Lepton Flavor Universality ratio

$$R_K = \frac{\mathrm{Br}(B^+ \to K^+\mu^+\mu^-)}{\mathrm{Br}(B^+ \to K^+e^+e^-)} \ . \tag{3.38}$$

and implies $C^{(3)}_{\substack{lq \\ 2233}} = (-2.4 \pm 2.1) \times 10^{-4}$ for the scenario when only one operator is present at a time. This bound has a smaller error and mean value compared to the constraint from low-energy CC observables.

$C_{ll,1122}$

These Wilson coefficients generate $C_{\substack{ll \\ 1221}}$ through loop diagrams that involve the gauge coupling, as shown in the right panel of Fig. 3.3. This is characterized by the RGEs

$$\dot{C}_{\substack{ll \\ 1221}} \supset 6\, C_{\substack{ll \\ 1122}} g_2^2 \ , \qquad \dot{C}_{\substack{ll \\ 2112}} \supset 6\, C_{\substack{ll \\ 2211}} g_2^2 \ , \tag{3.39}$$

leading to the constraint

$$C_{\substack{ll \\ 1122}} = C_{\substack{ll \\ 2211}} = (1.8 \pm 0.5) \times 10^{-2} \ . \tag{3.40}$$

The above-mentioned operators also induce muon pair production at tree level. Ref. [216] performed a global fit that incorporated experimental data from various sources, including Z boson measurements at LEP-1, W boson mass and decay measurements, muon and tau decays, and lepton pair production at LEP-2. Under the assumption that only one operator is present at a time, this led to an allowed range of $(-1.8 \pm 2.9) \times 10^{-3}$ at 1 TeV with 68% CL, comparable to the bound from low-energy CC processes.

$C^{(3)}_{qq,1331}$

The operator $Q^{(3)}_{qq}$, discussed in Section 3.2.4, reappears in the analysis, albeit with different particle content. In particular, $C^{(3)}_{qq,1331}$ contributes to both $C^{(3)}_{\substack{Hq\\11}}$ and $C^{(3)}_{\substack{lq\\1111}}$ via the left and middle diagrams of Fig. 3.3,

$$\dot{C}^{(3)}_{\substack{Hq\\11}} \supset \left(C^{(3)}_{\substack{qq\\1331}} + C^{(3)}_{\substack{qq\\3113}}\right)\left([Y_u{}^\dagger Y_u]_{33} - \frac{1}{3}g_2^2\right) , \tag{3.41}$$

$$\dot{C}^{(3)}_{\substack{lq\\1111}} \supset -\frac{1}{3}g_2^2 C^{(3)}_{\substack{qq\\1331}} - \frac{1}{3}g_2^2 C^{(3)}_{\substack{qq\\3113}} . \tag{3.42}$$

These RGEs lead to the following limits from β decays,

$$C^{(3)}_{\substack{qq\\1331}} \ , \ C^{(3)}_{\substack{qq\\3113}} = (3.0 \pm 0.9) \times 10^{-2} . \tag{3.43}$$

The above effective couplings modify top quark production processes. Ref. [214] obtained the following constraints on several linear combinations of Wilson coefficients,

Linear combination	Constraint
$c^{1,8}_{Qq} = C^{(1)}_{\substack{qq\\i33i}} + 3C^{(3)}_{\substack{qq\\i33i}}$,	0.121 ± 0.30 ,
$c^{1,1}_{Qq} = C^{(1)}_{\substack{qq\\ii33}} + \frac{1}{6}C^{(1)}_{\substack{qq\\i33i}} + \frac{1}{2}C^{(3)}_{\substack{qq\\i33i}}$,	0.30 ± 0.61 ,
$c^{3,8}_{Qq} = C^{(1)}_{\substack{qq\\i33i}} - C^{(3)}_{\substack{qq\\i33i}}$,	-0.12 ± 0.30 ,

as well as the previously mentioned constraint on $c^{3,1}_{Qq}$, see Section 3.2.4. Evaluating these resultso, assuming that only one Wilson coefficient from the Warsaw basis is present at a time, we extract $C^{(3)}_{\substack{qq\\1331}} \approx (-0.042 \pm 0.024)$ at 68% CL, which is a factor of a few weaker than the result from β decays. Finally, our analysis of the constraints from $\Delta S = 1$ and $\Delta S = 2$ FCNC processes is discussed in Section 3.2.4.

$C^{(1)}_{qq,1331}$

The final operator coefficient from Table 3.5 we discuss here is similar to that of the previous section, but with a different weak isospin dependence. It contributes primarily to the operators $Q^{(3)}_{\substack{Hq\\11}}$ through the loop diagrams involving a Yukawa interaction in Fig. 3.3. The RG equation

$$\dot{C}^{(3)}_{\substack{Hq\\11}} \supset \left(C^{(1)}_{\substack{qq\\1331}} + C^{(1)}_{\substack{qq\\3113}}\right)\left(\frac{1}{3}g_2^2 - [Y_u{}^\dagger Y_u]_{33}\right) \tag{3.45}$$

leads to the following limit from low-energy CC processes:

$$C^{(1)}_{\substack{qq\\1331}} \ , \ C^{(1)}_{\substack{qq\\3113}} = (-3.1 \pm 0.9) \times 10^{-2} \ . \tag{3.46}$$

Direct constraints on this coefficient have been obtained in Ref. [214] through top quark production. Evaluating the fit while only one Wilson coefficient of the Warsaw basis was present at a time, at 68% CL, we extract $C^{(1)}_{\substack{qq\\1331}} \approx -0.035 \pm 0.027$. This result is a factor of a few weaker than the limit obtained from β decay, albeit with a similar central value. We discuss the constraints from $\Delta S = 1$ and $\Delta S = 2$ FCNC processes in Section 3.2.4.

FCNC processes

As mentioned above, the limits on the Wilson coefficient that arise from beta decay at the loop level are competitive with those obtained from other processes that are induced at the tree level. Here, we discuss several other probes of the Wilson coefficients in more detail, with particular emphasis on Flavor-Changing Neutral Current (FCNC) processes. FCNCs are suppressed in the Standard Model due to the GIM mechanism [221], which is generally violated in New Physics models and within SMEFT. These observables are therefore highly sensitive to contributions from physics beyond the Standard Model, given the low SM background and high experimental precision.

As discussed in section 3.2.4, probes of $\Delta F = 1$ transitions are able to constrain a number of SMEFT operators at the tree level. In this section, we instead focus on the constraints from $\Delta F = 1$ FCNC processes that are induced at the loop level and from $\Delta F = 2$ observables. To investigate the former, we look for the FCNC dimension-six coefficients (C_{FCNC}) that could be generated by the same C_x coefficients that generate C_β, allowing us to compare the resulting limits. The relevant RGEs can be written schematically as

$$\dot{C}_\beta = \gamma_{\beta x} \, C_x \ , \tag{3.47a}$$

$$\dot{C}_{FCNC} = \gamma_{FCNCx} \, C_x \ . \tag{3.47b}$$

We focus on processes that can be calculated with negligible theoretical uncertainty, specifically, the rare decays of kaons and B mesons, taking into account the effects of the rotation to the mass basis. The strongest constraints arise from the rare $\Delta S = 1$ FCNC process

$K \to \pi\nu\bar{\nu}$, which is controlled by the LEFT coefficient $[L^{\nu d}_{VLL}]_{\ell\ell 12}$, currently bound to be smaller than $0.97 \times 10^{-4}\,\text{TeV}^{-2}$ [222, 223]. In terms of the SMEFT Wilson coefficients in our basis, we have

$$\begin{aligned} v^2[L^{\nu d}_{VLL}]_{\ell\ell 12} &= \tilde{C}_{\ell\ell 12} + \lambda\left(\tilde{C}_{\ell\ell 11} - \tilde{C}_{\ell\ell 22}\right) + O(\lambda^2) \\ \tilde{C}_{\ell\ell ij} &= C^{(1)}_{\substack{lq \\ \ell\ell ij}} - C^{(3)}_{\substack{lq \\ \ell\ell ij}} + \delta_{\ell\ell} C^{(1)}_{\substack{Hq \\ ij}} + \delta_{\ell\ell} C^{(3)}_{\substack{Hq \\ ij}} \,. \end{aligned} \tag{3.48}$$

For the running of $C^{(1),(3)}_{qq}$ into these couplings we find

$$\tilde{C}_{\ell\ell 11} \simeq \left(-0.099\, C^{(1)}_{\substack{qq \\ 1133}} - 0.0034\, C^{(1)}_{\substack{qq \\ 1331}} + 0.098\, C^{(3)}_{\substack{qq \\ 1133}} - 0.054\, C^{(3)}_{\substack{qq \\ 1331}}\right)\delta_{\ell\ell}\,, \tag{3.49}$$

while $\tilde{C}_{12,22}$ are much smaller than $\tilde{C}_{11}$. The limit on $[L^{\nu d}_{VLL}]_{\nu_\ell\nu_\ell 12}$ implies

$$C^{(1)}_{\substack{qq \\ 1133}} < 2.0 \cdot 10^{-5}\,, \qquad C^{(1)}_{\substack{qq \\ 1331}} < 0.57 \cdot 10^{-3}\,, \tag{3.50}$$

$$C^{(3)}_{\substack{qq \\ 1133}} < 2.0 \cdot 10^{-5}\,, \qquad C^{(3)}_{\substack{qq \\ 1331}} < 0.37 \cdot 10^{-4}\,. \tag{3.51}$$

Apart from measurements of rare $\Delta F = 1$ processes that violate flavor by one unit, stringent constraints arise from $\Delta F = 2$ observables, such as the $B_{d,s} - \bar{B}_{d,s}$ and $K_L - K_S$ mass differences. These mass differences are suppressed due to the GIM mechanism in the SM, which implies that the contributions from the four-quark operators $Q^{(1),(3)}_{qq}$ can be significant as they arise at the tree level, after rotating to the mass basis. To evaluate the constraints from $\Delta m_{B_{d,s}}$, we compare the sum of the SM [224] and BSM contributions [217] with the experimental determinations [225]. The SM prediction of Δm_K is subject to larger theoretical uncertainties. Although the short-distance contributions are known to about 30%, the long-distance effects are poorly known [226, 227]. In fact, preliminary lattice-QCD results are currently subject to significant systematic uncertainties [228]. Therefore, to set conservative constraints, we demand that the BSM contributions cannot be larger than the experimental determination, $\Delta m_K^{\text{BSM}} \leq \Delta m_K^{\text{exp}}$. Although it comes with significant uncertainties, the kaon mass difference is still the most sensitive probe of the $C^{(1),(3)}_{qq}$ coefficients, while the limits from Δm_{B_d} are a factor of a few weaker. Quantitatively, the $\Delta S = 2$ limits imply $|C^{(3)}_{\substack{qq \\ 1133}}|, |C^{(1)}_{\substack{qq \\ 1331}}|, |C^{(3)}_{\substack{qq \\ 1331}}| < 0.0009$. These constraints are weaker than the ones from $K \to \pi\nu\bar{\nu}$, except for $C^{(1)}_{\substack{qq \\ 1331}}$.

At face value, the $\Delta S = 1$ and $\Delta S = 2$ observables then lead to some of the strongest constraints on the $C_{qq}^{(1,3)}$ coefficients in Table 3.5. It should be noted, however, that these flavor-violating probes strongly depend on the assumed flavor structure of the Wilson coefficients. For example, defining the operators in the basis where M_d is diagonal, instead of using Eq. (3.11), would lead to severely weakened $\Delta F = 1$ and $\Delta F = 2$ constraints [217], while those from low-energy CC processes and $pp \to t\bar{t}$ would be mostly unaffected.

3.2.5 Simplified models above the Λ scale

Here, we briefly discuss the kind of BSM scenarios that could give rise to the operators discussed in the previous section. Above the Λ scale, such simplified scenarios can be constructed by introducing new heavy fields with all possible spin- and gauge representations. The complete list of new particles and their tree-level contributions to the SMEFT operators up to dimension-six are provided in Ref. [229]. This matching procedure allows us to express the SMEFT Wilson coefficients as functions of the couplings and masses in the appropriate simplified model. With the aid of the provided dictionary, we can readily identify all heavy fields that can generate the Wilson coefficients for which we established constraints. The results are summarized in Table 3.6.

There are two heavy fields, marked with an asterisk in Table 3.6, which exclusively contribute to the $Q_{qq}^{(3)}$ and $Q_{qq}^{(1)}$ operators that were constrained from β decay at the loop level. These heavy fields are a scalar boson Υ, which is a color sextet and a weak isotriplet, along with a vector boson $\mathcal{H}$, which is a color octet and a weak isotriplet. The scalar field can play a role in explanations of baryogenesis [230] and contributes to processes at the LHC [231]. The vector field $\mathcal{H}$ can appear as the gauge boson of an enlarged gauge group, $SU(6)$, which is broken down to the SM [232], or as a resonance arising from strongly coupled BSM physics [233]. Their contributions to the C_x operator coefficients, assuming only one multiplet at a time, read

$$C_{\substack{qq\\ijkl}}^{(1)} = \frac{3(y_\Upsilon)_{lj}(y_\Upsilon)_{ki}^*}{4M_\Upsilon^2} \,, \qquad C_{\substack{qq\\ijkl}}^{(3)} = \frac{3(y_\Upsilon)_{ki}^*(y_\Upsilon)_{jl}}{M_\Upsilon^2} \,, \tag{3.52a}$$

$$C_{\substack{qq\\ijkl}}^{(1)} = -\frac{3(g_\mathcal{H})_{kj}(g_\mathcal{H})_{il}}{32M_\mathcal{H}^2} \,, \qquad C_{\substack{qq\\ijkl}}^{(3)} = \frac{(g_\mathcal{H})_{kl}(g_\mathcal{H})_{ij}}{48M_\mathcal{H}^2} + \frac{(g_\mathcal{H})_{kj}(g_\mathcal{H})_{il}}{32M_\mathcal{H}^2} \,. \tag{3.52b}$$

where M_Υ and $M_\mathcal{H}$ are the masses of the heavy fields and y_Υ and $y_\mathcal{H}$ are their couplings to left-handed quarks. With respect to the flavor structure of these coefficients, it becomes apparent that we require significant couplings of $(y_\Upsilon)_{13}$, $(y_\Upsilon)_{31}$, $(y_\mathcal{H})_{11}$, $(y_\mathcal{H})_{33}$, $(y_\mathcal{H})_{13}$, $(y_\mathcal{H})_{31}$ to address the Cabibbo angle anomaly. For sufficiently small masses of heavy fields, these couplings can be examined in various processes at a tree level, particularly in top quark production. In addition, the needed Υ couplings involve different quark generations, implying significant contributions to FCNC processes in case the diagonal couplings are nonzero as well, $(y_\Upsilon)_{ii} \neq 0$.

Q_x operator	Heavy field						
$Q_{qq}^{(3)}$	ω_1	ζ	Ω_1	Υ^*	$\mathcal{W}$	$\mathcal{G}$,	$\mathcal{H}^*$
Irrep	$(3,1)_{-\frac{1}{3}}$	$(3,3)_{-\frac{1}{3}}$	$(6,1)_{\frac{1}{3}}$	$(6,3)_{\frac{1}{3}}$	$(1,1)_0$	$(8,1)_0$	$(8,3)_0$
$Q_{qq}^{(1)}$	ω_1	ζ	Ω_1	Υ^*	$\mathcal{B}$	$\mathcal{G}$,	$\mathcal{H}^*$
Irrep	$(3,1)_{-\frac{1}{3}}$	$(3,3)_{-\frac{1}{3}}$	$(6,1)_{\frac{1}{3}}$	$(6,3)_{\frac{1}{3}}$	$(1,3)_0$	$(8,1)_0$	$(8,3)_0$
$Q_{lq}^{(3)}$	ω_1	ζ	$\mathcal{W}$	$\mathcal{U}_2$	$\mathcal{X}$		
Irrep	$(3,1)_{-\frac{1}{3}}$	$(3,3)_{-\frac{1}{3}}$	$(1,3)_0$	$(3,1)_0$	$(3,3)_{\frac{2}{3}}$		
Q_{ll}	$\mathcal{S}_1$	Ξ	β	$\mathcal{W}$			
Irrep	$(1,1)_1$	$(1,3)_1$	$(1,1)_0$	$(1,3)_0$			

Table 3.6: Single-field extensions of the Standard Model generating Q_x operators at tree level. Here we follow the notation of Ref. [229]. The asterisks indicate fields that only generate the operators that contribute to the β decays at the loop level.

3.2.6 Conclusions

We performed a loop-level analysis of low-energy (semi)leptonic charged current processes in the Standard Model Effective Field Theory, truncated at dimension six. Using the one-loop anomalous dimensions and the corresponding renormalization group equations we have expressed the low-scale effective couplings affecting β decays, $\epsilon_\alpha(\mu_W)$, in terms of the SMEFT

Wilson coefficients at the new-physics scale, Λ. We find that the RGE running generates new significant contributions only for the left-handed effective coupling ϵ_L that shifts the Standard Model $(V-A)\times(V-A)$ operator, while providing only small shifts to the tree-level matching conditions (see Eqs. (3.15)) for the right-handed current, scalar, and tensor operators.

Our main results are given by Eqs. (3.28) and (3.29), which display $\epsilon_L^{(d,s)}(\mu_W)$ in terms of the SMEFT Wilson coefficients $C_n(\Lambda)$, keeping only the effective couplings that contribute with coefficients larger than 10^{-3}. Eq. (3.28), coupled with the experimental input on $\epsilon_L^{(d)}(\mu_W)$ from a recent global analysis of beta decays and other precision measurements [101], provides the general constraint from low-energy charged-current processes on SMEFT effective couplings, at the leading logarithmic accuracy. Turning on the SMEFT couplings one at a time at the reference scale $\Lambda = 5$ TeV, we obtain the constraints displayed in Fig. 3.4 and Table 3.5, which we compare with the sensitivity of other observables. We find that low-energy charged-current processes are generally competitive and provide bounds that do not depend on assumptions about flavor symmetries imposed on the SMEFT couplings. We find that the Wilson coefficients of operators involving the third generation, such as $Q_{qq}^{(1),(3)}$ and $Q_{lq}^{(3)}$, are stringently constrained by low-energy CC processes to be at the permille level, corresponding to a reach of $\Lambda \simeq 8$ TeV. While the current tension with first-row CKM unitarity points to a nonzero combination of SMEFT couplings, further theoretical and experimental scrutiny may shift the central value and will certainly improve confidence in the uncertainties, and thus the robustness of the resulting constraints.

Finally, we have also identified single-field extensions of the Standard Model that contribute to the SMEFT operators, which generate significant effects in beta decays via loops (see Table 3.6). It is interesting to note that the scalar field Υ and vector field $\mathcal{H}$ at tree level only generate the $Q_{qq}^{(1),(3)}$ operators. These extensions, therefore, provide simplified UV scenarios in which the first contributions to low-energy charged-current processes appear at the loop level.

3.3 Loop corrections to the two-body potential of beta decay

Superallowed β decays are pure Fermi transitions, mediated only by the vector component of the weak interaction, and involve no change in nuclear spin or parity. Owing to their simplicity, these decays provide a relatively clean and theoretically well-controlled means of testing the conservation of the vector weak current and determining the CKM matrix element V_{ud}. Currently, the most precise extraction of V_{ud} arises from superallowed decays [234]. However, as discussed in Section 1.1.2, the current global analysis yields $\Delta_{CKM} = -1.48(53) \times 10^{-3}$ a deviation from zero at the $\sim 3\sigma$. To scrutinize this discrepancy and to fully exploit the potential of nuclear beta decay experiments, it is necessary to improve the precision of theoretical calculations.

To address this, we work within the framework of Chiral Perturbation Theory (ChPT), described in Section 2.2. This approach systematically incorporates the symmetries of QCD and allows us to account for higher-order hadronic corrections with controlled uncertainties, thereby enabling CKM unitarity tests at the 10^{-4} level [235, 236]. Refs. [235, 236] set up the framework and computed the two-body weak transition operator to order $G_F\alpha\epsilon_\chi$, where $\epsilon_\chi \sim m_\pi/\Lambda_\chi$. This corresponds to the three-level diagram in Fig. 3.5. However, to test the CKM unitarity at the level of 2×10^{-4} one needs nuclear-structure-dependent corrections to order $G_F\alpha\epsilon_\chi^2$, which is the goal of this project. We set up a computational method to calculate the loop corrections in a two-body potential to a superallowed transition.

Although the project is not yet complete, we have made substantial progress toward its realization. We have identified all diagrams contributing at the required order (~ 50 diagrams), therefore, establishing a comprehensive basis for the calculation. The types of topologies with exemplary diagrams are placed in Appendix B. Building on this, we have initiated the automation of their evaluation using tools such as *FeynOnium*, *FeynCalc*, and *Mathematica*. To test and validate the automated procedure, we have carried out explicit analytic computations of two representative diagrams: one involving photon exchange and pion exchange, and another including two-pion exchange, which requires insertion of the electromagnetic mass splitting. The diagrams are presented in Fig. 3.6. These calculations confirm the consistency of our approach and provide valuable benchmarks for the automated

framework. Work is ongoing to extend these methods to the full set of diagrams, with the ultimate goal of delivering a systematic and reliable calculation at the desired precision.

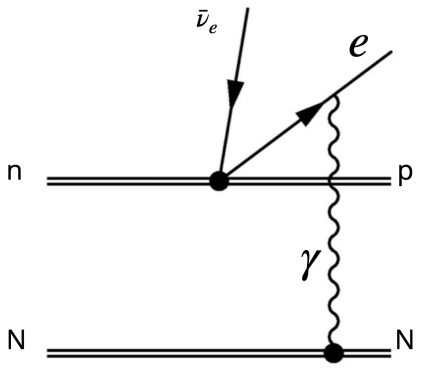

Figure 3.5: Feynman diagram describing the contribution to the two-body potential to beta decay at a loop level.

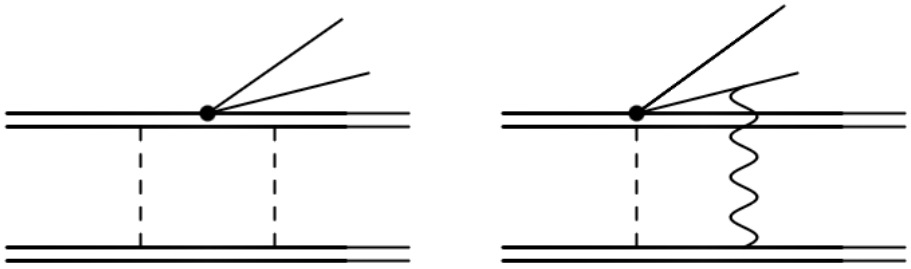

Figure 3.6: Feynman diagrams of loop corrections to two-body potential contributing to superallowed beta decay discussed in this work. The left panel presents two two-pion exchange potential, and the right panel presents one pion exchange and photon exchange potential.

The relevant terms in the chiral Lagrangian with electroweak external sources are

$$\mathcal{L}_{\text{eff}} \supset \frac{1}{2} l_\mu \bar{N}(v^\mu - 2g_A S^\mu)\tau^+ N + \text{h.c.} \tag{3.53}$$

$$+ \frac{\sqrt{2}g_A}{F_\pi}(\bar{N}S^\mu\tau^+ N\,\partial_\mu\pi^+ + \text{h.c.}) + \frac{g_A}{F_\pi}(\bar{N}S^\mu\tau^3 N)\partial_\mu\pi^0 \tag{3.54}$$

$$+ \frac{i}{2\sqrt{2}F_\pi} l_\mu \bar{N}(v^\mu - 2g_A S^\mu)(\tau^3\pi^- - \frac{1}{\sqrt{2}}\pi^0\tau^+)N + \text{h.c.} \tag{3.55}$$

$$+ \frac{i}{\sqrt{2}} l_\mu(\pi^0\partial^\mu\pi^- - \pi^-\partial^\mu\pi^0) + \text{h.c.} \tag{3.56}$$

$$- \frac{F_\pi}{\sqrt{2}} l_\mu \partial^\mu\pi^- + \text{h.c.} \tag{3.57}$$

$$+ (-eA_\mu)\bar{N}v^\mu\frac{1}{2}(1+\tau^3)N \tag{3.58}$$

$$+ (eA_\mu)\bar{e}\gamma_\mu e \tag{3.59}$$

$$- 2e^2F_\pi^2 Z_\pi \pi^+\pi^- \ , \tag{3.60}$$

where $N^T = (p, n)$ are respectively neutron and proton fields, $\tau^a (a = 1, 2, 3)$ are the Pauli matrices acting on isospin space, $2\tau^\pm = \tau_1 \pm i\tau_2$ are the isospin raising and lowering operators, $v^\mu = (1, \vec{0})$ is a unity vector and $S^\mu = (0, \frac{\vec{\sigma}}{2})$ is spin 4-vector. We use the normalization $F_\pi \simeq 92.4$ MeV.

3.3.1 Two-pion exchange

The discussed potential originates from the diagram shown in the left panel of Fig. 3.6. The amplitude from this diagram reads

$$iT_1^{g_v} = \frac{\sqrt{2}G_F V_{ud} e^2 Z_\pi g_A^4 g_v v^\mu}{F_\pi^2} \times [\bar{e}_L\gamma_\mu\nu_L] \times (\delta_{BB'} - \delta_{B3}\delta_{B'3})[(\tau_B\tau^+\tau_A)\otimes(\tau_{B'}\tau_A)]$$
$$\times [(S^\alpha S^\delta)\otimes(S^\beta S^\gamma)] \times \int \frac{d^4l}{(2\pi)^4} \frac{(l-q_2)_\alpha l_\delta (l-q_2)_\beta l_\gamma}{[l^2 - m_\pi^2 + i\epsilon][(l-q_2)^2 - m_\pi^2 + i\epsilon]^2(-v\cdot l + i\epsilon)^2(v\cdot l + i\epsilon)} \ , \tag{3.61}$$

where $p_{1,2}$ are the incoming nucleon momenta, and $p'_{1,2}$ are the outgoing nucleon momenta. Index 1 refers to the upper nucleon line, and 2 denotes the lower nucleon line. The momentum transfers are denoted by $q_{1,2} = p'_{1,2} - p_{1,2}$. Since we are in the potential region (where $q^0 \sim \frac{m_\pi^2}{m_N} \ll |\vec{q}| \sim m_\pi$) we drop the external momenta on virtual nucleon propagators. We also drop the external leptonic momenta entirely due to their soft scaling. The spin

structure can be simplified down to a sum of terms with at most one spin vector acting on each nucleon using commutation and anticommutation relations.

$$[S_\mu, S_\nu] = i\epsilon^{\mu\nu\alpha\beta} v_\alpha S_\beta \tag{3.62}$$

$$\{S_\mu, S_\nu\} = \frac{1}{2}(g^{\mu\nu} - v^\mu v^\nu) \tag{3.63}$$

$$\implies (S^\alpha S^\delta) \otimes (S^\beta S^\gamma) = (\frac{1}{2}[i\epsilon^{\alpha\delta cd} v_c S_d + \frac{1}{2}(g^{\alpha\delta} - v^\alpha v^\delta)]) \otimes (\frac{1}{2}[i\epsilon^{\beta\gamma ef} v_e S_f + \frac{1}{2}(g^{\beta\gamma} - v^\beta v^\gamma)]) \tag{3.64}$$

The isospin structure can be similarly simplified down to a sum of terms with at most one isospin matrix acting on each nucleon. Since we are dealing with single beta decay, we know only the $1 \otimes \tau^+$ and $\tau^3 \otimes \tau^+$ structures survive, so it is convenient to rewrite the above sum in this basis.

$$[\tau_A, \tau_B] = 2i\epsilon^{ABC}\tau^C$$

$$\{\tau_A, \tau_B\} = 2\delta_{AB} \tag{3.65}$$

$$\tau_{B'}\tau_A = i\epsilon_{B'A\gamma}\tau_\gamma + \delta_{B'A}$$

$$\tau_B\tau_C\tau_A = \delta_{BC}\tau_A + \delta_{CA}\tau_B - \delta_{BA}\tau_C + i\epsilon_{BCA} \tag{3.66}$$

$$\begin{aligned}\implies (\delta_{BB'} - \delta_{B3}\delta_{B'3})[(\tau_B\tau_C\tau_A) \otimes (\tau_{B'}\tau_A)] &= (\delta_{BB'} - \delta_{B3}\delta_{B'3}) \\ &\times [\ i\epsilon_{B'A\gamma}\delta_{BC}(\tau_A \otimes \tau_\gamma) + i\epsilon_{B'C\gamma}(\tau_B \otimes \tau_\gamma) \\ &- i\epsilon_{B'B\gamma}(\tau_C \otimes \tau_\gamma) + (\delta_{BB'}\delta_{C\gamma} - \delta_{B\gamma}\delta_{CB'})(1 \otimes \tau_\gamma) \\ &+ \delta_{BC}(\tau_{B'} \otimes 1) + \delta_{CB'}(\tau_B \otimes 1) - \delta_{BB'}(\tau_C \otimes 1) \\ &+ i\epsilon_{BCB'}(1 \otimes 1)]\end{aligned} \tag{3.67}$$

$$\implies (\delta_{BB'} - \delta_{B3}\delta_{B'3})[(\tau_B\tau_+\tau_A) \otimes (\tau_{B'}\tau_A)] = 1 \otimes \tau^+ - \tau_3 \otimes \tau^+ \tag{3.68}$$

$$\text{N.B. } \epsilon_{+AB} = \frac{1}{2}(\epsilon_{1AB} + i\epsilon_{2AB})$$

$$\delta_{+3} = 0 \tag{3.69}$$

We have thus factorized the amplitude into a product of a leptonic bilinear, isospin terms, spin terms, and a momentum space tensor loop integral. The spin terms that have exactly one spin four vector can always be neglected between $0^+ \to 0^+$ states by parity and angular

momentum arguments outlined in a later section. Therefore, the amplitude becomes:

$$
\begin{aligned}
iT_1^{g_v} = & \frac{\sqrt{2}G_F V_{ud} e^2 Z_\pi g_A^4 g_v v^\mu}{4F_\pi^2} \times [\bar{e}_L \gamma_\mu \nu_L] \times (1-\tau_3) \otimes \tau^+ \\
& \times \Bigg[(-\epsilon^{\alpha\delta cd} \epsilon^{\beta\gamma ef} v_c v_e q_{2\alpha} q_{2\beta} S_d S_f) \cdot \\
& \int \frac{d^4 l}{(2\pi)^4} \frac{l_\delta l_\gamma}{[l^2 - m_\pi^2 + i\epsilon][(l-q_2)^2 - m_\pi^2 + i\epsilon]^2 (-v\cdot l + i\epsilon)^2 (v \cdot l + i\epsilon)} \\
& + (\frac{1}{4}\mathbb{I} \otimes \mathbb{I}) \cdot \int \frac{d^4 l}{(2\pi)^4} \frac{[(\vec{l} - \vec{q_2}) \cdot \vec{l}]^2}{[l^2 - m_\pi^2 + i\epsilon][(l-q_2)^2 - m_\pi^2 + i\epsilon]^2 (-v\cdot l + i\epsilon)^2 (v \cdot l + i\epsilon)} \Bigg]
\end{aligned}
\tag{3.70}
$$

The first tensor loop integral, after extracting out the nucleon pole term, can be solved in dimensional regularization by combining the relativistic and nonrelativistic propagators and shifting the loop momenta. In general this integral can be decomposed as follows: $\mathcal{I}_{\delta\gamma} = c_1 q_{2\delta} q_{2\gamma} + c_2 q_{2\delta} v_\gamma + c_3 v_\delta q_{2\gamma} + c_4 v_\delta v_\gamma + c_5 g^{\delta\gamma}$. The coefficients are scalars and depend on the external scales: $c_i = c_i(v \cdot q_2 \sim \frac{\vec{q_2^2}}{2m_N} \approx 0, q_2^2 \sim -|\vec{q_2}|^2, m_\pi^2)$.

The second loop integral is a little trickier since the numerator involves the square of the scalar product of three-momenta, which is not a Lorentz invariant quantity. One way to solve this integral is to write the numerator as a sum of inverse propagators and solve the sum of scalar integrals that result. Another way is to do the integration over l_0 first using the method of residues and then over $d^3\vec{l}$ using standard formulae.

The last steps are to simplify the product of epsilon tensors to a sum of products of Kronecker deltas and take the non-relativistic limit to arrive at the quantum mechanical potential. We also need to remember the contribution due to the S_2 matrix element, but not the exchange diagrams, since the distinguishability of particles is put in by hand in quantum mechanics, unlike in the scattering formalism of QFT, where it is inbuilt. Putting these pieces together

yields:

$$T_{\rm lep}\hat{V}_W^{\rm 2b} = \left[\frac{-\sqrt{2}G_F V_{ud}e^2}{(4\pi F_\pi)^2}\right][Z_\pi \pi g_A^4 g_v \delta^{\mu 0}] \times [\bar{e}_L \gamma_\mu \nu_L] \times [\frac{(1-\tau_3)^{(1)}}{2} \otimes \tau^{+(2)} + \frac{(1-\tau_3)^{(1)}}{2} \otimes \tau^{+(2)}] \times \left[\frac{|\vec{q}|^2(\vec{\sigma}^{(1)}\cdot\vec{\sigma}^{(2)}) - (\vec{\sigma}^{(1)}\cdot\vec{q})(\vec{\sigma}^{(2)}\cdot\vec{q})}{4m_\pi[|\vec{q}|^2+4m_\pi^2]} + (\mathbb{I}\otimes\mathbb{I}) f(|\vec{q}|, m_\pi^2)\right] \tag{3.71}$$

$$T_{\rm lep}\hat{V}_W^{\rm 2b} = \left[\frac{-\sqrt{2}G_F V_{ud}e^2}{(4\pi F_\pi)^2}\right][Z_\pi \pi g_A^4 g_v \delta^{\mu 0}] \times [\bar{e}_L \gamma_\mu \nu_L] \times [\frac{(1-\tau_3)^{(1)}}{2} \otimes \tau^{+(2)} + \frac{(1-\tau_3)^{(1)}}{2} \otimes \tau^{+(2)}] \times \left[\frac{|\vec{q}|^2(\vec{\sigma}^{(1)}\cdot\vec{\sigma}^{(2)} + \frac{1}{2}S^{(12)})}{6m_\pi[|\vec{q}|^2+4m_\pi^2]} + (\mathbb{I}\otimes\mathbb{I}) f(|\vec{q}|, m_\pi^2)\right] \tag{3.72}$$

$$S^{(12)} = \vec{\sigma}^{(1)}\cdot\vec{\sigma}^{(2)} - 3(\vec{\sigma}^{(1)}\cdot\hat{q})(\vec{\sigma}^{(2)}\cdot\hat{q})$$
$$f(|\vec{q}|, m_\pi^2) = \frac{[(|\vec{q}|^2+4m_\pi^2)^2(4m_\pi \tan^{-1}[\frac{2m_\pi}{|\vec{q}|}] - 2m_\pi\pi) - 28m_\pi^4|\vec{q}| - 9m_\pi^2|\vec{q}|^3 - |\vec{q}|^5]}{16m_\pi|\vec{q}|(|\vec{q}|^2+4m_\pi^2)^2} \tag{3.73}$$

3.3.2 One pion and one photon exchange

The discussed potential originates from the diagram shown in the right panel of Fig. 3.6.

We can similarly factorize the photon exchange diagram as follows:

$$iT_1^{\pi^+} = \frac{\sqrt{2}G_F V_{ud}e^2 g_A v^\delta}{F_\pi^2} \times [\bar{e}\gamma_\delta\gamma_\beta\gamma_\mu P_L \nu] \times [\tau_3 \otimes Q\tau^+] \times [(g_v v^\mu - 2g_A S^\mu)\otimes S_\nu] \times \int \frac{d^4l}{(2\pi)^4} \frac{l^\beta (l-q_2)^\nu}{[(l-q_2)^2 - m_\pi^2 + i\epsilon](-v\cdot l + i\epsilon)[l^2+i\epsilon]^2} \tag{3.74}$$

Like before, the tensor integral can be decomposed as: $\mathcal{I}^{\beta\nu} = c_1 q_2^\beta q_2^\nu + c_2 q_2^\beta v^\nu + c_3 v^\beta q_2^\nu + c_4 v^\beta v^\nu + c_5 g^{\beta\nu}$. In this case, the coefficients c_2 and c_4 can be neglected since $S\cdot v = 0$. Furthermore, we can neglect the term proportional to g_v since the spin term contains exactly one spin 4-vector which vanishes between $0^+ \to 0^+$ states by angular momentum and parity selection rules. We can in turn ignore the c_4 term then because its a vector operator with respect to the first nucleon's Hilbert space.

The leptonic structure is more complicated than the previous example, involving the product of three gamma matrices. It therefore needs to be reduced using the identity: $\gamma_\mu\gamma_\nu\gamma_\rho = \eta_{\mu\nu}\gamma_\rho + \eta_{\nu\rho}\gamma_\mu - \eta_{\mu\rho}\gamma_\nu - i\epsilon_{\sigma\mu\nu\rho}\gamma_\sigma\gamma^5$. We then contract this expansion with the remaining c_1 and c_5 terms. The epsilon term creates vector cross product operators in the nucleonic Hilbert space (for the c_1 term it is a momentum cross spin operator and for the c_5 term it is a spin cross spin operator). After these simplifications and taking the non-relativistic limit the resulting potential is:

$$\begin{aligned} T_{\rm lep}\hat{V}_W^{\rm 2b} &= \frac{-\sqrt{2}G_F V_{ud} e^2 g_A \delta^{\mu 0}}{F_\pi^2} \times [\bar{e}_L\gamma_\mu\nu_L] \times [\tau_3^{(1)} \otimes \tau^{+(2)} + \tau^{+(1)} \otimes \tau_3^{(2)}] \\ &\quad \times [g(m_\pi^2, |\vec{q}|)\frac{1}{2}\vec{\sigma}^{(1)} \cdot \vec{q} + h(m_\pi^2, |\vec{q}|)\frac{1}{4}\vec{\sigma}^{(1)} \cdot \vec{\sigma}^{(2)}] \\ g(m_\pi^2, |\vec{q}|) &= \frac{3m_\pi|\vec{q}| - (3m_\pi^2 + |\vec{q}|^2)\cot^{-1}[\frac{m_\pi}{|\vec{q}|}]}{32\pi|\vec{q}|^5} \qquad (3.75) \\ h(m_\pi^2, |\vec{q}|) &= \frac{m_\pi|\vec{q}| + (|\vec{q}|^2 - m_\pi^2)\cot^{-1}[\frac{m_\pi}{|\vec{q}|}]}{32\pi|\vec{q}|^3} \qquad (3.76) \\ & \qquad (3.77) \end{aligned}$$

3.3.3 Conclusion

In summary, we have established the framework necessary to compute nuclear-structure dependent corrections to superallowed β decays at order $G_F\alpha\epsilon_\chi^2$, which are essential for probing CKM unitarity tests to the 2×10^{-4} level. While the project is still in progress, we have identified all ~ 50 contributing diagrams and implemented the first steps toward their automated evaluation.

Chapter 4

NEW CLASS OF THREE-NUCLEON FORCES AND THEIR IMPLICATIONS

The development of EFT methods for low-energy nuclear processes has greatly advanced our understanding of nuclei and dense matter in neutron stars [111, 112]. Building on Weinberg's work [102, 113], chiral EFT provides a systematic framework consistent with QCD symmetries, exploiting the separation of energy scales. It describes nucleon interactions at momenta comparable to the pion mass but well below heavier meson masses, organizing operators in a momentum expansion with higher-order terms suppressed by powers of p/Λ_χ or m_π/Λ_χ. The corresponding low-energy constants (LECs) are fixed from experiment. A major advantage of chiral EFT is the natural inclusion of many-body forces in a hierarchy consistent with the two-nucleon force. The three-nucleon force (3NF) is essential for reproducing binding energies, radii, and the saturation properties of nuclear matter [111, 114, 115], and for a realistic equation of state of neutron stars [8, 237]. For typical cutoffs $\Lambda_\chi = 450 - 500$ MeV, 3N forces stabilize both nuclei and neutron stars; without them, nuclear saturation would occur at too high density, and neutron stars would be too light and small.

The leading 3NF enters at next-to-next-to-leading order (N2LO) [161, 162], comprising a long-range two-pion exchange, an intermediate-range one-pion exchange, and a short-range contact term. The LECs c_D and c_E for the latter two can be constrained from few-body observables such as light-nucleus binding energies, radii, tritium beta decay, and $n - d$ scattering[133, 162–164]. The long-range Fujita–Miyazawa term [167] is determined independently from pion–nucleon scattering.

In this chapter, we identify new loop contributions to the 3N force, which arise from operators that involve four nucleon fields and two pion fields. One of these operators is related by chiral symmetry to the quark mass-dependent four-nucleon contact operator, which can be interpreted as the nuclear σ term [238].

4.1 Problems with the conventional power counting

Weinberg's power counting scheme works remarkably well in many nuclear applications; however, it is not universally valid. Kaplan, Savage, and Wise demonstrated in Ref. [20] that Weinberg's approach can fail in certain channels, particularly due to issues with renormalization when pions are included perturbatively. Namely, Fig. 4.1 shows the leading-order contribution to the NN scattering amplitude in the KSW scheme. It consists of two insertions of the contact interaction C_0 and two vertices involving one pion and two nucleons.

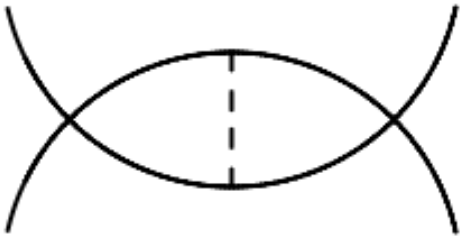

Figure 4.1: A divergent Feynman diagram necessitating the promotion of the d_2 operator. The diagram features two insertions of the contact interaction C_0, along with two pion-nucleon vertices involving one pion and two nucleons each.

This diagram in ${}^1S_0$ channel is ultraviolet divergent and therefore requires introducing a quark-mass-dependent four-nucleon counterterm in the leading order Lagrangian.

In terms of nucleons and the chiral fields, $N = (p, n)^T$, $\chi_+ = u^\dagger \chi u^\dagger + u \chi^\dagger u$, $\chi = 2B_0 m_q$, and $U = u^2 = \exp(i\tau^a \pi^a / f_\pi)$ (where $f_\pi = 92.4$ MeV is the pion decay constant), and working in the isospin limit, the required interactions can be written in chiral covariant form

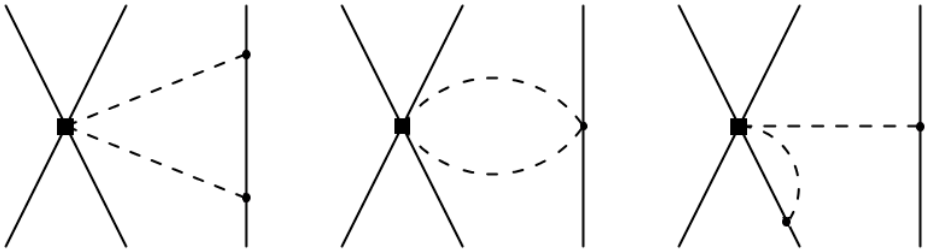

Figure 4.2: Diagrams that contribute to the 3NF due to the 2π-exchange interaction induced by insertions of the D_2 operator (black circle). Solid lines represent nucleons and dashed lines represent pions.

as follows [239],

$$\begin{aligned}
\mathcal{L} &= \left[d_2^S\,\bar{N}N\,\bar{N}N + d_2^T\bar{N}\vec{\sigma}N\,\bar{N}\vec{\sigma}N\right]\,\langle\chi_+\rangle\,, \\
&= -\frac{1}{4}D_2\,(N^TP_iN)^\dagger\,(N^TP_iN)\,\langle\chi_+\rangle \\
&\quad -\frac{1}{4}D_2'\,(N^TP_i'N)^\dagger\,(N^TP_i'N)\,\langle\chi_+\rangle\,, \qquad (4.1)\\
\langle\chi_+\rangle &= 4m_\pi^2\left(1-\frac{\pi^a\pi^b}{2f_\pi^2}\delta^{ab}+\cdots\right)\,, \qquad (4.2)
\end{aligned}$$

where σ^i (τ^i) are the (iso)spin Pauli matrices, while $P_i = \tau_2\tau^i\sigma_2/\sqrt{8}$ and $P_i' = \sigma_2\sigma^i\tau_2/\sqrt{8}$ are the ${}^1S_0$ and ${}^3S_1$ partial-wave projection operators, respectively. The scalar/tensor couplings (d_2^S, d_2^T) and the partial-wave couplings (D_2 and D_2') are related by

$$d_2^S = -\frac{D_2+3D_2'}{32}\,, \qquad d_2^T = \frac{D_2-D_2'}{32}\,. \qquad (4.3)$$

D_2 and D_2' could be determined from pion-nucleus scattering or lattice QCD [240], but are currently poorly constrained. In this work we estimate D_2 based on the scaling required by the renormalization group equation [20]

$$\frac{d}{d\ln\mu}\left[\frac{m_\pi^2 D_2}{\tilde{C}_0^2}\right] = \frac{g_A^2 m_\pi^2 m_N^2}{64\pi^2 f_\pi^2}\,, \qquad (4.4)$$

where $\tilde{C}_0$ is the leading-order contact interaction in the ${}^1S_0$ channel and μ is the renor-

malization scale in dimensional regularization [1]. Similar results for the logarithmic scaling with the cutoff hold in other regularization schemes [242].

At a generic scale the above relation implies

$$D_2(\mu) \approx \frac{g_A^2 m_N^2}{64\pi^2 f_\pi^2}\, \tilde{C}_0^2(\mu)\,. \tag{4.5}$$

More generally, we define the dimensionless ratio

$$\xi = \left| \frac{D_2}{\tilde{C}_0^2} \right| , \tag{4.6}$$

note that Eq. 4.5 predicts $\xi = 0.26$, and explore the range $\xi \sim 0.1 - 0.5$. For typical values of $\tilde{C}_0$, this corresponds to $|D_2| < 1/(5 f_\pi^4)$. In [243], the authors introduce a related dimensionless ratio $\eta = |D_2 m_\pi^2/\tilde{C}_0|$ and suggest the range $1/15 < \eta < 1/3$ to ensure consistency with a perturbative treatment of the pion exchange [244, 245]. Although the LO contact term can vary by an $\mathcal{O}(1)$ factor depending on the chosen regulator and cutoff, the estimate $\tilde{C}_0 \approx 1/m_\pi^2$ is consistent with commonly employed regularization schemes, see e.g. Refs. [103, 165, 246–249]. Since $\xi = \eta/(m_\pi^2 \tilde{C}_0)$, the range we explore here is roughly compatible with the range suggested in [243]. In Chiral EFT, for typical Λ employed in calculations, $|\tilde{C}_0| \sim 1/m_\pi^2 \approx 5$ fm^2, and $\xi < 0.5$ predicts $|D_2| \lesssim 10$ fm^4.

When pions are treated non-perturbatively, the LECs associated with the spin-triplet operators are not required for renormalization of scattering amplitudes to leading order [250]. For this reason, we assume $D_2' \ll D_2$ and neglect the contribution of the spin-triplet operators.

The D_2 operator induces three-nucleon potentials through the Feynman diagrams shown in Fig. 4.2. In momentum space, we find

$$V_{ijk}^{i'j'k'}(\vec{q}_1, \vec{q}_2, \vec{q}_3) = \frac{9 g_A^2 D_2 m_\pi^3}{128\pi f_\pi^4} \kappa_{ij}^{i'j'} \delta_{kk'}\, \mathcal{I}\left(\frac{\vec{q}_3^{\,2}}{4m_\pi^2}\right) , \tag{4.7}$$

where $\kappa_{ij}^{i'j'} = (d_2^S \delta_{ii'}\delta_{jj'} + d_2^T \vec{\sigma}_{i'i} \cdot \vec{\sigma}_{j'j})/(d_2^S - 3d_2^T)$, and

$$\mathcal{I}(b) = \frac{2}{3}\left(1 + \left(\frac{1}{2\sqrt{b}} + \sqrt{b}\right)\tan^{-1}(\sqrt{b})\right) . \tag{4.8}$$

[1] Note that Ref. [241] under-estimates the anomalous dimension in the RHS of Eq. (4.4) by a factor of four. Our direct calculation agrees with the result of Ref.[20]

Here $q_i = p_i' - p_i$ is the exchanged momentum of nucleon i, and $\sum q_i = 0$.

Here we discuss the coordinate-space potentials induced by D_2 and F_2. Performing the Fourier transform of the momentum-space expressions in dimensional regularization (DR) or regulating the integrals with a small imaginary part of r, we obtain

$$\begin{aligned} V^{ijk}_{i'j'k'}(\vec{r}_1,\vec{r}_2,\vec{r}_3) &= -\frac{9g_A^2 D_2 m_\pi^3}{128\pi f_\pi^4}\kappa^{i'j'}_{ij}\,\delta_{kk'} \\ &\quad \times\delta^3(\vec{r}_2-\vec{r}_1) f(|\vec{r}_3-\vec{r}_1|)\,, \\ f(r)\Big|_{\rm DR} &= -\frac{e^{-2z}}{6\pi z r^3}(1+z)^2\,, \\ f(r)\Big|_{{\rm Im}(r)} &= f(r)\Big|_{\rm DR} + \frac{2}{3}\delta^3(r)\,, \end{aligned} \tag{4.9}$$

in the case of D_2, while the potential for F_2 can be written as

$$\begin{aligned} V^{ijk}_{i'j'k'}(\vec{r}_1,\vec{r}_2,\vec{r}_3) &= \frac{15g_A^2 F_2 m_\pi^3}{128\pi f_\pi^4}\bar{\kappa}^{i'j'}_{ij}\,\delta_{kk'} \\ &\quad \times\delta^3(\vec{r}_2-\vec{r}_1) g(|\vec{r}_3-\vec{r}_1|)\,, \\ g(r)\Big|_{\rm DR} &= \frac{e^{-2z}}{10\pi r^3 z^3}\left(6+12z+10z^2+4z^3+z^4\right) \\ &\quad +\frac{4}{15}\delta^3(r)\,, \\ g(r)\Big|_{{\rm Im}(r)} &= g(r)\Big|_{\rm DR} + \frac{2}{5}\left[1-\frac{1}{2m_\pi^2}\nabla^2\right]\delta^3(r)\,, \end{aligned} \tag{4.10}$$

with $\bar{\kappa}^{i'j'}_{ij} = (f_2^S\delta_{ii'}\delta_{jj'} + f_2^T\vec{\sigma}_{i'i}\cdot\vec{\sigma}_{j'j})/(f_2^S - 3f_2^T)$ and $z = m_\pi r$. Here $\vec{r}_i$ denotes the position of nucleon i with respect to the center of mass, $\vec{x}$, which is related to the absolute position of nucleon i, by $\vec{x}_i = \vec{x} + \vec{r}_i$, with $\vec{r}_1 + \vec{r}_2 + \vec{r}_3 = 0$ and $\vec{x} = \frac{\vec{x}_1+\vec{x}_2+\vec{x}_3}{3}$.

The effect of the above coordinate-space potentials is described by the following Lagrangian,

$$\begin{aligned} \mathcal{L}(t,\vec{x}) \;\supset\; &-\int d^3\vec{r}_1 d^3\vec{r}_2 \bar{N}_{i'}(x_1)\bar{N}_{j'}(x_2)\bar{N}_{k'}(x_3) \\ &\times V^{i'j'k'}_{ijk}(\vec{r}_1,\vec{r}_2,\vec{r}_3) N_k(x_3) N_j(x_2) N_i(x_1)\,, \end{aligned} \tag{4.11}$$

where the indices denote (iso)spin, while x_i and r_i have the same meaning as above. The relation to the momentum-space potentials discussed above is given by,

$$V^{ijk}_{i'j'k'}(\vec{r}_1,\vec{r}_2,\vec{r}_3) = \int_{\vec{q}_2,\vec{q}_3} e^{i\sum_i \vec{q}_i\cdot\vec{r}_i} V^{ijk}_{i'j'k'}(\vec{q}_1,\vec{q}_2,\vec{q}_3)\,. \tag{4.12}$$

These integrals are singular, which leads to slightly different expressions in Eqs. (4.9) and (4.10) depending on the choice of regulator.

Finally, in perhaps more familiar notation, these potentials enter the Lippmann-Schwinger equation as

$$\begin{aligned} V_{D2} &= \frac{9g_A^2 m_\pi^3}{16\pi f_\pi^4} \sum_{I\neq J\neq K} \delta^3(\vec{r}_{JI}) f(|\vec{r}_{KI}|) \\ &\quad \times \left[\mathbf{1}^{(I)}\mathbf{1}^{(J)} d_2^S + \boldsymbol{\sigma}^{(I)}\cdot\boldsymbol{\sigma}^{(J)} d_2^T\right] , \\ V_{F2} &= -\frac{15g_A^2 m_\pi^3}{16\pi f_\pi^4} \sum_{I\neq J\neq K} \delta^3(\vec{r}_{JI}) g(|\vec{r}_{KI}|) \\ &\quad \times \left[\mathbf{1}^{(I)}\mathbf{1}^{(J)} f_2^S + \boldsymbol{\sigma}^{(I)}\cdot\boldsymbol{\sigma}^{(J)} f_2^T\right] , \end{aligned} \tag{4.13}$$

with a sum over nucleons I, J, and K and $\vec{r}_{IJ} = \vec{r}_I - \vec{r}_J$.

The D_2 scaling in (4.5) implies the above potentials appear at N^{3}LO, one order below the leading N^{2}LO 3N force. This expectation assumes a loop suppression of $\sim 1/(4\pi)^2$, even though possibly large numerical factors and powers of π can be hard to predict [2]. Indeed, the result of Eq. (D.1) is larger than the naive expectation by at least a factor of π. As we will see later, the D_2 contributions also have a stronger momentum dependence than the leading 3N force, giving further enhancement at large densities.

For completeness, the amplitude of the four-nucleon potential generated by the d_2 operator is also presented below.

$$i\mathcal{T} = -i4(\bar{N}N)^4 \, \frac{d_2 g_A^2}{F^4} \, \frac{S\cdot q_2 \tau^d \; S\cdot q_1 \tau^a}{((p_4-p_4')^2 - m_\pi^2)((p_1-p_1')^2) - m_p i^2)} \, , \tag{4.14}$$

where p_1 and p_4 are the incoming momenta of the 'outer' legs, and p_1' and p_4' are the corresponding outgoing momenta. Consistent with the KSW argument, this diagram also requires promotion by two orders in the EFT power counting.

---

[2]For example, numerically large and/or π-enhanced contributions have been encountered in $\pi - N$ and π-deuteron scattering [251–258]. However, there is no general power-counting that can capture such enhancements, without explicit calculation.

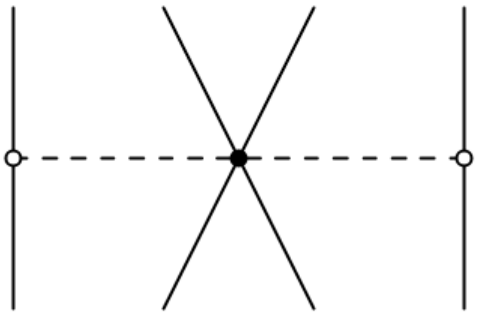

Figure 4.3: 2π-exchange interaction with d_2 operator contributing to 4N potential

4.2 The 3N forcess from derivative terms

The consistent renormalization of pion scattering off two-nucleons in the spin-singlet channel also requires two other operators that describe the coupling of pions to two nucleons involving derivatives of the pion field [259, 260]. Following Ref. [260] we write these additional $\pi^2 NN$ operator structures that are independent of the pion mass [3]

$$\begin{aligned}
\mathcal{L}_2 &= \frac{1}{4}\left[E_2\langle (v\cdot u)^2\rangle + F_2\langle u\cdot u - (v\cdot u)^2\rangle\right] \\
&\times \left(N^T P_i N\right)^\dagger \left(N^T P_i N\right) \\
&+ \frac{1}{4}\left[E_2'\langle (v\cdot u)^2\rangle + F_2'\langle u\cdot u - (v\cdot u)^2\rangle\right] \\
&\times \left(N^T P_i' N\right)^\dagger \left(N^T P_i' N\right)
\end{aligned} \tag{4.15}$$

where $u_\mu = i(u\partial_\mu u^\dagger - u^\dagger\partial_\mu u)/2$. Expanding u and retaining only the leading terms we find that

$$\begin{aligned}
\mathcal{L}_2 &= -\frac{2}{f_\pi^2}\sum_{\alpha=S,T}(\bar{N}\Gamma_\alpha N)\cdot(\bar{N}\Gamma_\alpha N) \\
&\times \left[e_2^\alpha(\partial_0\pi^A)(\partial_0\pi^A) - f_2^\alpha(\vec{\nabla}\pi^A)(\vec{\nabla}\pi^A)\right] + \mathcal{O}(\pi^4)
\end{aligned} \tag{4.16}$$

[3] In principle, an isospin-tensor operator of the form, $(N^T P_a N)(N^T P_b N)^\dagger\langle u_\mu\tau^c\rangle\langle u^\mu\tau^d\rangle(3\delta_{ac}\delta_{bd} - \delta_{ab}\delta_{cd})$ appears in the ${}^1S_0$ channel, in addition to the singlet term, $\sim\delta_{ab}\delta_{cd}$, in Eq. (4.15). In fact, we find that this operator has the same anomalous dimension as that of Eq. (4.18). We do not discuss this term any further here, as the contributions to the 3N force are only sensitive to the singlet operator.

where $\Gamma_S = 1$ and $\Gamma_T = \vec{\sigma}$. The S,T couplings are related to the partial-wave basis in analogy to Eq. (4.3)

$$\begin{aligned} e_2^S &= -\frac{E_2 + 3E_2'}{32}\,, \quad e_2^T = \frac{E_2 - E_2'}{32} \\ f_2^S &= -\frac{F_2 + 3F_2'}{32}\,, \quad f_2^T = \frac{F_2 - F_2'}{32}\,. \end{aligned} \tag{4.17}$$

We find the following renormalization group equations (RGEs) for the ${}^1S_0$ operators (see Ref. [260] for the relevant diagrams in the ${}^3S_1$ channel)

$$\frac{d}{d\ln\mu}\left[\frac{X}{\tilde{C}_0^2}\right] = \gamma_X \left(\frac{m_N}{4\pi f_\pi}\right)^2\,, \tag{4.18}$$

with $X \in \{E_2, F_2\}$, $\gamma_{E_2} = -(1+g_A^2)/3$, and $\gamma_{F_2} = -g_A^2/3$. Since its RGE is similar to that of D_2, in what follows we will explore the same range for the size of F_2, namely, $|F_2| \leq 1/(5f_\pi^4)$.

The 3N potential can be calculated as in the case of the D_2 operator, and in momentum space, we find that

$$\begin{aligned} V_{ijk}^{i'j'k'}(\vec{q}_1,\vec{q}_2,\vec{q}_3) &= -\frac{15 g_A^2 m_\pi^3}{16\pi f_\pi^4}\delta_{kk'}\mathcal{J}\left(\frac{\vec{q}_3^{\,2}}{4m_\pi^2}\right) \\ &\times \left(f_2^S \delta_{ii'}\delta_{jj'} + f_2^T \vec{\sigma}_{i'i}\cdot\vec{\sigma}_{j'j}\right), \end{aligned} \tag{4.19}$$

where

$$\mathcal{J}(b) = \frac{3}{5}\left((1+2b)\mathcal{I}(b) + \frac{2}{3}\right)\,, \tag{4.20}$$

$q_i = p_i' - p_i$ is the exchanged momentum of nucleon i, and $\sum q_i = 0$. We neglect the contribution from the E_2 operator because it is proportional to the kinetic energy of the nucleons [4].

4.3 Neutron and Nuclear Matter

To assess the importance of the D_2 and F_2 terms in the 3N force, we estimate their contributions to the energy per particle in uniform neutron and nuclear matter in perturbation

[4] One might expect these contributions to become comparable to D_2 for Fermi momenta of $\mathcal{O}(300)$ MeV, at which point $E_{\rm kin}^2 \sim m_\pi^2$. However, explicit calculation shows that the E_2 terms only become comparable for significantly larger Fermi momenta.

theory. We shall assume that the Fermi Gas (FG) reference state well describes the momentum distribution of nucleons in the ground state. The interaction energy density is obtained by calculating the matrix element of the potential in Eq. (D.1) in the FG ground state and contracting the nucleon fields through,

$$\langle T\left[N_i(y)\bar{N}_j(x)\right]\rangle = \int_q e^{iq\cdot(x-y)}\left[\frac{i}{v\cdot q+i\epsilon}-2\pi\delta(v\cdot q)\theta(k_f-|\vec{q}|)\right]\delta_{ij}\,. \tag{4.21}$$

Accounting for all possible contractions, we find

$$\begin{aligned}\langle\mathcal{H}(0)\rangle &= \int_{\vec{p}_1,\vec{p}_2,\vec{p}_3}\theta(k_f-|\vec{p}_1|)\theta(k_f-|\vec{p}_2|)\theta(k_f-|\vec{p}_3|)\\ &\times\Bigg[V^{ijk}_{ijk}(0,0,0)-V^{ikj}_{ijk}(0,\vec{p}_{32},\vec{p}_{23})\\ &+V^{jki}_{ijk}(\vec{p}_{21},\vec{p}_{32},\vec{p}_{13})+V^{kij}_{ijk}(\vec{p}_{31},\vec{p}_{12},\vec{p}_{21})\\ &-V^{kji}_{ijk}(\vec{p}_{31},0,\vec{p}_{13})-V^{jik}_{ijk}(\vec{p}_{21},\vec{p}_{12},0)\Bigg]\,,\end{aligned} \tag{4.22}$$

where the second line results from contracting at least one of the nucleon lines with itself (leading to zero exchanged momentum), while each $N(x_i)$ is contracted with a different nucleon, $\bar{N}(x_{j\neq i})$, in the last line. In neutron matter the i,j,k indices only run over the spins, while they also run over isospin in symmetric matter. The momentum integrals can be performed and we find that the energy per particle in neutron and symmetric matter due to the potential in (D.1) are given by

$$\begin{aligned}E^D_{\rm NM} &= -\frac{g_A^2m_\pi^9D_2}{8960\pi^5f_\pi^4}\Bigg[4u^5(7+3u^2)\cot^{-1}(1/u)\\ &+ 2(3+7u^2)\log(1+u^2)\\ &- u^2(6+11u^2+23u^4)\Bigg]\,,\end{aligned} \tag{4.23}$$

$$\frac{E^D_{\rm SM}}{A} = \frac{3(D_2+D_2')}{2D_2}\left(E^D_{\rm NM}+\frac{9g_A^2m_\pi^3D_2}{1024\pi f_\pi^4}n_B^2\right)\,, \tag{4.24}$$

respectively. Here $u=k_F/m_\pi$, and $k_F=(3\pi^2n_n)^{1/3}$ in neutron matter and in symmetric matter $k_F=(3\pi^2n_B/2)^{1/3}$. The energy per particle due to the potential in (D.3) takes the

form

$$\begin{aligned} E^F_{\rm NM} &= -\frac{g_A^2 m_\pi^9 F_2}{241920\pi^5 f_\pi^4}\Big[u^2\Big(138+630\pi u-735u^2 \\ &- 587u^4+240u^6-1260u\cot^{-1}(u) \\ &+ 12u^3(63+54u^2+20u^4)\tan^{-1}(u)\Big) \\ &- 6(23+99u^2)\log(1+u^2)\Big]\,, \end{aligned} \tag{4.25}$$

$$E^F_{\rm SM} = \frac{3(F_2+F_2')}{2F_2}\left(E^F_{\rm NM}-\frac{15g_A^2m_\pi^3n_B^2}{1024\pi f_\pi^4}F_2\right)\,. \tag{4.26}$$

We can compare the above terms with the contributions of the usual three-body potential in Eqs (2.48), (2.49) and (2.50), by plugging it into Eq. (4.22). We start with the potential induced by $c_{1,3}$, which are the only couplings that contribute to both symmetric and neutron matter. Whenever a nucleon line with a πN vertex, $\sim g_A$, is contracted with itself, this leads to terms proportional to $\mathrm{Tr}(\sigma)=0$, so that only three of the contractions in Eq. (4.22) survive, two of which are equivalent. This gives

$$\begin{aligned} \langle\mathcal{H}(0)\rangle_{c_{1,3}} = -\eta_1\frac{g_A^2}{F^4}\int_{\vec{p}_1,\vec{p}_2,\vec{p}_3}\theta(k_f-|\vec{p}_1|)\theta(k_f-|\vec{p}_2|)\theta(k_f-|\vec{p}_3|)\Bigg[\eta_2(\vec{q}_1-\vec{q}_2)^2 \\ \frac{2m_\pi^2c_1+c_3(\vec{q}_1-\vec{q}_2)^2}{[(\vec{q}_1-\vec{q}_2)^2+m_\pi^2]^2}+(\vec{q}_1-\vec{q}_2)\cdot(\vec{q}_3-\vec{q}_1)\frac{2m_\pi^2c_1-c_3(\vec{q}_1-\vec{q}_2)\cdot(\vec{q}_3-\vec{q}_1)}{[(\vec{q}_1-\vec{q}_2)^2+m_\pi^2]\,[(\vec{q}_3-\vec{q}_1)^2+m_\pi^2]}\Bigg]\,, \end{aligned} \tag{4.27}$$

where $\eta_1=\{1,6\}$ and $\eta_2=\{1,2\}$ for neutron and symmetric matter respectively. These integrals can be reduced to a one-dimensional integral by defining the following functions [261],

$$\begin{aligned} \int_{\vec{q}}\frac{(\vec{q}-\vec{p})_i(\vec{q}-\vec{p})_j}{(\vec{q}-\vec{p})^2+m_\pi^2}\theta(k_f-|\vec{q}|) &= \frac{m_\pi^3}{48\pi^2x}\left[\delta_{ij}G_S(x,u)+(3\hat{p}_i\hat{p}_j-\delta_{ij})G_T(x,u)\right]\,, \\ \int_{\vec{q}}\frac{(\vec{q}-\vec{p})_i}{(\vec{q}-\vec{p})^2+m_\pi^2}\theta(k_f-|\vec{q}|) &= \frac{m_\pi^2}{64\pi^2}\hat{p}_iG_V(x,u)\,, \end{aligned} \tag{4.28}$$

where $x=|\vec{p}|/m_\pi$ and $G_{S,V,T}$ are scalar integrals that can be obtained by contracting both

sides by δ_{ij} or factors of $\hat{p}$,

$$\begin{aligned}
G_S(x,u) &= \frac{4ux}{3}(2u^2-3) + 4x(\arctan(u+x)+\arctan(u-x)) \\
&\quad +(x^2-u^2-1)\log\frac{1+(u+x)^2}{1+(u-x)^2}\,, \\
G_V(x,u) &= \frac{1}{x^2}\Bigg(-4ux(u^2+x^2+1) \\
&\quad +(u^4-2u^2(x^2-1)+(x^2+1)^2)\log\frac{1+(u+x)^2}{1+(u-x)^2}\Bigg)\,, \\
G_T(x,u) &= \frac{ux}{6}(8u^2+3x^2) - \frac{u}{2x}(1+u^2)^2 \\
&\quad +\frac{1}{8}\left(\frac{(1+u^2)^3}{x^2} - x^4 + (1-3u^2)(1+u^2-x^2)\right)\log\frac{1+(u+x)^2}{1+(u-x)^2}\,. \qquad (4.29)
\end{aligned}$$

Using Eq. (4.28) to perform the $\vec{q}_2$ and $\vec{q}_3$ integrals in Eq. (4.27), we obtain

$$\begin{aligned}
\varepsilon_{c_{1,3}} &= \eta_1 \frac{g_A^2}{64\pi^4 F^4}\Bigg[\left(-c_3 + (c_1 - \frac{c_3}{2})m_\pi\partial_{m_\pi}\right)\int_0^u dx\, x\, m_\pi^6 G_S(x,u) \\
&\quad +\frac{1}{\eta_2}\frac{3m_\pi^9}{64k_f^3}\int_0^u dx\left(c_1 x^2\, G_V(x,u)^2 + \frac{8c_3}{9}\left(3G_S(x,u)^2 + 6G_T(x,u)^2\right)\right)\Bigg] \qquad (4.30)
\end{aligned}$$

where $\partial_{m_\pi} = \partial/\partial m_\pi$, which matches the result of Ref. [9] for symmetric matter up to the factor of 6, which is 1 in that reference.

The contributions from c_4, c_D, and c_E in symmetric matter can be obtained similarly and give

$$\begin{aligned}
\varepsilon_{c_E} &= -\frac{c_E}{F^4\Lambda_\chi}\frac{k_f^6}{12\pi^4}\,, \\
\varepsilon_{c_D} &= \frac{3g_A c_D m_\pi^6}{128\pi^4 F^4\Lambda_\chi}\int_0^u dx\, x\, G_S(x,u) \\
&= \frac{g_A c_D m_\pi^6}{1536\pi^4 F^4\Lambda_\chi}\left(32u^6 - 72u^4 + 12u^2 + 96u^3\arctan(2u) - (36u^2+3)\log(1+4u^2)\right)\,, \\
\varepsilon_{c_4} &= -\frac{3g_A^2 c_4 m_\pi^9}{256\pi^4 F^4 k_f^3}\int_0^u dx\,\left(G_S(x,u)^2 - G_T(x,u)^2\right)\,, \qquad (4.31)
\end{aligned}$$

in agreement with Ref. [9].

The resulting contributions in neutron matter and a comparison to Hartree-Fock estimates of the N^{2}LO 3NFs [9] are shown in Fig. 4.4, for $|D_2| < 1/(5f_\pi^4)$ and $|F_2| < 1/(5f_\pi^4)$

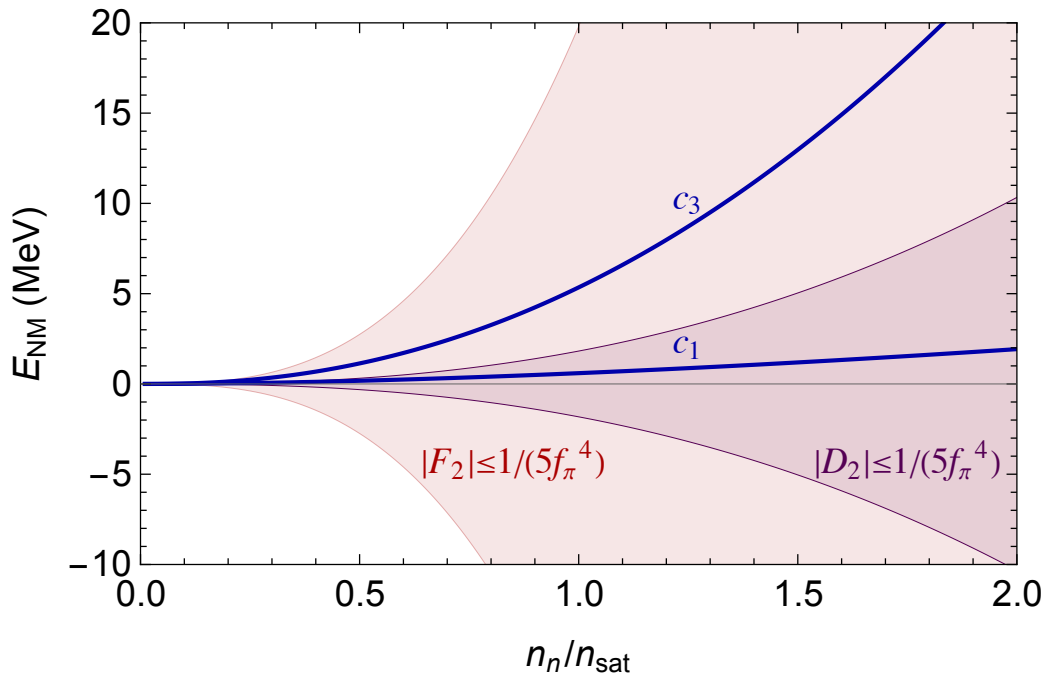

Figure 4.4: The figure shows D_2 and F_2 contributions to the energy per particle in neutron matter as a function of the density. The bands are obtained by setting $|D_2| < 1/(5f_\pi^4)$ and $|F_2| < 1/(5f_\pi^4)$. For reference, we show the contributions from the long-range Fujita-Miyazawa 3NF induced by the LECs c_1 and c_3, obtained by setting $c_1 = -0.81/\text{GeV}$ and $c_3 = -3.2/\text{GeV}$ [8].

while neglecting the ${}^3S_1$ couplings. In symmetric matter, the corresponding contributions are shown in Fig. 4.5 [5]. The results in these figures employ the DR result for the 3N potentials. If we instead use the regularization prescription of Refs. [249, 264], the long-range part of the potential tends to produce smaller contributions in dense matter. For example, in the case of the D_2, the contributions in neutron matter differ by a factor of $E_{\rm NM}^{(\Lambda)}/E_{\rm NM}^{(\rm DR)} = \{0.10, 0.29, 0.59, 0.78\}$ at $n = n_{\rm sat}$, for $\Lambda = \{0.3, 0.5, 1, 2\}$ GeV, where Λ is the cutoff in the scheme of Refs. [249, 264].

[5]The two figures use the values for $c_{1,3,4}$ and $c_{D,E}$ employed in Refs. [8, 9] for ease of comparison of the effects in dense matter. Note, however, that improved determinations of $c_{1,3,4}$ are available, see e.g. Refs. [169, 262, 263].

The prescription of Refs. [249, 264] removes the short-distance part of the D_2 and F_2 potentials, e.g. the pieces that are degenerate with c_E, and would most likely affect the value of c_E, when used in favor of e.g. DR. In addition, D_2 and F_2, as well as their contributions, depend on the regulator. This dependence is determined by requiring that $\pi NN \to \pi NN$ amplitude is regulator independent and cancels that of certain bubble diagrams (see Fig. 2 of Ref. [260]). In the context of 3NFs, the latter topologies are generated when the N^{3}LO 3NFs [265–267] are combined with iterations of the LO contact interaction, $\tilde{C}_0$. This implies that a fully consistent analysis will have to determine D_2 and F_2 together with the usual contact terms $c_{D,E}$ and include the conventional N^{3}LO 3NFs.

4.4 Implications

For Chiral EFT to provide a useful description of nuclei and neutron-rich matter, the results in Figs. 4.4 and 4.5 indicate that D_2 and F_2 will need to be determined rather accurately. In an *ab initio* approach, they would be deduced by fitting to the binding energies of light nuclei or from pion-nucleus scattering data. In the former approach, one would need to simultaneously determine c_D, c_E, D_2, and F_2 from light nuclei. Absent such constraints, in what follows, we focus on neutron matter and adopt a phenomenological approach to correlate D_2 and F_2 using empirical information about the nuclear symmetry energy $S_0 = 31.7 \pm 3.2$ MeV at saturation density [268].

Since the LECs associated with the 2NF and the long-range 3NF (c_1 and c_3) between neutrons are well constrained by scattering data, the associated interaction energies denoted by $E^{2N}_{\rm NM}$ and $E^{(c_1+c_3)}_{\rm NM}$, respectively, can be calculated accurately using quantum many-body methods [8, 269, 270]. Noting that the symmetry energy is the difference between the energy per particle of neutron and nuclear matter at saturation density, we define

$$\delta S_0 = S_0 - (\tilde{E}_{\rm NM}(n_{\rm sat}) - E_{\rm SM}(n_{\rm sat}))\,, \tag{4.32}$$

where

$$\tilde{E}_{\rm NM}(n_B) = E^{\rm kin}_{\rm NM}(n_B) + E^{2N}_{\rm NM}(n_B) + E^{(c_1+c_3)}_{\rm NM}(n_B)\,, \tag{4.33}$$

is the neutron matter energy when contributions from D_2 and F_2 are neglected and $E_{\rm SM}(n_{\rm sat}) \simeq -16$ MeV.

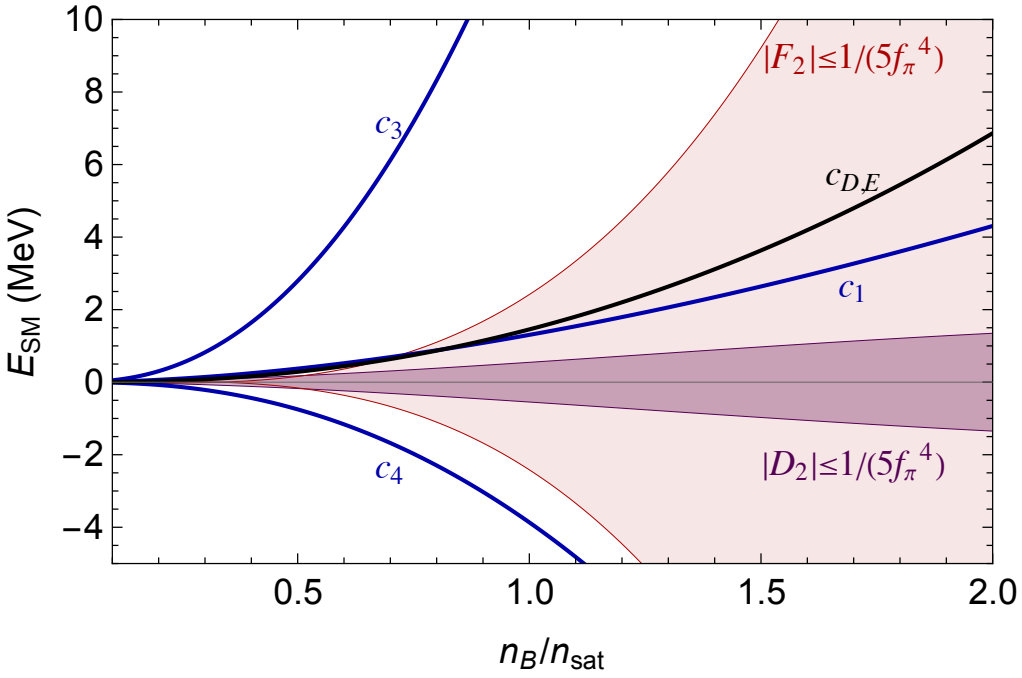

Figure 4.5: Same as Fig. 4.4, but for symmetric matter. For the single-nucleon LECs we use $c_1 = -0.76/\text{GeV}$, $c_3 = -4.78/\text{GeV}$, and $c_4 = 3.96/\text{GeV}$, while for the 2 and 3 nucleon terms we take $c_D = 2.08$, and $c_E = 0.23$ for $\Lambda_\chi = 700$ MeV [9].

We correlate D_2 and F_2 by requiring that $E^D_{\rm NM} + E^F_{\rm NM} = \delta S_0$ at $n_B = n_{\rm sat}$. Approximately, we find that $(100F_2 + 9D_2) \approx -(\delta S_0/\text{MeV})/f_\pi^4$.

Previously in the literature, the contributions from "old" operators at N2LO to the pressure at nuclear saturation density have been reported as $P(n_{sat}) = 3.1 \pm 0.5$ MeV/fm^3 [105] and $P(n_{sat}) = 2.2 \pm 0.4$ MeV/fm^3 [270].

In comparison, the estimated contribution to the pressure from the new three-nucleon forces derived in this work is given by

$$\delta P_{3NF} = \left[0.7\left(\frac{D_2}{D_2^{ref}})\right) + 8.8\left(\frac{F_2}{F_2^{ref}}\right)\right]\frac{\text{MeV}}{\text{fm}^3}\ , \tag{4.34}$$

where $D_2^{ref} = F_2^{ref} = 1/(5F_\pi^4)$ are the values estimated from RGEs.

In Fig. 4.6, we show δP, the net contribution from the D_2 and F_2 operators to the pressure of neutron matter. The bands are obtained by varying D_2 in the range $\pm 1/(5f_\pi^4)$ and F_2 is

determined by specifying δS_0. For $\delta S_0 \simeq \pm 2$ MeV, $\delta P \simeq \pm 1$ MeV/fm^3 at saturation density and the uncertainty associated with the parameter $L = 3P(n_{\rm sat})/n_{\rm sat}$ is $\simeq \pm 19$ MeV. The mild discrepancy between the EFT prediction for L and those deduced from the neutron-skin measurement of lead using the recent parity-violating electron scattering experiment (PREX) [271, 272] would be alleviated if this additional uncertainty is included.

The rapid change of δP in the density interval $n_{\rm sat} - 2n_{\rm sat}$ has implications for neutron stars and will be discussed in a separate paper [273]. The estimates of Fig. 4.6 call into question whether earlier estimates of the uncertainty associated with Chiral EFT predictions for the pressure of neutron star matter for $n_B \simeq n_{\rm sat} - 2n_{\rm sat}$ and its implied bounds on neutron star radii and maximum mass will need to be revised. Assessing the quantitative impact of these new effects will require calculations that include and determine these couplings in a consistent manner.

As previously noted in Ref. [274], the couplings of pions to two nucleons are also relevant to the analysis of pionic atoms and could explain the missing repulsion observed in phenomenological approaches [275]. The pion-nucleus optical potential used to describe pionic atoms also constrains D_2 and E_2. Using the analysis in [274] and several optical potentials extracted by different fitting procedures in Ref.[276], we find that -15 fm$^4 < D_2 + E_2 < -1$ fm^4. For values in this range, the s-wave interaction of the pion inside the nucleus is adequately repulsive to explain observed binding energies of pionic atoms.

4.5 Constraining new class of operators

The operators D_2, F_2, and E_2 haven't been constrained from experiments yet. In principle, these parameters could be determined through first-principles lattice QCD calculations. Such efforts have been undertaken by [240]. Experimentally, these operators could, in principle, be constrained in combination with c_D and c_E by analyzing few-body observables, including nucleon–deuteron scattering, the binding energies of light nuclei, and the beta decay of tritium. Another way for constraining these operators is through the study of dense matter properties near nuclear saturation density, nucleon–nucleus scattering, as well as astrophysical observables such as neutron star masses and radii, and gravitational wave signals from neutron star mergers.

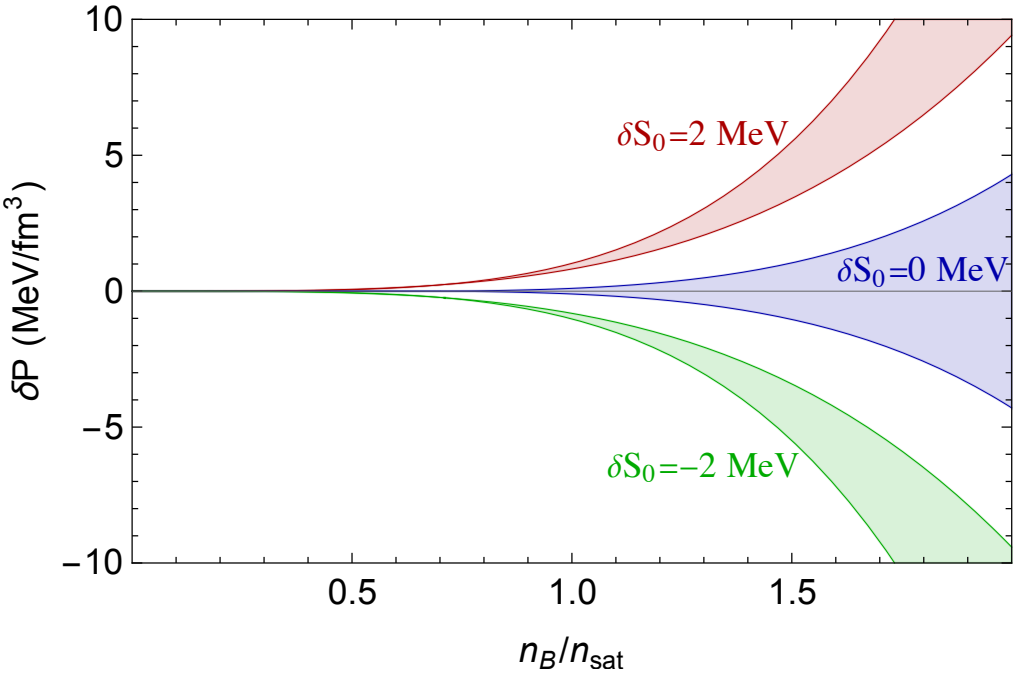

Figure 4.6: $D_2 + F_2$ contribution to the pressure of neutron matter.

We have made initial attempts to constrain these operators by combining Hartree–Fock estimates of the three-nucleon force with two-nucleon contributions, using dense matter properties near nuclear saturation density as input. The corresponding values are reported in the Table. V of Ref. [277], while the two-body part of the energy per baryon was taken from [278]. We expressed the dense matter properties in terms of the corresponding 3N operators, and used χ^2 fit to obtain the constraints. The results of the dependence D_2 operator on F_2 in neutron matter is shown of Fig. 4.7. Total contributions to the energy per particle in neutron matter as a function of the density is shown in Fig. 4.8.

The results presented here, while primarily illustrative, highlight the remarkable potential of this method for constraining previously unexplored operators. Two- and three-nucleon forces using different regulators, and Hartree-Fock estimates. Nevertheless, they suggest that dense matter properties could provide valuable constraints on the D_2 and F_2 operators. A more stringent determination of these couplings will require careful many-body calculations, and work in this direction is currently in progress.

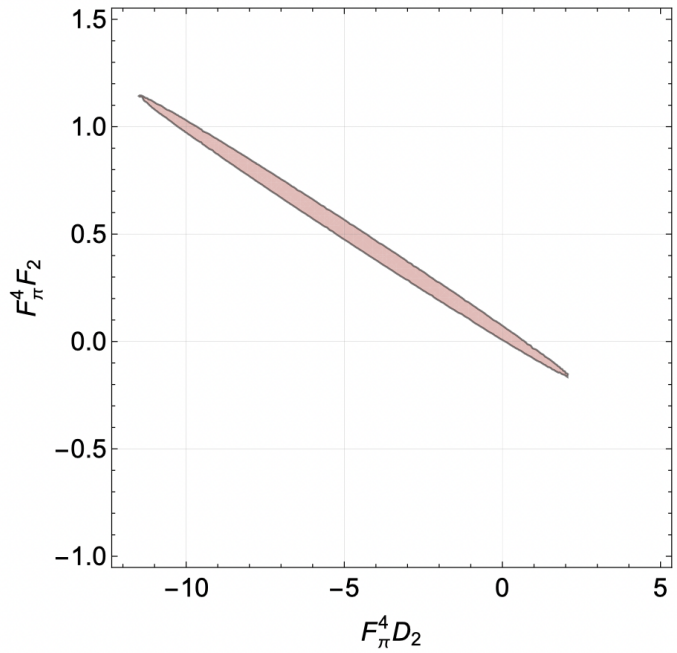

Figure 4.7: Dependence of the D_2 operator on F_2 in neutron matter. The results are obtained by minimizing the χ^2 function and properties of dense matter near saturation density.

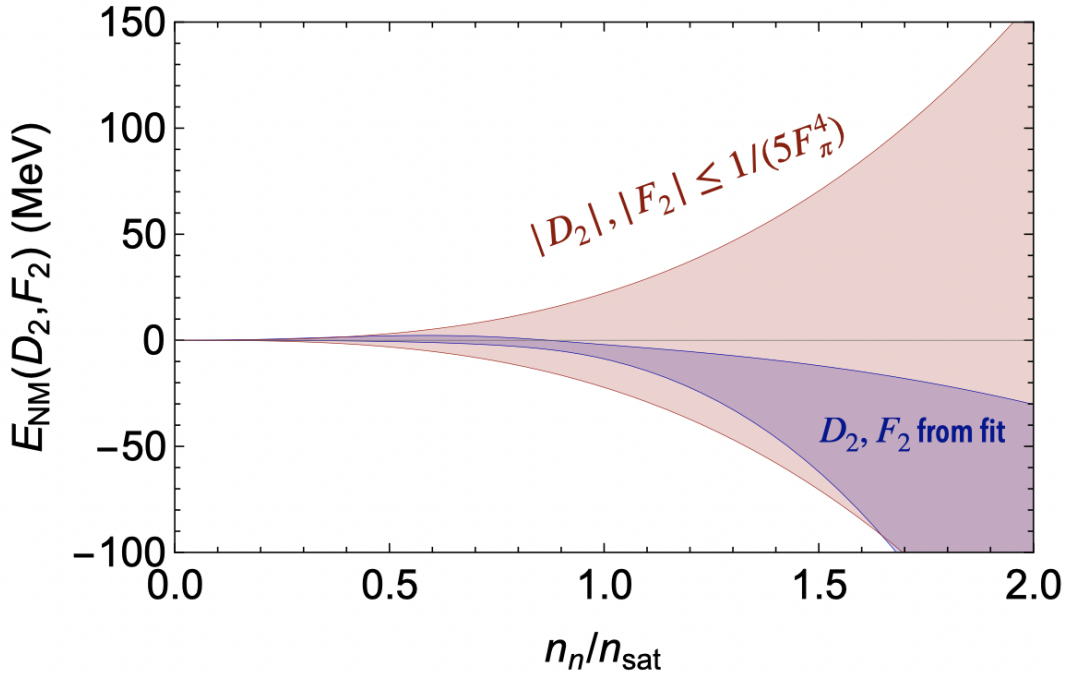

Figure 4.8: Total contributions to the energy per particle in neutron matter as a function of the density. The results are obtained by minimizing the χ^2 function and properties of dense matter near saturation density.

Chapter 5

CONCLUSIONS

This thesis has explored the use and scope of effective field theory methods in addressing two major phenomena in contemporary nuclear physics: precision studies of beta decay as a probe of new physics, and the theoretical understanding of strong interactions in nuclear systems. The work bridges phenomenology, formal developments, and experimental analysis, demonstrating how EFT provides a unifying framework across vastly different energy scales and physical systems. On the weak interaction side, beta decay has proven to be an invaluable laboratory for testing the Standard Model and constraining new physics through precision observables. Using the Standard Model Effective Field Theory, this thesis analyzed the dominant loop-level contributions to charged-current processes, particularly those arising from operators involving third-generation quarks. These effects, though not present at tree level, can influence beta decay observables through renormalization group evolution. In conjunction with improved radiative corrections derived from chiral perturbation theory, our theoretical efforts contribute to reducing uncertainties in the extraction of CKM matrix elements and support ongoing tests of first-row unitarity with unprecedented precision.

Experimentally, this work included analysis from the UCNτ collaboration, which has provided the most precise measurement to date of the neutron lifetime. This measurement is crucial for determining the axial coupling g_A, and thus V_{ud}, from neutron decay. It also plays a central role in resolving the neutron lifetime anomaly — a persistent discrepancy between beam and bottle methods. In addition to exploring possible systematic explanations, this thesis discussed speculative beyond-the-Standard-Model scenarios, such as dark decay modes and mirror neutron oscillations, providing a comprehensive treatment of current theoretical interpretations.

On the strong interaction side, the thesis presented work on the structure of nuclear forces within chiral EFT, identifying a previously neglected class of three-nucleon operators

required for proper renormalization. The contribution of the new 3NFs discussed in Chapter 4 is large enough to warrant their inclusion in all aspects of nuclear structure studies and calculations of the dense matter EOS. Using RG invariance to estimate the size of the associated LECs combined with a Hartree-Fock approximation, we find that at saturation density, they contribute a few MeV to the energy per particle of nuclear matter and their contribution to neutron matter can be as large as 10 MeV per particle–suggesting that earlier studies may have underestimated the EFT truncation errors. To obtain better estimates, D_2 and F_2 should be included in fits to experimental data, along with the currently considered LECs c_D and c_E and N^{3}LO 3NFs [116, 162, 165, 270, 279–282]. We hope our study motivates the inclusion of these new 3NFs in ab initio calculations of light nuclei and look forward to stringent constraints on the associated LECs.

D_2 and F_2 contributions are significant in neutron matter and highlight the role of using a consistent renormalization procedure in Chiral EFT. The expectation that Chiral EFT can provide a good description of neutron matter solely in terms of LECs extracted from nucleon-nucleon and pion-nucleon scattering data would require D_2 and F_2 to be significantly smaller than suggested by the RG analysis. We combined HF calculations of D_2 and F_2 contributions to the energy of neutron matter with earlier Chiral EFT predictions to correlate and restrict these LECs with empirical information about the nuclear symmetry energy. Even for values in this restricted range, our study highlights the need to revisit EFT predictions for the density dependence of the nuclear symmetry energy and its implications for the EOS of neutron-rich matter and neutron stars, neutron skins of nuclei, and the interpretation of the data from pionic atoms.

In summary, this thesis demonstrates that the EFT approach is not only a powerful computational tool but also a conceptual framework for organizing physical insight. By applying EFT across weak and strong interaction sectors, we have contributed to sharpening the precision frontier of Standard Model tests and to deepening the theoretical understanding of nuclear forces. The continuing interplay between theory and experiment will be essential as we seek to probe new physics and further unravel the structure of matter.

Appendices

Appendix 1

NUMERICAL RESULTS FOR THE RG EVOLUTION

Table A.1: Results for $U_{ik}(\mu_W, \Lambda)$, which describes the ratio of $C_{\beta i}(\mu_W)$ at low electroweak scale $\mu_W = 0.246$ TeV to $C_{xk}(\Lambda)$ at high scale $\Lambda = 5$ TeV as defined in (3.20). In the table below, the rows correspond to the index k while the columns correspond to the index i. We report here only the entries with $|U_{ik}(\mu_W, \Lambda)| > 10^{-3}$.

C_x	$C^{(3)}_{Hl\ 11}$	$C^{(3)}_{Hl\ 22}$	$C^{(3)}_{Hq\ 11}$	$C^{(3)}_{ll\ 1221}$	$C^{(3)}_{ll\ 2112}$	$C^{(3)}_{lq\ 1111}$
$C^{(3)}_{qq\ 1111}$	0	0	−0.0261	0	0	−0.0262
$C^{(3)}_{qq\ 1122}$	0	0	−0.0153	0	0	−0.0154
$C^{(3)}_{qq\ 1133}$	−0.0010	−0.0010	0.0819	0	0	−0.0154
$C^{(3)}_{qq\ 1221}$	0	0	0.0025	0	0	0.0025
$C^{(3)}_{qq\ 1331}$	0	0	−0.0113	0	0	0.0025
$C^{(3)}_{qq\ 2112}$	0	0	0.0025	0	0	0.0025
$C^{(3)}_{qq\ 2211}$	0	0	−0.0153	0	0	−0.0154
$C^{(3)}_{qq\ 2233}$	−0.0010	−0.0010	−0.0010	0	0	0
$C^{(3)}_{qq\ 3113}$	0	0	−0.0113	0	0	0.0025
$C^{(3)}_{qq\ 3311}$	−0.0010	−0.0010	0.0818	0	0	−0.016
$C^{(3)}_{qq\ 3322}$	−0.0010	−0.0010	−0.0010	0	0	0

$C^{(3)}_{qq\ 3333}$	-0.0021	-0.0021	-0.0021	0	0	0
$C^{(1)}_{qq\ 1111}$	-0.0158	0	-0.0037	0	0	-0.0037
$C^{(1)}_{qq\ 1133}$	0	0	-0.0020	0	0	0
$C^{(1)}_{qq\ 1221}$	0	0	-0.0020	0	0	-0.0020
$C^{(1)}_{qq\ 1331}$	0	0	0.0110	0	0	-0.0020
$C^{(1)}_{qq\ 2112}$	0	0	-0.0022	0	0	-0.0021
$C^{(1)}_{qq\ 3113}$	0	0	0.012	0	0	-0.0021
$C^{(1)}_{qq\ 3311}$	0	0	-0.001	0	0	0
$C^{(3)}_{lq\ 1111}$	-0.0158	0	-0.0051	-0.0156	-0.0156	1.0311
$C^{(3)}_{lq\ 1122}$	-0.0158	0	0	-0.0160	-0.0160	-0.0157
$C^{(3)}_{lq\ 1133}$	0.0834	0	0	-0.0156	-0.0156	-0.0157
$C^{(3)}_{lq\ 2211}$	0	-0.0158	-0.0051	-0.0156	-0.0156	-0.0051
$C^{(3)}_{lq\ 2222}$	0	-0.0158	0	-0.0156	-0.0156	0
$C^{(3)}_{lq\ 2233}$	0	0.0834	0	-0.0156	-0.0156	0
$C^{(3)}_{lq\ 3311}$	0	0	-0.0056	0	0	-0.0051
$C_{ll\ 1111}$	-0.0051	0	0	-0.0051	-0.0051	-0.0052
$C_{ll\ 1122}$	0	0	0	-0.049	0	0
$C_{ll\ 1221}$	-0.0026	-0.0026	0	1.007	-0.0052	-0.0026
$C_{ll\ 1331}$	-0.0026	0	0	-0.0027	-0.0026	-0.0027
$C_{ll\ 2112}$	-0.0026	-0.0026	0	-0.0052	1.007	-0.0026

$C_{\substack{ll \\ 2211}}$	0	0	0	0	-0.049	0
$C_{\substack{ll \\ 2222}}$	0	-0.0054	0	-0.0051	-0.0051	0
$C_{\substack{ll \\ 2332}}$	0	-0.0027	0	-0.0026	-0.0026	0
$C_{\substack{ll \\ 3113}}$	-0.0026	0	0	-0.0026	-0.0026	-0.0027
$C_{\substack{ll \\ 3223}}$	0	-0.0027	0	-0.0026	-0.0026	0
$C^{(3)}_{\substack{Hq \\ 11}}$	-0.0143	-0.0143	0.9257	0	0	-0.0026
$C^{(3)}_{\substack{Hq \\ 22}}$	-0.0143	-0.0143	-0.0141	0	0	0
$C^{(3)}_{\substack{Hq \\ 33}}$	-0.0142	-0.0142	-0.0140	0	0	0
$C^{(3)}_{\substack{Hl \\ 11}}$	0.957	-0.005	-0.005	-0.003	-0.003	-0.003
$C^{(3)}_{\substack{Hl \\ 22}}$	-0.0053	0.957	-0.0053	-0.003	-0.003	0
$C^{(3)}_{\substack{Hl \\ 33}}$	-0.0048	-0.0048	-0.0048	0	0	0
$C_{H\Box}$	-0.0013	-0.0013	-0.0013	0	0	0

Appendix 2

ONE LOOP DIAGRAMS CONTRIBUTING TO THE TWO-BODY POTENTIAL TO SUPERALLOWED BETA DECAY

B.1 Topology 1: π (with explicit γ

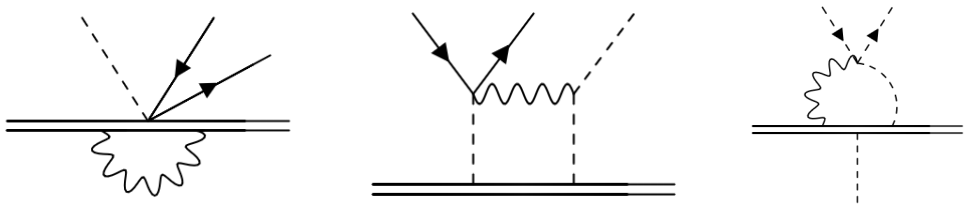

Figure B.1

B.2 Topology 2: γN

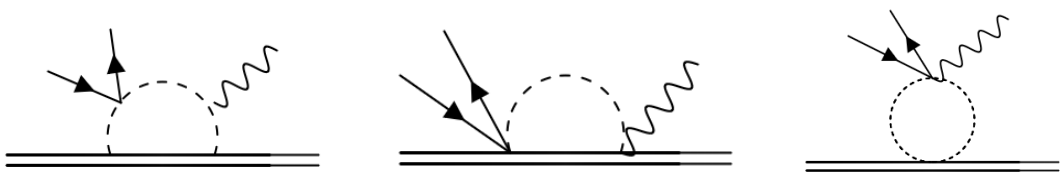

Figure B.2

B.3 Topology 3: NN with explicit γ

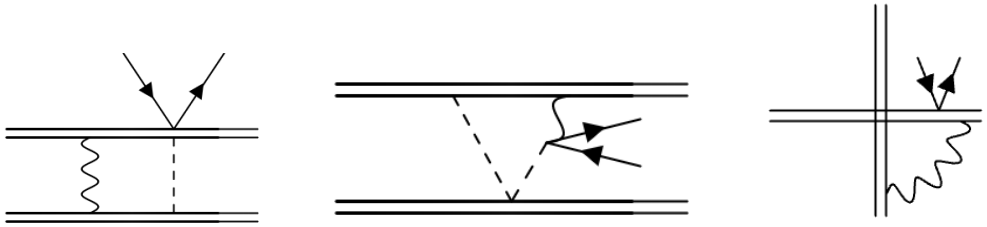

Figure B.3

B.4 Topology 4: Z_π with pion mass splitting contributions

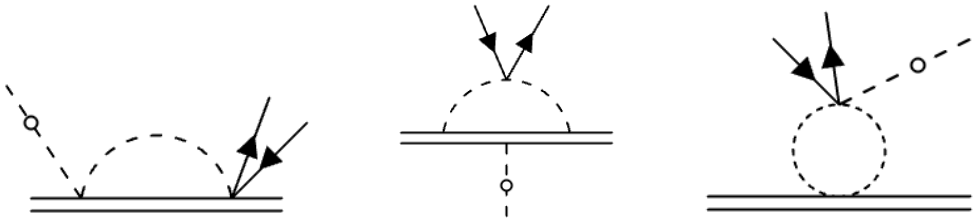

Figure B.4

B.5 Topology 5: NN (with explicit Z_π)

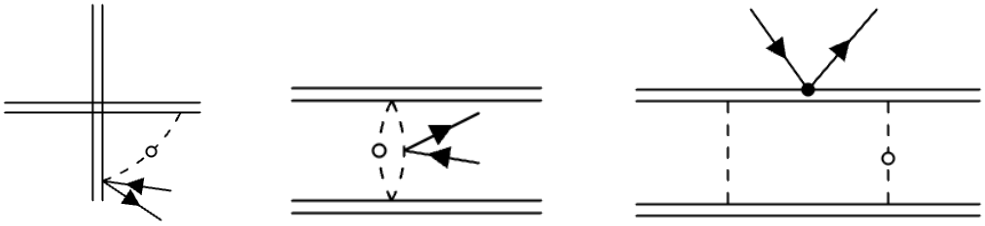

Figure B.5

Appendix 3

QFT VERSION OF THE POTENTIAL

The potential can be interpreted as the result of matching the usual χPT Lagrangian, involving nucleons and pions, onto a χEFT Lagrangian in terms of just the nucleon fields. This second EFT can only describe interactions without pions and takes the form $\mathcal{L}_{\chi EFT} = \bar{N}(iv\cdot D + \vec{\nabla}^2/2m_N)N - \hat{V}$, where the potential should capture the effects of pion-exchanges and contact interactions. In this language, the potential can be written as,

$$\begin{aligned}\int_{\vec{x}} \hat{V}(x) &= \hat{a}_2 \int_{\vec{x}_1,\vec{x}_2} \bar{N}_{\beta_1}(x_1)\bar{N}_{\beta_2}(x_2)V^{\beta_1\beta_2}_{\alpha_1\alpha_2}(x_1,x_2)N_{\alpha_2}(x_2)N_{\alpha_1}(x_1) + \dots \\ &\quad + \hat{a}_n \int_{\vec{x}_1\dots\vec{x}_n} \bar{N}_{\beta_1}(x_1)\dots\bar{N}_{\beta_n}(x_n)V^{\beta_1\dots\beta_n}_{\alpha_1\dots\alpha_n}(x_1,\dots x_n)N_{\alpha_n}(x_n)\dots N_{\alpha_1}(x_1) \end{aligned} \tag{C.1}$$

where α, β denote (iso)spin indices, the $\hat{a}_m$ terms capture m-body potentials, and the dots stand for 3 to $n-1$ body interactions. All of the appearing nucleon fields should be evaluated at equal times, i.e. $v\cdot x_i = v\cdot X$ and the $\hat{a}_i$ prefactors are convention dependent, Fetter & Walecka use $\hat{a}_2 = 1/2$.

The above should somehow lead to the usual QM version of the Schrödinger equation, which, for an n-body wavefunction, takes the form

$$\begin{aligned} E\psi^{\alpha_1\dots\alpha_n}(x_1\dots x_n) &= \Bigg[\sum_i \delta\vec{\nabla}_i^2/2m_N + a_2\sum_{i\neq j}\delta_{ij}V^{\alpha_i\alpha_j}_{\beta_i\beta_j}(x_i,x_j) + \dots \\ &\quad + a_n \sum_{i_1\neq i_2\dots\neq i_n} V^{\alpha_{i_1}\dots\alpha_{i_n}}_{\beta_{i_1}\dots\beta_{i_n}}(x_{i_1},\dots x_{i_n})\Bigg]\psi^{\beta_1\dots\beta_n}(x_1\dots x_n)\,, \end{aligned} \tag{C.2}$$

where x_i denotes the position of nucleon i, the prefactors, a_i, are again convention dependent and the δ's should set all the β's that are not acted on by the potentials equal to the α's, $\delta_{i_1\dots i_n} = \prod_{m\neq\{i_1,\dots i_n\}}\delta^{\alpha_m}_{\beta_m}$.

To see how the above QM and QFT approaches are related, we can look at what kind of Schrödinger equation is implied by Eq. (C.1) by letting it act on the QFT version of a

n-body wavefunction,

$$\hat{\psi}(x_1 \dots x_n) = f^{\alpha_1 \dots \alpha_n}(x_1 \dots x_n) \bar{N}_{\alpha_1}(x_1) \dots \bar{N}_{\alpha_n}(x_n)|0\rangle \,. \tag{C.3}$$

When we act with the potential on this wavefunction, we'll get all possible contractions of the N fields in the potential with the $\bar{N}$'s in the wavefunction, each of which will give a δ function through $\{\bar{N}_\alpha(x), N_\beta(y)\} = (2\pi)^3 \delta^3(\vec{x} - \vec{y}) \delta^{\alpha\beta}$. The $\bar{N}$ fields that are eliminated by these contractions are then replaced by the $\bar{N}$'s coming from the potential. For example, the two-body part of $\hat{V}$ leads to $n(n-1)$ possible contractions,

$$\hat{V}_{2b}\hat{\psi}(x_1 \dots x_n) = \sum_{i \neq j} V^{\beta_i \beta_j}_{\alpha_i \alpha_j}(x_i, x_j) f^{\alpha_1 \dots \alpha_n}(x_1 \dots x_n)$$
$$\times \bar{N}_{\alpha_1}(x_1) \dots \bar{N}_{\alpha_{i-1}}(x_{i-1}) \bar{N}_{\beta_i}(x_i) \bar{N}_{\alpha_{i+1}}(x_{i+1}) \dots \bar{N}_{\alpha_{j-1}}(x_{j-1}) \bar{N}_{\beta_j}(x_j) \bar{N}_{\alpha_{j+1}}(x_{j+1}) \dots \bar{N}_{\alpha_n}(x_n)|0\rangle \,.$$

We can work out all the contractions in the QFT version of the Schrödinger equation, $(E - \hat{H})\hat{\psi} = 0$, in the same way. Using $\hat{H} = \int_{\vec{x}} \left[\bar{N} \vec{\nabla}^2 / 2 m_N N + \hat{V}(x) \right]$ and multiplying the resulting equation by $\int_{\vec{y}_1 \dots \vec{y}_n} \langle 0 | N_{\alpha_n}(y_n) \dots N_{\alpha_1}(y_1)$, we get

$$\begin{aligned} E f^{\alpha_1 \dots \alpha_n}(x_1 \dots x_n) \;\; = \;\; & \Bigg[\sum_i \delta \vec{\nabla}_i^2 / 2 m_N + \hat{a}_2 \sum_{i \neq j} \delta_{ij} V^{\alpha_i \alpha_j}_{\beta_i \beta_j}(x_i, x_j) + \dots \\ & + \hat{a}_n \sum_{i_1 \neq i_2 \dots \neq i_n} V^{\alpha_{i_n} \dots \alpha_{i_n}}_{\beta_{i_1} \dots \beta_{i_n}}(x_{i_1}, \dots x_{i_n}) \Bigg] f^{\beta_1 \dots \beta_n}(x_1 \dots x_n) \,. \end{aligned} \tag{C.4}$$

This implies that solving the QM version in Eq. (C.2) is equivalent to solving the QFT version in Eq. (C.4) as long as we set $\hat{a}_i = a_i$.

Appendix 4

SPECTRAL FUNCTION REGULATOR

The D_2 and F_2 operators induce three-nucleon potentials, which in momentum space take the form

$$V_{ijk}^{i'j'k'}(\vec{q}_1,\vec{q}_2,\vec{q}_3) = \frac{9g_A^2 D_2 m_\pi^3}{128\pi f_\pi^4}\kappa_{ij}^{i'j'}\delta_{kk'}\,\mathcal{I}\left(\frac{\vec{q}_3^{\,2}}{4m_\pi^2}\right)\,, \tag{D.1}$$

where $\kappa_{ij}^{i'j'} = (d_2^S\delta_{ii'}\delta_{jj'} + d_2^T\vec{\sigma}_{i'i}\cdot\vec{\sigma}_{j'j})/(d_2^S - 3d_2^T)$, and

$$\mathcal{I}(b) = \frac{2}{3}\left(1+\left(\frac{1}{2\sqrt{b}}+\sqrt{b}\right)\tan^{-1}(\sqrt{b})\right)\,. \tag{D.2}$$

For D_2, and

$$\begin{aligned} V_{ijk}^{i'j'k'}(\vec{q}_1,\vec{q}_2,\vec{q}_3) &= -\frac{15g_A^2 m_\pi^3}{16\pi f_\pi^4}\delta_{kk'}\mathcal{J}\left(\frac{\vec{q}_3^{\,2}}{4m_\pi^2}\right) \\ &\times \left(f_2^S\delta_{ii'}\delta_{jj'} + f_2^T\vec{\sigma}_{i'i}\cdot\vec{\sigma}_{j'j}\right), \end{aligned} \tag{D.3}$$

where

$$\mathcal{J}(b) = \frac{3}{5}\left((1+2b)\mathcal{I}(b)+\frac{2}{3}\right)\,, \tag{D.4}$$

for F_2, where $q_i = p_i' - p_i$ is the exchanged momentum of nucleon i, and $\sum q_i = 0$. We neglect the contribution from the E_2 operator because it is proportional to the kinetic energy of the nucleons.

The non-polynomial part of the loop functions can be written as

$$\mathcal{I}_{non-poly} = \frac{2}{3M_\pi}(2M_\pi^2+q^2)A(q)\,, \qquad A(q) = \frac{1}{2q}\arctan\frac{q}{2M_\pi}\,, \tag{D.5}$$

for the D_2 operator, while for F_2

$$\mathcal{J}_{non-poly}(q) = \frac{2}{10M_\pi^3}(2M_\pi^2+q^2)^2A(q)\,. \tag{D.6}$$

The long-range part of the resulting potentials can be obtained by spectral-function regularization as described in [249], via

$$X_{long-range}(q) = \frac{2}{\pi}\int_{2M_\pi}^{\infty}\frac{d\mu}{\mu^3}\rho_X(\mu)\left(\frac{q^4}{\mu^2+q^2}+C_1(\mu)+C_2(\mu)q^2\right)e^{-\frac{\mu^2+q^2}{2\Lambda^2}}\,, \tag{D.7}$$

where $X = \mathcal{I}, \mathcal{J}$ and Λ is a cutoff of the order of the breakdown scale and the spectral functions are given by

$$\rho_{\mathcal{I}}(\mu) = \frac{2}{3M_\pi}(2M_\pi^2 - \mu^2)\frac{\pi}{4\mu} \ , \qquad \rho_{\mathcal{J}}(\mu) = \frac{2}{10M_\pi^3}(2M_\pi^2 - \mu^2)^2\frac{\pi}{4\mu} \ , \tag{D.8}$$

and C_1 and C_2 are

$$C_1(\mu) = \frac{2\Lambda\mu^2(2\Lambda^4 - 4\Lambda^2\mu^2 - \mu^4) + \sqrt{2\pi}\mu^5 e^{\frac{\mu^2}{2\Lambda^2}}(5\Lambda^2 + \mu^2)\mathrm{erfc}(\frac{\mu}{\sqrt{2}\Lambda})}{4\Lambda^5} \tag{D.9}$$

$$C_2(\mu) = -\frac{2\Lambda(6\Lambda^6 - 2\Lambda^2\mu^4 - \mu^6) + \sqrt{2\pi}\mu^5 e^{\frac{\mu^2}{2\Lambda^2}}(3\Lambda^2 + \mu^2)\mathrm{erfc}(\frac{\mu}{\sqrt{2}\Lambda})}{12\Lambda^7} \tag{D.10}$$

where $\mathrm{erfc}(x)$ is the complementary error function

$$\mathrm{erfc}(x) = \frac{2}{\sqrt{\pi}}\int_x^\infty dt e^{-t^2} \ . \tag{D.11}$$

We used $X_{\mathrm{long-range}}(q)$ in place of our loop functions, $\mathcal{I}, \mathcal{J}$, when computing the contribution to the energy per particle. The results are shown in Fig. D.1 and Fig. D.2, for several values of the cutoff Λ. The difference between our result and that obtained by using Epelbaum's regulator is about a factor of two for $n = n_{\mathrm{sat}}$ and $\Lambda = 500$ MeV.

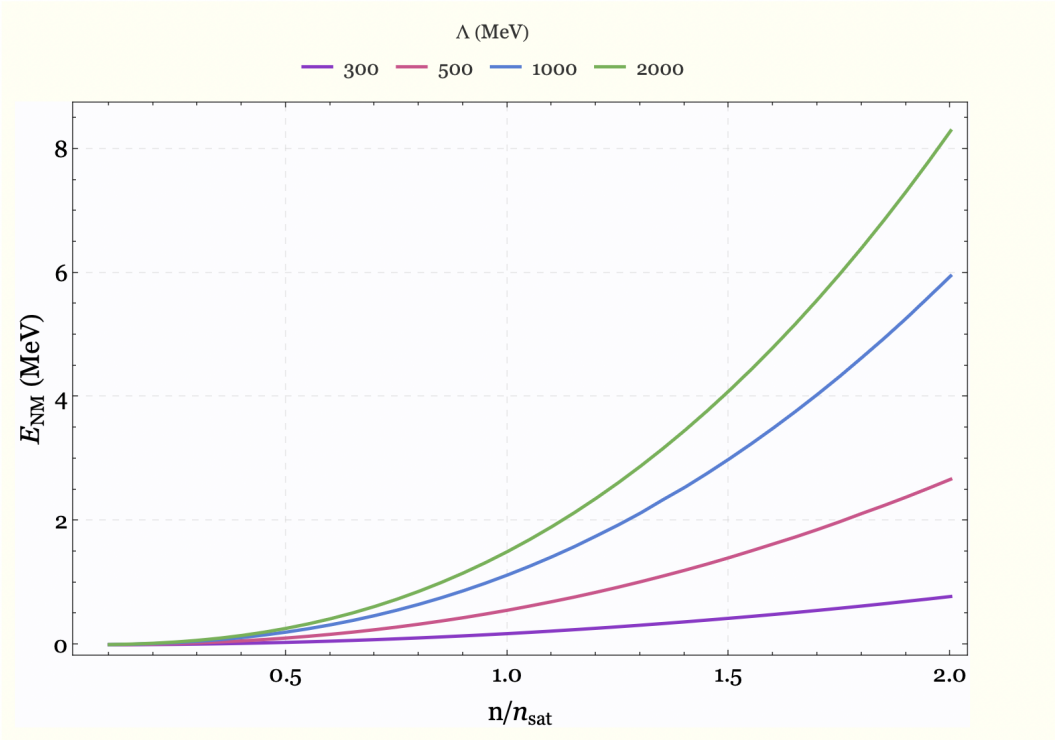

Figure D.1: The contribution to the energy in neutron matter, when using the regulator suggested by Epelbaum for D_2 operator.

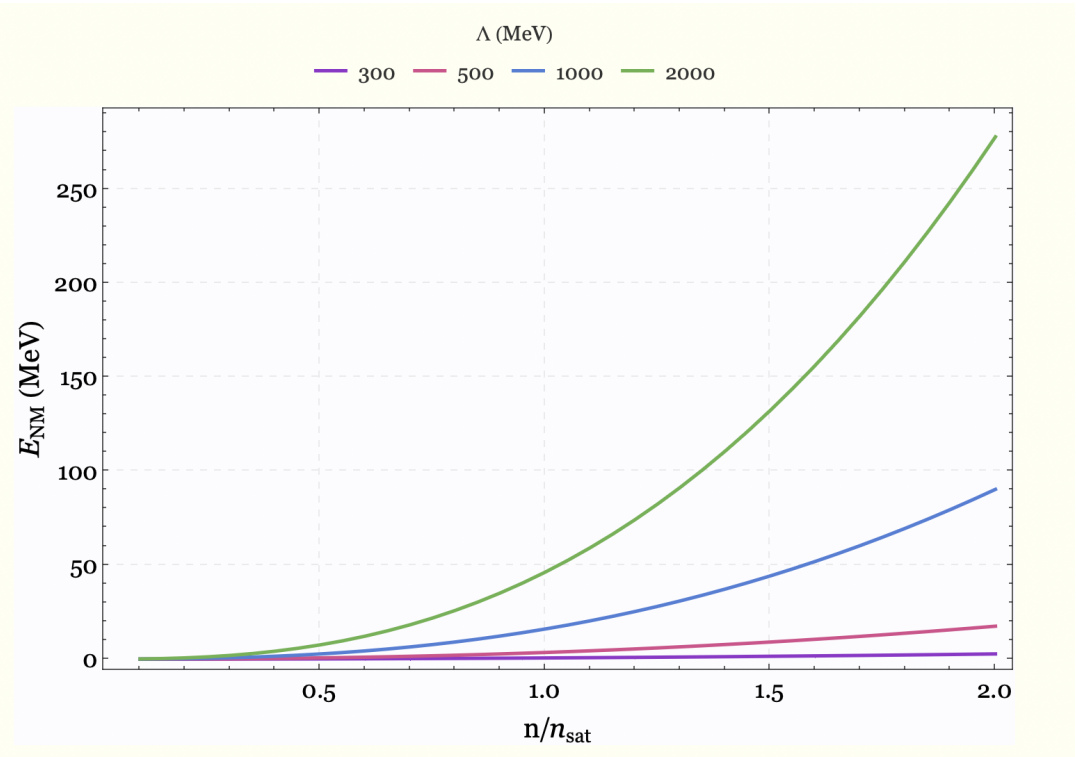

Figure D.2: The contribution to the energy in neutron matter, when using the regulator suggested by Epelbaum for F_2 operator.

BIBLIOGRAPHY

[1] William J. Marciano. Precise determination of |V(us)| from lattice calculations of pseudoscalar decay constants. *Phys. Rev. Lett.*, 93:231803, 2004.

[2] Y. Aoki et al. FLAG Review 2021. *Eur. Phys. J. C*, 82(10):869, 2022.

[3] Mikhail Gorchtein. γW Box Inside Out: Nuclear Polarizabilities Distort the Beta Decay Spectrum. *Phys. Rev. Lett.*, 123(4):042503, 2019.

[4] Particle Data Group, R L Workman, V D Burkert, V Crede, E Klempt, U Thoma, L Tiator, K Agashe, G Aielli, B C Allanach, C Amsler, M Antonelli, E C Aschenauer, D M Asner, H Baer, Sw Banerjee, R M Barnett, L Baudis, C W Bauer, J J Beatty, V I Belousov, J Beringer, A Bettini, O Biebel, K M Black, E Blucher, R Bonventre, V V Bryzgalov, O Buchmuller, M A Bychkov, R N Cahn, M Carena, A Ceccucci, A Cerri, R Sekhar Chivukula, G Cowan, K Cranmer, O Cremonesi, G D'Ambrosio, T Damour, D de Florian, A de Gouvêa, T DeGrand, P de Jong, S Demers, B A Dobrescu, M D'Onofrio, M Doser, H K Dreiner, P Eerola, U Egede, S Eidelman, A X El-Khadra, J Ellis, S C Eno, J Erler, V V Ezhela, W Fetscher, B D Fields, A Freitas, H Gallagher, Y Gershtein, T Gherghetta, M C Gonzalez-Garcia, M Goodman, C Grab, A V Gritsan, C Grojean, D E Groom, M Grünewald, A Gurtu, T Gutsche, H E Haber, Matthieu Hamel, C Hanhart, S Hashimoto, Y Hayato, A Hebecker, S Heinemeyer, J J Hernández-Rey, K Hikasa, J Hisano, A Höcker, J Holder, L Hsu, J Huston, T Hyodo, Al Ianni, M Kado, M Karliner, U F Katz, M Kenzie, V A Khoze, S R Klein, F Krauss, M Kreps, P Križan, B Krusche, Y Kwon, O Lahav, J Laiho, L P Lellouch, J Lesgourgues, A R Liddle, Z Ligeti, C-J Lin, C Lippmann, T M Liss, L Littenberg, C Lourenço, K S Lugovsky, S B Lugovsky, A Lusiani, Y Makida, F Maltoni, T Mannel, A V Manohar, W J Marciano, A Masoni, J Matthews, U-G Meißner, I-A Melzer-Pellmann, M Mikhasenko, D J Miller, D Milstead, R E Mitchell, K Mönig, P Molaro, F Moort-

gat, M Moskovic, K Nakamura, M Narain, P Nason, S Navas, A Nelles, M Neubert, P Nevski, Y Nir, K A Olive, C Patrignani, J A Peacock, V A Petrov, E Pianori, A Pich, A Piepke, F Pietropaolo, A Pomarol, S Pordes, S Profumo, A Quadt, K Rabbertz, J Rademacker, G Raffelt, M Ramsey-Musolf, B N Ratcliff, P Richardson, A Ringwald, D J Robinson, S Roesler, S Rolli, A Romaniouk, L J Rosenberg, J L Rosner, G Rybka, M G Ryskin, R A Ryutin, Y Sakai, S Sarkar, F Sauli, O Schneider, S Schönert, K Scholberg, A J Schwartz, J Schwiening, D Scott, F Sefkow, U Seljak, V Sharma, S R Sharpe, V Shiltsev, G Signorelli, M Silari, F Simon, T Sjöstrand, P Skands, T Skwarnicki, G F Smoot, A Soffer, M S Sozzi, S Spanier, C Spiering, A Stahl, S L Stone, Y Sumino, M J Syphers, F Takahashi, M Tanabashi, J Tanaka, M Taševský, K Terao, K Terashi, J Terning, R S Thorne, M Titov, N P Tkachenko, D R Tovey, K Trabelsi, P Urquijo, G Valencia, R Van de Water, N Varelas, G Venanzoni, L Verde, I Vivarelli, P Vogel, W Vogelsang, V Vorobyev, S P Wakely, W Walkowiak, C W Walter, D Wands, D H Weinberg, E J Weinberg, N Wermes, M White, L R Wiencke, S Willocq, C G Wohl, C L Woody, W-M Yao, M Yokoyama, R Yoshida, G Zanderighi, G P Zeller, O V Zenin, R-Y Zhu, Shi-Lin Zhu, F Zimmermann, and P A Zyla. Review of particle physics. *Progress of Theoretical and Experimental Physics*, 2022(8):083C01, 08 2022.

[5] Vincenzo Cirigliano, Andreas Crivellin, Martin Hoferichter, and Matthew Moulson. Scrutinizing CKM unitarity with a new measurement of the $K_{\mu 3}/K_{\mu 2}$ branching fraction. *arXiv*, August 2022.

[6] D. R. Entem, R. Machleidt, and Y. Nosyk. High-quality two-nucleon potentials up to fifth order of the chiral expansion. *Phys. Rev. C*, 96(2):024004, 2017.

[7] R. W. Pattie, N. B. Callahan, C. Cude-Woods, E. R. Adamek, L. J. Broussard, S. M. Clayton, S. A. Currie, E. B. Dees, X. Ding, E. M. Engel, D. E. Fellers, W. Fox, P. Geltenbort, K. P. Hickerson, M. A. Hoffbauer, A. T. Holley, A. Komives, C.-Y. Liu, S. W. T. MacDonald, M. Makela, C. L. Morris, J. D. Ortiz, J. Ramsey, D. J. Salvat, A. Saunders, S. J. Seestrom, E. I. Sharapov, S. K. Sjue, Z. Tang, J. Vanderwerp, B. Vogelaar, P. L. Walstrom, Z. Wang, W. Wei, H. L. Weaver, J. W. Wexler, T. L.

Womack, A. R. Young, and B. A. Zeck. Measurement of the neutron lifetime using a magneto-gravitational trap and in situ detection. *Science*, 360(6389):627–632, 2018.

[8] K. Hebeler and A. Schwenk. Chiral three-nucleon forces and neutron matter. *Phys. Rev. C*, 82:014314, 2010.

[9] S. K. Bogner, A. Schwenk, R. J. Furnstahl, and A. Nogga. Is nuclear matter perturbative with low-momentum interactions? *Nucl. Phys. A*, 763:59–79, 2005.

[10] Howard Georgi. Effective field theory. *Ann. Rev. Nucl. Part. Sci.*, 43:209–252, 1993.

[11] Antonio Pich. Effective field theory: Course. In *Les Houches Summer School in Theoretical Physics, Session 68: Probing the Standard Model of Particle Interactions*, pages 949–1049, 6 1998.

[12] Steven Weinberg. Phenomenological lagrangians. *Physica A*, 96:327, 1979.

[13] David B. Kaplan. Effective field theories. *nucl-th/9506035*, 1995.

[14] Particle Data Group. Review of particle physics. *Prog. Theor. Exp. Phys.*, 2022(8):083C01, 2022.

[15] Steven Weinberg. *The Quantum Theory of Fields, Volume 3: Supersymmetry*. Cambridge University Press, 2005.

[16] W. Buchmuller and D. Wyler. Effective Lagrangian Analysis of New Interactions and Flavor Conservation. *Nucl. Phys. B*, 268:621–653, 1986.

[17] B. Grzadkowski, M. Iskrzynski, M. Misiak, and J. Rosiek. Dimension-Six Terms in the Standard Model Lagrangian. *JHEP*, 10:085, 2010.

[18] Maria Dawid, Vincenzo Cirigliano, and Wouter Dekens. One-loop analysis of β decays in SMEFT. *JHEP*, 08:175, 2024.

[19] F. M. Gonzalez et al. Improved neutron lifetime measurement with UCNτ. *Phys. Rev. Lett.*, 127(16):162501, 2021.

[20] David B. Kaplan, Martin J. Savage, and Mark B. Wise. Nucleon - nucleon scattering from effective field theory. *Nucl. Phys. B*, 478:629–659, 1996.

[21] Vincenzo Cirigliano, Maria Dawid, Wouter Dekens, and Sanjay Reddy. New Class of Three-Nucleon Forces and Their Implications. *Phys. Rev. Lett.*, 135(2):022501, 2025.

[22] Enrico Fermi. Tentativo di una teoria dell'emissione dei raggi "beta". *La Ricerca Scientifica*, 4:491–495, 1933.

[23] T. D. Lee and C. N. Yang. Question of parity conservation in weak interactions. *Phys. Rev.*, 104:254–258, Oct 1956.

[24] Tanmoy Bhattacharya, Vincenzo Cirigliano, Saul D. Cohen, Alberto Filipuzzi, Martin Gonzalez-Alonso, Michael L. Graesser, Rajan Gupta, and Huey-Wen Lin. Probing Novel Scalar and Tensor Interactions from (Ultra)Cold Neutrons to the LHC. *Phys. Rev. D*, 85:054512, 2012.

[25] Vincenzo Cirigliano, Martin Gonzalez-Alonso, and Michael L. Graesser. Non-standard Charged Current Interactions: beta decays versus the LHC. *JHEP*, 02:046, 2013.

[26] Martin González-Alonso, Oscar Naviliat-Cuncic, and Nathal Severijns. New physics searches in nuclear and neutron β decay. *Prog. Part. Nucl. Phys.*, 104:165–223, 2019.

[27] William J. Marciano and Alberto Sirlin. Improved calculation of electroweak radiative corrections and the value of V(ud). *Phys. Rev. Lett.*, 96:032002, 2006.

[28] Mikhail Gorchtein and Chien-Yeah Seng. The Standard Model Theory of Neutron Beta Decay. *Universe*, 9(9):422, 2023.

[29] J. D. Jackson, S. B. Treiman, and H. W. Wyld. Possible tests of time reversal invariance in beta decay. *Phys. Rev.*, 106:517–521, May 1957.

[30] A. Sirlin. General properties of the electromagnetic corrections to the beta decay of a physical nucleon. *Phys. Rev.*, 164:1767–1775, Dec 1967.

[31] A. García and M. Maya. First-order radiative corrections to asymmetry coefficients in neutron decay. *Phys. Rev. D*, 17:1376–1380, Mar 1978.

[32] Vincenzo Cirigliano, Jordy de Vries, Leendert Hayen, Emanuele Mereghetti, and André Walker-Loud. Pion-Induced Radiative Corrections to Neutron β Decay. *Phys. Rev. Lett.*, 129(12):121801, 2022.

[33] E. Rutherford and F. Soddy. Radioactive change. *Philosophical Magazine*, 5:576, 1903. Reprinted in *Benchmark Papers in Physical Chemistry and Chemical Physics*, Vol. 5, Hutchinson Ross Publishing Co., Stroudsburg, Pennsylvania, 1982, ed. G. T. Seaborg and W. Loveland.

[34] Henri Becquerel. Contribution à l'étude du rayonnement du radium. *Journal de Physique Théorique et Appliquée*, 9(1):190–199, 1900. HAL archive: jpa-00240436.

[35] Lise Meitner and Otto Hahn. Magnetische spektren der betastrahlen des radiums. *Physikalische Zeitschrift*, 12:1099–1101, 1911.

[36] J. Danysz. Recherches expérimentales sur les β-rayons de la famille du radium. *Annales de Chimie et de Physique*, 30:241–320, 1913. First high-resolution magnetic spectrometry of radium beta spectrum revealing continuous distribution and up to 27 discrete lines from RaB + RaC decay series.

[37] J. Chadwick. The intensity distribution in the magnetic spectrum of β particles from radium (B + C). *Verh. Phys. Gesell.*, 16:383–391, 1914.

[38] Wolfgang Pauli. Structure et propriétés des noyaux atomiques. In G. T. Seaborg and W. Loveland, editors, *Benchmark Papers in Physical Chemistry and Chemical Physics, Volume 5*, pages 324–. Hutchinson Ross Publishing Co., Stroudsburg, Pennsylvania, 1982. Originally published in 1934.

[39] James Chadwick. The possible existence of a neutron. *Nature*, 129:312, 1932.

[40] G. Gamow and E. Teller. Selection rules for the β-disintegration. *Phys. Rev.*, 49:895–899, Jun 1936.

[41] W. Greiner and Berndt Muller. *Gauge theory of weak interactions*. 1993.

[42] C. S. Wu, E. Ambler, R. W. Hayward, D. D. Hoppes, and R. P. Hudson. Experimental test of parity conservation in beta decay. *Phys. Rev.*, 105:1413–1415, Feb 1957.

[43] M. Goldhaber, L. Grodzins, and A. W. Sunyar. Helicity of Neutrinos. *Phys. Rev.*, 109:1015–1017, 1958.

[44] R. E. Marshak and E. C. G. Sudarshan. The structure of the weak interactions. In *Proceedings of the Padua-Venice Conference on Mesons and Recently Discovered Particles*, pages V–VIII. Pergamon Press, 1958. Originally presented in 1957.

[45] R. P. Feynman and M. Gell-Mann. Theory of the fermi interaction. *Physical Review*, 109(1):193–198, 1958.

[46] Sheldon L. Glashow. Partial-symmetries of weak interactions. *Nuclear Physics*, 22:579–588, 1961.

[47] Steven Weinberg. A model of leptons. *Physical Review Letters*, 19:1264–1266, 1967.

[48] Abdus Salam. Weak and Electromagnetic Interactions. *Conf. Proc. C*, 680519:367–377, 1968.

[49] F. J. Hasert and the Gargamelle Collaboration. Observation of neutrino-like interactions without muon or electron in the gargamelle neutrino experiment. *Physics Letters B*, 46(1):138–140, 1973.

[50] C. Y. Prescott et al. Parity Nonconservation in Inelastic Electron Scattering. *Phys. Lett. B*, 77:347–352, 1978.

[51] I. S. Towner and J. C. Hardy. Superallowed $0+ \rightarrow 0+$ nuclear β-decays. *Nucl. Phys. A*, 205:33–55, 1973.

[52] J. C. Hardy and I. S. Towner. Superallowed $0^+ \rightarrow 0^+$ nuclear β decays: A new survey with precision tests of the conserved vector current hypothesis and the standard model. *Phys. Rev. C*, 79:055502, May 2009.

[53] J. C. Hardy and I. S. Towner. Superallowed $0^+ \to 0^+$ nuclear β decays: 2014 critical survey, with precise results for V_{ud} and ckm unitarity. *Phys. Rev. C*, 91:025501, Feb 2015.

[54] J. M. Robson. The radioactive decay of the neutron. *Phys. Rev.*, 83:349–358, Jul 1951.

[55] C. J. Christensen, A. Nielsen, A. Bahnsen, W. K. Brown, and B. M. Rustad. Free-neutron beta-decay half-life. *Phys. Rev. D*, 5:1628–1640, Apr 1972.

[56] A. P. Serebrov. Neutron lifetime beam anomaly and possible explanation. 12 2019.

[57] W. Mampe, P. Ageron, C. Bates, J. M. Pendlebury, and A. Steyerl. Neutron lifetime measured with stored ultracold neutrons. *Phys. Rev. Lett.*, 63:593–596, Aug 1989.

[58] V. V. Nesvizhevskii, A. P. Serebrov, R. R. Tal'daev, A. G. Kharitonov, V. P. Alfimenkov, Y. D. Mareev, and A. V. Strelkov. Measurement of the free-neutron lifetime using a gravitational trap. *JETP Letters*, 75(3):405–412, 1992. Pis'ma Zh. Eksp. Teor. Fiz. 75, 474–479 (1992).

[59] J. S. Nico, M. S. Dewey, D. M. Gilliam, F. E. Wietfeldt, X. Fei, W. M. Snow, G. L. Greene, J. Pauwels, R. Eykens, A. Lamberty, J. Van Gestel, and R. D. Scott. Measurement of the neutron lifetime by counting trapped protons in a cold neutron beam. *Phys. Rev. C*, 71:055502, May 2005.

[60] A. Serebrov et al. Measurement of the neutron lifetime using a gravitational trap and a low-temperature Fomblin coating. *Phys. Lett. B*, 605:72–78, 2005.

[61] A. Pichlmaier, V. Varlamov, K. Schreckenbach, and P. Geltenbort. Neutron lifetime measurement with the UCN trap-in-trap MAMBO II. *Phys. Lett. B*, 693:221–226, 2010.

[62] A. P. Serebrov, A. K. Fomin, A. G. Kharitonov, V. E. Varlamov, and A. V. Chechkin. New installation for measuring a neutron lifetime with a big gravitational trap of ultra cold neutrons. *Tech. Phys.*, 58(11):1681–1687, 2013.

[63] S. Arzumanov, L. Bondarenko, S. Chernyavsky, P. Geltenbort, V. Morozov, V. V. Nesvizhevsky, Yu. Panin, and A. Strepetov. A measurement of the neutron lifetime using the method of storage of ultracold neutrons and detection of inelastically up-scattered neutrons. *Phys. Lett. B*, 745:79–89, 2015.

[64] A. P. Serebrov, E. A. Kolomensky, A. K. Fomin, I. A. Krasnoshchekova, A. V. Vassiljev, D. M. Prudnikov, I. V. Shoka, A. V. Chechkin, M. E. Chaikovskiy, V. E. Varlamov, S. N. Ivanov, A. N. Pirozhkov, P. Geltenbort, O. Zimmer, T. Jenke, M. Van der Grinten, and M. Tucker. Neutron lifetime measurements with a large gravitational trap for ultracold neutrons. *Phys. Rev. C*, 97:055503, May 2018.

[65] A. T. Yue, M. S. Dewey, D. M. Gilliam, G. L. Greene, A. B. Laptev, J. S. Nico, W. M. Snow, and F. E. Wietfeldt. Improved determination of the neutron lifetime. *Phys. Rev. Lett.*, 111:222501, Nov 2013.

[66] R. W. Pattie, Jr. et al. Measurement of the neutron lifetime using a magneto-gravitational trap and in situ detection. *Science*, 360(6389):627–632, 2018.

[67] M. Schumann, T. Soldner, M. Deissenroth, F. Gluck, J. Krempel, M. Kreuz, B. Markisch, D. Mund, A. Petoukhov, and H. Abele. Measurement of the neutrino asymmetry parameter B in neutron decay. *Phys. Rev. Lett.*, 99:191803, 2007.

[68] M. Schumann, M. Kreuz, M. Deissenroth, F. Gluck, J. Krempel, B. Markisch, D. Mund, A. Petoukhov, T. Soldner, and H. Abele. Measurement of the Proton Asymmetry Parameter C in Neutron Beta Decay. *Phys. Rev. Lett.*, 100:151801, 2008.

[69] M. P. Mendenhall et al. Precision measurement of the neutron β-decay asymmetry. *Phys. Rev. C*, 87(3):032501, 2013.

[70] M. A. P. Brown et al. New result for the neutron β-asymmetry parameter A_0 from UCNA. *Phys. Rev. C*, 97(3):035505, 2018.

[71] F. E. Wietfeldt et al. Recoil-order and radiative corrections to the aCORN experiment. *Phys. Rev. C*, 110(1):015502, 2024.

[72] M. Beck et al. Improved determination of the β-$\overline{\nu}_e$ angular correlation coefficient a in free neutron decay with the $aSPECT$ spectrometer. *Phys. Rev. C*, 101(5):055506, 2020.

[73] Nicola Cabibbo. Unitary symmetry and leptonic decays. *Phys. Rev. Lett.*, 10:531–533, Jun 1963.

[74] Makoto Kobayashi and Toshihide Maskawa. CP Violation in the Renormalizable Theory of Weak Interaction. *Prog. Theor. Phys.*, 49:652–657, 1973.

[75] Vincenzo Cirigliano, Andreas Crivellin, Martin Hoferichter, and Matthew Moulson. Scrutinizing CKM unitarity with a new measurement of the Kμ3/Kμ2 branching fraction. *Phys. Lett. B*, 838:137748, 2023.

[76] Xu Feng, Mikhail Gorchtein, Lu-Chang Jin, Peng-Xiang Ma, and Chien-Yeah Seng. First-principles calculation of electroweak box diagrams from lattice QCD. *Phys. Rev. Lett.*, 124(19):192002, 2020.

[77] Chien-Yeah Seng, Xu Feng, Mikhail Gorchtein, and Lu-Chang Jin. Joint lattice QCD–dispersion theory analysis confirms the quark-mixing top-row unitarity deficit. *Phys. Rev. D*, 101(11):111301, 2020.

[78] Peng-Xiang Ma, Xu Feng, Mikhail Gorchtein, Lu-Chang Jin, and Chien-Yeah Seng. Lattice QCD calculation of the electroweak box diagrams for the kaon semileptonic decays. 2 2021.

[79] Jun-Sik Yoo, Tanmoy Bhattacharya, Rajan Gupta, Santanu Mondal, and Boram Yoon. Electroweak box diagram contribution for pion and kaon decay from lattice QCD. *Phys. Rev. D*, 108(3):034508, 2023.

[80] Vincenzo Cirigliano, Wouter Dekens, Emanuele Mereghetti, and Oleksandr Tomalak. Effective field theory for radiative corrections to charged-current processes: Vector coupling. *Phys. Rev. D*, 108(5):053003, 2023.

[81] Chien-Yeah Seng and Mikhail Gorchtein. Dispersive formalism for the nuclear structure correction δNS to the β decay rate. *Phys. Rev. C*, 107(3):035503, 2023.

[82] Chien-Yeah Seng and Mikhail Gorchtein. Towards *ab-initio* nuclear theory calculations of $\delta_{\rm C}$. 4 2023.

[83] H. Akaike. A new look at the statistical model identification. *IEEE Transactions on Automatic Control*, 19(6):716–723, 1974.

[84] Chien-Yeah Seng and Mikhail Gorchtein. Electroweak nuclear radii constrain the isospin breaking correction to Vud. *Phys. Lett. B*, 838:137654, 2023.

[85] Chien-Yeah Seng. Model-Independent Determination of Nuclear Weak Form Factors and Implications for Standard Model Precision Tests. *Phys. Rev. Lett.*, 130(15):152501, 2023.

[86] Peng-Xiang Ma, Xu Feng, Mikhail Gorchtein, Lu-Chang Jin, Keh-Fei Liu, Chien-Yeah Seng, Bi-Geng Wang, and Zhao-Long Zhang. Lattice QCD Calculation of Electroweak Box Contributions to Superallowed Nuclear and Neutron Beta Decays. 8 2023.

[87] Chien-Yeah Seng and Mikhail Gorchtein. Data-driven re-evaluation of ft-values in superallowed beta decays. 9 2023.

[88] Benedetta Belfatto, Revaz Beradze, and Zurab Berezhiani. The CKM unitarity problem: A trace of new physics at the TeV scale? *Eur. Phys. J. C*, 80(2):149, 2020.

[89] Yuval Grossman, Emilie Passemar, and Stefan Schacht. On the Statistical Treatment of the Cabibbo Angle Anomaly. *JHEP*, 07:068, 2020.

[90] Andreas Crivellin and Martin Hoferichter. β Decays as Sensitive Probes of Lepton Flavor Universality. *Phys. Rev. Lett.*, 125(11):111801, 2020.

[91] Matthew Kirk. Cabibbo anomaly versus electroweak precision tests: An exploration of extensions of the Standard Model. *Phys. Rev. D*, 103(3):035004, 2021.

[92] Andreas Crivellin, Fiona Kirk, Claudio Andrea Manzari, and Marc Montull. Global Electroweak Fit and Vector-Like Leptons in Light of the Cabibbo Angle Anomaly. *JHEP*, 12:166, 2020.

[93] Ashutosh Kumar Alok, Amol Dighe, Shireen Gangal, and Jacky Kumar. A natural resolution for the Cabibbo angle anomaly and $R_{K^{(*)}}$. 8 2021.

[94] Andreas Crivellin, Martin Hoferichter, Matthew Kirk, Claudio Andrea Manzari, and Luc Schnell. First-generation new physics in simplified models: from low-energy parity violation to the LHC. *JHEP*, 10:221, 2021.

[95] Andreas Crivellin, Matthew Kirk, Teppei Kitahara, and Federico Mescia. Global fit of modified quark couplings to EW gauge bosons and vector-like quarks in light of the Cabibbo angle anomaly. *JHEP*, 03:234, 2023.

[96] Benedetta Belfatto and Zurab Berezhiani. Are the CKM anomalies induced by vector-like quarks? Limits from flavor changing and Standard Model precision tests. *JHEP*, 10:079, 2021.

[97] Benedetta Belfatto and Sokratis Trifinopoulos. Cabibbo angle anomalies and oblique corrections: The remarkable role of the vectorlike quark doublet. *Phys. Rev. D*, (3):035022, 2023.

[98] Martín González-Alonso and Jorge Martin Camalich. Global Effective-Field-Theory analysis of New-Physics effects in (semi)leptonic kaon decays. *JHEP*, 12:052, 2016.

[99] Adam Falkowski, Martín González-Alonso, and Kin Mimouni. Compilation of low-energy constraints on 4-fermion operators in the SMEFT. *JHEP*, 08:123, 2017.

[100] Vincenzo Cirigliano, David Díaz-Calderón, Adam Falkowski, Martín González-Alonso, and Antonio Rodríguez-Sánchez. Semileptonic tau decays beyond the Standard Model. *JHEP*, 04:152, 2022.

[101] Vincenzo Cirigliano, Wouter Dekens, Jordy de Vries, Emanuele Mereghetti, and Tom

Tong. Anomalies in global SMEFT analyses: a case study of first-row CKM unitarity. 10 2023.

[102] Steven Weinberg. Nuclear forces from chiral Lagrangians. *Phys. Lett. B*, 251:288–292, 1990.

[103] R. Machleidt and D. R. Entem. Chiral effective field theory and nuclear forces. *Phys. Rept.*, 503:1–75, 2011.

[104] H. Hergert. A Guided Tour of *ab initio* Nuclear Many-Body Theory. *Front. in Phys.*, 8:379, 2020.

[105] C. Drischler, J. W. Holt, and C. Wellenhofer. Chiral Effective Field Theory and the High-Density Nuclear Equation of State. *Ann. Rev. Nucl. Part. Sci.*, 71:403–432, 2021.

[106] Sebastian Huth, Peter T. H. Pang, Ingo Tews, Junjie Yao, Tim Dietrich, Chris van den Broeck, and Achim Schwenk. Constraining neutron-star matter with microscopic and macroscopic collisions. *Nature*, 606:276–280, 2022.

[107] David J. Griffiths. *Introduction to Elementary Particles*. Wiley-VCH, 2 edition, 2008.

[108] G. A. Miller, B. M. K. Nefkens, and I. Slaus. Charge symmetry, quarks and mesons. *Phys. Rept.*, 194:1–116, 1990.

[109] W. D. Myers and W. J. Swiatecki. Nuclear masses and deformations. *Nucl. Phys.*, 81:1–60, 1966.

[110] H. A. Bethe and R. F. Bacher. Nuclear physics a: Stationary states of nuclei. *Rev. Mod. Phys.*, 8:82–229, 1936.

[111] Evgeny Epelbaum, Hans-Werner Hammer, and Ulf-G. Meissner. Modern Theory of Nuclear Forces. *Rev. Mod. Phys.*, 81:1773–1825, 2009.

[112] H. W. Hammer, S. König, and U. van Kolck. Nuclear effective field theory: status and perspectives. *Rev. Mod. Phys.*, 92(2):025004, 2020.

[113] Steven Weinberg. Effective chiral Lagrangians for nucleon - pion interactions and nuclear forces. *Nucl. Phys. B*, 363:3–18, 1991.

[114] Kai Hebeler. Three-nucleon forces: Implementation and applications to atomic nuclei and dense matter. *Phys. Rept.*, 890:1–116, 2021.

[115] Ruprecht Machleidt and Francesca Sammarruca. Recent advances in chiral EFT based nuclear forces and their applications. *Prog. Part. Nucl. Phys.*, 137:104117, 2024.

[116] P. Navratil, V. G. Gueorguiev, J. P. Vary, W. E. Ormand, and A. Nogga. Structure of A=10-13 nuclei with two plus three-nucleon interactions from chiral effective field theory. *Phys. Rev. Lett.*, 99:042501, 2007.

[117] Robert Roth, Joachim Langhammer, Angelo Calci, Sven Binder, and Petr Navratil. Similarity-Transformed Chiral NN+3N Interactions for the Ab Initio Description of 12-C and 16-O. *Phys. Rev. Lett.*, 107:072501, 2011.

[118] Robert Roth, Sven Binder, Klaus Vobig, Angelo Calci, Joachim Langhammer, and Petr Navratil. Ab Initio Calculations of Medium-Mass Nuclei with Normal-Ordered Chiral NN+3N Interactions. *Phys. Rev. Lett.*, 109:052501, 2012.

[119] G. Hagen, M. Hjorth-Jensen, G. R. Jansen, R. Machleidt, and T. Papenbrock. Continuum effects and three-nucleon forces in neutron-rich oxygen isotopes. *Phys. Rev. Lett.*, 108:242501, 2012.

[120] G. Hagen, M. Hjorth-Jensen, G. R. Jansen, R. Machleidt, and T. Papenbrock. Evolution of shell structure in neutron-rich calcium isotopes. *Phys. Rev. Lett.*, 109:032502, 2012.

[121] H. Hergert, S. K. Bogner, S. Binder, A. Calci, J. Langhammer, R. Roth, and A. Schwenk. In-Medium Similarity Renormalization Group with Chiral Two- Plus Three-Nucleon Interactions. *Phys. Rev. C*, 87(3):034307, 2013.

[122] G. Hagen, T. Papenbrock, M. Hjorth-Jensen, and D. J. Dean. Coupled-cluster computations of atomic nuclei. *Rept. Prog. Phys.*, 77(9):096302, 2014.

[123] Sven Binder, Joachim Langhammer, Angelo Calci, and Robert Roth. Ab Initio Path to Heavy Nuclei. *Phys. Lett. B*, 736:119–123, 2014.

[124] G. Hagen, G. R. Jansen, and T. Papenbrock. Structure of ^{78}Ni from first principles computations. *Phys. Rev. Lett.*, 117(17):172501, 2016.

[125] J. Simonis, K. Hebeler, J. D. Holt, J. Menendez, and A. Schwenk. Exploring sd-shell nuclei from two- and three-nucleon interactions with realistic saturation properties. *Phys. Rev. C*, 93(1):011302, 2016.

[126] J. Simonis, S. R. Stroberg, K. Hebeler, J. D. Holt, and A. Schwenk. Saturation with chiral interactions and consequences for finite nuclei. *Phys. Rev. C*, 96(1):014303, 2017.

[127] T. D. Morris, J. Simonis, S. R. Stroberg, C. Stumpf, G. Hagen, J. D. Holt, G. R. Jansen, T. Papenbrock, R. Roth, and A. Schwenk. Structure of the lightest tin isotopes. *Phys. Rev. Lett.*, 120(15):152503, 2018.

[128] V. Somà, P. Navrátil, F. Raimondi, C. Barbieri, and T. Duguet. Novel chiral Hamiltonian and observables in light and medium-mass nuclei. *Phys. Rev. C*, 101(1):014318, 2020.

[129] L. Coraggio, J. W. Holt, N. Itaco, R. Machleidt, L. E. Marcucci, and F. Sammarruca. Nuclear-matter equation of state with consistent two- and three-body perturbative chiral interactions. *Phys. Rev. C*, 89(4):044321, 2014.

[130] F. Sammarruca, L. Coraggio, J. W. Holt, N. Itaco, R. Machleidt, and L. E. Marcucci. Toward order-by-order calculations of the nuclear and neutron matter equations of state in chiral effective field theory. *Phys. Rev. C*, 91(5):054311, 2015.

[131] Francesca Sammarruca, B. Chen, L. Coraggio, N. Itaco, and R. Machleidt. Dirac-Brueckner-Hartree-Fock versus chiral effective field theory. *Phys. Rev. C*, 86:054317, 2012.

[132] F. Sammarruca, L. E. Marcucci, L. Coraggio, J. W. Holt, N. Itaco, and R. Machleidt.

Nuclear and neutron matter equations of state from high-quality potentials up to fifth order of the chiral expansion. 7 2018.

[133] K. Hebeler, S. K. Bogner, R. J. Furnstahl, A. Nogga, and A. Schwenk. Improved nuclear matter calculations from chiral low-momentum interactions. *Phys. Rev. C*, 83:031301, 2011.

[134] G. Hagen, T. Papenbrock, A. Ekström, K. A. Wendt, G. Baardsen, S. Gandolfi, M. Hjorth-Jensen, and C. J. Horowitz. Coupled-cluster calculations of nucleonic matter. *Phys. Rev. C*, 89(1):014319, 2014.

[135] L. Coraggio, J. W. Holt, N. Itaco, R. Machleidt, and F. Sammarruca. Reduced regulator dependence of neutron-matter predictions with perturbative chiral interactions. *Phys. Rev. C*, 87(1):014322, 2013.

[136] C. P. Burgess. Introduction to effective field theory. *Ann. Rev. Nucl. Part. Sci.*, 57:329–362, 2007.

[137] David B. Kaplan. Five lectures on effective field theory. 10 2005.

[138] Steven Weinberg. Phenomenological Lagrangians. *Physica A*, 96(1-2):327–340, 1979.

[139] ATLAS Collaboration. Search for supersymmetry in final states with missing transverse momentum and multiple jets with the ATLAS detector in 139 fb^{-1} of $\sqrt{s} = 13$ TeV pp collisions. *JHEP*, 09:050, 2020.

[140] CMS Collaboration. Combined measurements of Higgs boson couplings in proton-proton collisions at $\sqrt{s} = 13$ TeV. *Eur. Phys. J. C*, 79:421, 2019.

[141] Michael E. Peskin and Daniel V. Schroeder. *An Introduction to quantum field theory.* Addison-Wesley, Reading, USA, 1995.

[142] Steven Weinberg. Baryon and Lepton Nonconserving Processes. *Phys. Rev. Lett.*, 43:1566–1570, 1979.

[143] Frank Wilczek and A. Zee. Operator analysis of nucleon decay. *Phys. Rev. Lett.*, 43:1571, 1979.

[144] Ilaria Brivio and Michael Trott. Scheming in the SMEFT... and a reparameterization invariance! *JHEP*, 07:148, 2017. [Addendum: JHEP 05, 136 (2018)].

[145] Thomas Appelquist and J. Carazzone. Infrared Singularities and Massive Fields. *Phys. Rev. D*, 11:2856, 1975.

[146] Rodrigo Alonso, Elizabeth E. Jenkins, Aneesh V. Manohar, and Michael Trott. Renormalization Group Evolution of the Standard Model Dimension Six Operators III: Gauge Coupling Dependence and Phenomenology. *JHEP*, 04:159, 2014.

[147] Elizabeth E. Jenkins, Aneesh V. Manohar, and Peter Stoffer. Low-Energy Effective Field Theory below the Electroweak Scale: Operators and Matching. *JHEP*, 03:016, 2018.

[148] Stephen L. Adler. Axial-vector vertex in spinor electrodynamics. *Phys. Rev.*, 177:2426–2438, Jan 1969.

[149] J. S. Bell and R. Jackiw. A PCAC puzzle: $\pi^0 \to \gamma\gamma$ in the σ model. *Nuovo Cim. A*, 60:47–61, 1969.

[150] Stefan Scherer and Matthias R. Schindler. A Chiral perturbation theory primer. 5 2005.

[151] J. Goldstone. Field Theories with Superconductor Solutions. *Nuovo Cim.*, 19:154–164, 1961.

[152] Jeffrey Goldstone, Abdus Salam, and Steven Weinberg. Broken Symmetries. *Phys. Rev.*, 127:965–970, 1962.

[153] J. Gasser and H. Leutwyler. Chiral Perturbation Theory: Expansions in the Mass of the Strange Quark. *Nucl. Phys. B*, 250:465–516, 1985.

[154] G. Ecker. Chiral perturbation theory. *Prog. Part. Nucl. Phys.*, 35:1–80, 1995.

[155] Elizabeth Ellen Jenkins and Aneesh V. Manohar. Baryon chiral perturbation theory using a heavy fermion Lagrangian. *Phys. Lett. B*, 255:558–562, 1991.

[156] Veronique Bernard, Norbert Kaiser, and Ulf G. Meissner. Critical analysis of baryon masses and sigma terms in heavy baryon chiral perturbation theory. *Z. Phys. C*, 60:111–120, 1993.

[157] A. Sirlin. Current Algebra Formulation of Radiative Corrections in Gauge Theories and the Universality of the Weak Interactions. *Rev. Mod. Phys.*, 50:573, 1978. [Erratum: Rev.Mod.Phys. 50, 905 (1978)].

[158] Vincenzo Cirigliano, Alejandro Garcia, Doron Gazit, Oscar Naviliat-Cuncic, Guy Savard, and Albert Young. Precision Beta Decay as a Probe of New Physics. 7 2019.

[159] Carlos Ordo
nez, Lalit Ray, and Ubirajara van Kolck. Nucleon-nucleon potential from an effective chiral Lagrangian. *Phys. Rev. Lett.*, 72:1982–1985, 1994.

[160] A. Gezerlis, I. Tews, E. Epelbaum, M. Freunek, S. Gandolfi, K. Hebeler, A. Nogga, and A. Schwenk. Local chiral effective field theory interactions and quantum Monte Carlo applications. *Phys. Rev. C*, 90(5):054323, 2014.

[161] U. van Kolck. Few nucleon forces from chiral Lagrangians. *Phys. Rev. C*, 49:2932–2941, 1994.

[162] E. Epelbaum, A. Nogga, Walter Gloeckle, H. Kamada, Ulf G. Meissner, and H. Witala. Three nucleon forces from chiral effective field theory. *Phys. Rev. C*, 66:064001, 2002.

[163] Petr Navratil. Local three-nucleon interaction from chiral effective field theory. *Few Body Syst.*, 41:117–140, 2007.

[164] L. E. Marcucci, A. Kievsky, S. Rosati, R. Schiavilla, and M. Viviani. Chiral effective field theory predictions for muon capture on deuteron and ^3He. *Phys. Rev. Lett.*, 108:052502, 2012. [Erratum: Phys.Rev.Lett. 121, 049901 (2018)].

[165] A. Ekström, G. R. Jansen, K. A. Wendt, G. Hagen, T. Papenbrock, B. D. Carlsson, C. Forssén, M. Hjorth-Jensen, P. Navrátil, and W. Nazarewicz. Accurate nuclear radii

and binding energies from a chiral interaction. *Phys. Rev. C*, 91(5):051301, 2015. [Erratum: Phys.Rev.C 109, 059901 (2024)].

[166] C. Drischler, K. Hebeler, and A. Schwenk. Chiral interactions up to next-to-next-to-next-to-leading order and nuclear saturation. *Phys. Rev. Lett.*, 122(4):042501, 2019.

[167] Jun-ichi Fujita and Hironari Miyazawa. Pion Theory of Three-Body Forces. *Progress of Theoretical Physics*, 17(3):360–365, 03 1957.

[168] D. R. Entem and R. Machleidt. Accurate charge dependent nucleon nucleon potential at fourth order of chiral perturbation theory. *Phys. Rev. C*, 68:041001, 2003.

[169] Martin Hoferichter, Jacobo Ruiz de Elvira, Bastian Kubis, and Ulf-G. Meißner. Matching pion-nucleon Roy-Steiner equations to chiral perturbation theory. *Phys. Rev. Lett.*, 115(19):192301, 2015.

[170] G. J. Mathews, T. Kajino, and T. Shima. Big bang nucleosynthesis with a new neutron lifetime. *Phys. Rev. D*, 71:021302, Jan 2005.

[171] Dirk Dubbers and Michael G. Schmidt. The neutron and its role in cosmology and particle physics. *Rev. Mod. Phys.*, 83:1111–1171, Oct 2011.

[172] A. N. Ivanov, M. Pitschmann, and N. I. Troitskaya. Neutron β^- decay as a laboratory for testing the standard model. *Phys. Rev. D*, 88:073002, Oct 2013.

[173] M. Gonzalez-Alonso, O. Naviliat-Cuncic, and N. Severijns. New physics searches in nuclear and neutron β decay. *Progress in Particle and Nuclear Physics*, 104:165 – 223, 2019.

[174] William J. Marciano and Alberto Sirlin. Improved calculation of electroweak radiative corrections and the value of V_{ud}. *Phys. Rev. Lett.*, 96:032002, Jan 2006.

[175] Chien-Yeah Seng, Mikhail Gorchtein, and Michael J. Ramsey-Musolf. Dispersive evaluation of the inner radiative correction in neutron and nuclear β decay. *Phys. Rev. D*, 100:013001, Jul 2019.

[176] Andrzej Czarnecki, William J. Marciano, and Alberto Sirlin. Radiative corrections to neutron and nuclear beta decays revisited. *Phys. Rev. D*, 100:073008, Oct 2019.

[177] Leendert Hayen. Standard model $\mathcal{O}(\alpha)$ renormalization of g_A and its impact on new physics searches. *Phys. Rev. D*, 103:113001, Jun 2021.

[178] T. M. Ito, E. R. Adamek, N. B. Callahan, J. H. Choi, S. M. Clayton, C. Cude-Woods, S. Currie, X. Ding, D. E. Fellers, P. Geltenbort, S. K. Lamoreaux, C.-Y. Liu, S. MacDonald, M. Makela, C. L. Morris, R. W. Pattie, J. C. Ramsey, D. J. Salvat, A. Saunders, E. I. Sharapov, S. Sjue, A. P. Sprow, Z. Tang, H. L. Weaver, W. Wei, and A. R. Young. Performance of the upgraded ultracold neutron source at los alamos national laboratory and its implication for a possible neutron electric dipole moment experiment. *Phys. Rev. C*, 97:012501, Jan 2018.

[179] A. T. Holley, L. J. Broussard, J. L. Davis, K. Hickerson, T. M. Ito, C.-Y. Liu, J. T. M. Lyles, M. Makela, R. R. Mammei, M. P. Mendenhall, C. L. Morris, R. Mortensen, R. W. Pattie, R. Rios, A. Saunders, and A. R. Young. A high-field adiabatic fast passage ultracold neutron spin flipper for the ucna experiment. *Review of Scientific Instruments*, 83(7):073505, 2012.

[180] P.L. Walstrom, J.D. Bowman, S.I. Penttila, C. Morris, and A. Saunders. A magneto-gravitational trap for absolute measurement of the ultra-cold neutron lifetime. *Nuclear Instruments and Methods in Physics Research Section A: Accelerators, Spectrometers, Detectors and Associated Equipment*, 599(1):82 – 92, 2009.

[181] K. Halbach. Design of permanent multipole magnets with oriented rare earth cobalt material. *Nuclear Instruments and Methods*, 169(1):1 – 10, 1980.

[182] R. Picker, I. Altarev, P. Amos, B. Franke, P. Geltenbort, E. Gutsmiedl, F.J. Hartmann, A. Mann, S. Materne, A.R. Müller, S. Paul, R. Stoepler, and H.-F. Wirth. Investigation of titanium and polyethylene as ucn absorber materials with abex. *Nuclear Instruments and Methods in Physics Research Section A: Accelerators, Spectrometers,*

Detectors and Associated Equipment, 611(2):297 – 301, 2009. Particle Physics with Slow Neutrons.

[183] D. J. Salvat, E. R. Adamek, D. Barlow, J. D. Bowman, L. J. Broussard, N. B. Callahan, S. M. Clayton, C. Cude-Woods, S. Currie, E. B. Dees, W. Fox, P. Geltenbort, K. P. Hickerson, A. T. Holley, C.-Y. Liu, M. Makela, J. Medina, D. J. Morley, C. L. Morris, S. I. Penttilä, J. Ramsey, A. Saunders, S. J. Seestrom, E. I. Sharapov, S. K. L. Sjue, B. A. Slaughter, J. Vanderwerp, B. VornDick, P. L. Walstrom, Z. Wang, T. L. Womack, and A. R. Young. Storage of ultracold neutrons in the magneto-gravitational trap of the UCNτ experiment. *Phys. Rev. C*, 89:052501, May 2014.

[184] C. L. Morris, E. R. Adamek, L. J. Broussard, N. B. Callahan, S. M. Clayton, C. Cude-Woods, S. A. Currie, X. Ding, W. Fox, K. P. Hickerson, M. A. Hoffbauer, A. T. Holley, A. Komives, C.-Y. Liu, M. Makela, R. W. Pattie, J. Ramsey, D. J. Salvat, A. Saunders, S. J. Seestrom, E. I. Sharapov, S. K. Sjue, Z. Tang, J. Vanderwerp, B. Vogelaar, P. L. Walstrom, Z. Wang, Wanchun Wei, J. W. Wexler, T. L. Womack, A. R. Young, and B. A. Zeck. A new method for measuring the neutron lifetime using an in situ neutron detector. *Review of Scientific Instruments*, 88(5):053508, 2017.

[185] Zhehui Wang, M.A. Hoffbauer, C.L. Morris, N.B. Callahan, E.R. Adamek, J.D. Bacon, M. Blatnik, A.E. Brandt, L.J. Broussard, S.M. Clayton, C. Cude-Woods, S. Currie, E.B. Dees, X. Ding, J. Gao, F.E. Gray, K.P. Hickerson, A.T. Holley, T.M. Ito, C.-Y. Liu, M. Makela, J.C. Ramsey, R.W. Pattie, D.J. Salvat, A. Saunders, D.W. Schmidt, R.K. Schulze, S.J. Seestrom, E.I. Sharapov, A. Sprow, Z. Tang, W. Wei, J. Wexler, T.L. Womack, A.R. Young, and B.A. Zeck. A multilayer surface detector for ultracold neutrons. *Nuclear Instruments and Methods in Physics Research Section A: Accelerators, Spectrometers, Detectors and Associated Equipment*, 798:30 – 35, 2015.

[186] A. Anghel, T. L. Bailey, G. Bison, B. Blau, L. J. Broussard, S. M. Clayton, C. Cude-Woods, M. Daum, A. Hawari, N. Hild, P. Huffman, T. M. Ito, K. Kirch, E. Korobkina, B. Lauss, K. Leung, E. M. Lutz, M. Makela, G. Medlin, C. L. Morris, R. W. Pattie, D. Ries, A. Saunders, P. Schmidt-Wellenburg, V. Talanov, A. R. Young, B. Wehring,

C. White, M. Wohlmuther, and G. Zsigmond. Solid deuterium surface degradation at ultracold neutron sources. *The European Physical Journal A*, 54(9), Sep 2018.

[187] Hervé Abdi and Lynne J. Williams. Principal component analysis. *WIREs Computational Statistics*, 2(4):433–459, 2010.

[188] Daniel Foreman-Mackey, David W. Hogg, Dustin Lang, and Jonathan Goodman. emcee: The MCMC hammer. *Publications of the Astronomical Society of the Pacific*, 125(925):306–312, mar 2013.

[189] F. M. Gonzalez. Precision measurement of the neutron lifetime with the ucnτ experiment, 2021. PhD dissertation.

[190] Jay M. Ver Hoef and Peter L. Boveng. Quasi-poisson vs. negative binomial regression: How should we model overdispersed count data? *Ecology*, 88(11):2766–2772, 2007.

[191] Eric Michael Fries. *Precision Measurement of the Neutron Lifetime*. PhD thesis, California Institute of Technology, Pasadena, CA, USA, 2022. Ph.D. dissertation.

[192] Nathan Callahan, Chen-Yu Liu, Francisco Gonzalez, E. Adamek, J. D. Bowman, L. Broussard, S. M. Clayton, S. Currie, C. Cude-Woods, E. B. Dees, X. Ding, W. Fox, P. Geltenbort, K. P. Hickerson, M. A. Hoffbauer, A. T. Holley, A. Komives, S. W. T. MacDonald, M. Makela, C. L. Morris, J. D. Ortiz, R. W. Pattie, J. Ramsey, D. J. Salvat, A. Saunders, E. I. Sharapov, S. K. L. Sjue, Z. Tang, J. Vanderwerp, B. Vogelaar, P. L. Walstrom, Z. Wang, H. Weaver, W. Wei, J. Wexler, and A. R. Young. Monte carlo simulations of trapped ultracold neutrons in the UCNτ experiment. *Phys. Rev. C*, 100:015501, Jul 2019.

[193] S. J. Seestrom, E. R. Adamek, D. Barlow, L. J. Broussard, N. B. Callahan, S. M. Clayton, C. Cude-Woods, S. Currie, E. B. Dees, W. Fox, P. Geltenbort, K. P. Hickerson, A. T. Holley, C.-Y. Liu, M. Makela, J. Medina, D. J. Morley, C. L. Morris, J. Ramsey, A. Roberts, D. J. Salvat, A. Saunders, E. I. Sharapov, S. K. L. Sjue, B. A. Slaughter, B. VornDick, P. L. Walstrom, Z. Wang, T. L. Womack, A. R. Young, and B. A. Zeck. Upscattering of ultracold neutrons from gases. *Phys. Rev. C*, 92:065501, Dec 2015.

[194] S. J. Seestrom, E. R. Adamek, D. Barlow, M. Blatnik, L. J. Broussard, N. B. Callahan, S. M. Clayton, C. Cude-Woods, S. Currie, E. B. Dees, W. Fox, M. Hoffbauer, K. P. Hickerson, A. T. Holley, C.-Y. Liu, M. Makela, J. Medina, D. J. Morley, C. L. Morris, R. W. Pattie, J. Ramsey, A. Roberts, D. J. Salvat, A. Saunders, E. I. Sharapov, S. K. L. Sjue, B. A. Slaughter, P. L. Walstrom, Z. Wang, J. Wexler, T. L. Womack, A. R. Young, J. Vanderwerp, and B. A. Zeck. Total cross sections for ultracold neutrons scattered from gases. *Phys. Rev. C*, 95:015501, Jan 2017.

[195] T. Albahri, A. Anastasi, A. Anisenkov, K. Badgley, S. Baeßler, I. Bailey, V. A. Baranov, E. Barlas-Yucel, T. Barrett, A. Basti, F. Bedeschi, M. Berz, M. Bhattacharya, H. P. Binney, P. Bloom, J. Bono, E. Bottalico, T. Bowcock, G. Cantatore, R. M. Carey, B. C. K. Casey, D. Cauz, R. Chakraborty, S. P. Chang, A. Chapelain, S. Charity, R. Chislett, J. Choi, Z. Chu, T. E. Chupp, S. Corrodi, L. Cotrozzi, J. D. Crnkovic, S. Dabagov, P. T. Debevec, S. Di Falco, P. Di Meo, G. Di Sciascio, R. Di Stefano, A. Driutti, V. N. Duginov, M. Eads, J. Esquivel, M. Farooq, R. Fatemi, C. Ferrari, M. Fertl, A. T. Fienberg, A. Fioretti, D. Flay, E. Frlež, N. S. Froemming, J. Fry, C. Gabbanini, M. D. Galati, S. Ganguly, A. Garcia, J. George, L. K. Gibbons, A. Gioiosa, K. L. Giovanetti, P. Girotti, W. Gohn, T. Gorringe, J. Grange, S. Grant, F. Gray, S. Haciomeroglu, T. Halewood-Leagas, D. Hampai, F. Han, J. Hempstead, A. T. Herrod, D. W. Hertzog, G. Hesketh, A. Hibbert, Z. Hodge, J. L. Holzbauer, K. W. Hong, R. Hong, M. Iacovacci, M. Incagli, P. Kammel, M. Kargiantoulakis, M. Karuza, J. Kaspar, D. Kawall, L. Kelton, A. Keshavarzi, D. Kessler, K. S. Khaw, Z. Khechadoorian, N. V. Khomutov, B. Kiburg, M. Kiburg, O. Kim, Y. I. Kim, B. King, N. Kinnaird, E. Kraegeloh, A. Kuchibhotla, N. A. Kuchinskiy, K. R. Labe, J. LaBounty, M. Lancaster, M. J. Lee, S. Lee, S. Leo, B. Li, D. Li, L. Li, I. Logashenko, A. Lorente Campos, A. Lucà, G. Lukicov, A. Lusiani, A. L. Lyon, B. MacCoy, R. Madrak, K. Makino, F. Marignetti, S. Mastroianni, J. P. Miller, S. Miozzi, W. M. Morse, J. Mott, A. Nath, H. Nguyen, R. Osofsky, S. Park, G. Pauletta, G. M. Piacentino, R. N. Pilato, K. T. Pitts, B. Plaster, D. Počanić, N. Pohlman, C. C. Polly, J. Price, B. Quinn, N. Raha, S. Ramachandran, E. Ramberg, J. L. Ritchie, B. L. Roberts, D. L. Rubin, L. Santi,

C. Schlesier, A. Schreckenberger, Y. K. Semertzidis, D. Shemyakin, M. W. Smith, M. Sorbara, D. Stöckinger, J. Stapleton, C. Stoughton, D. Stratakis, T. Stuttard, H. E. Swanson, G. Sweetmore, D. A. Sweigart, M. J. Syphers, D. A. Tarazona, T. Teubner, A. E. Tewsley-Booth, K. Thomson, V. Tishchenko, N. H. Tran, W. Turner, E. Valetov, D. Vasilkova, G. Venanzoni, T. Walton, A. Weisskopf, L. Welty-Rieger, P. Winter, A. Wolski, and W. Wu. Measurement of the anomalous precession frequency of the muon in the fermilab muon $g-2$ experiment. *Phys. Rev. D*, 103:072002, Apr 2021.

[196] G. L. Greene and P. Geltenbort. The neutron enigma. *Scientific American*, 314(4):36–41, 2016.

[197] A. Steyerl, J. M. Pendlebury, C. Kaufman, S. S. Malik, and A. M. Desai. Quasielastic scattering in the interaction of ultracold neutrons with a liquid wall and application in a reanalysis of the mambo i neutron-lifetime experiment. *Phys. Rev. C*, 85:065503, Jun 2012.

[198] V. F. Ezhov, A. Z. Andreev, G. Ban, B. A. Bazarov, P. Geltenbort, A. G. Glushkov, V. A. Knyazkov, N. A. Kovrizhnykh, G. B. Krygin, O. Naviliat-Cuncic, and V. L. Ryabov. Measurement of the neutron lifetime with ultracold neutrons stored in a magneto-gravitational trap. *JETP Letters*, 107(11):671–675, Jun 2018.

[199] A. P. Serebrov, E. A. Kolomensky, A. K. Fomin, I. A. Krasnoshchekova, A. V. Vassiljev, D. M. Prudnikov, I. V. Shoka, A. V. Chechkin, M. E. Chaikovskiy, V. E. Varlamov, S. N. Ivanov, A. N. Pirozhkov, P. Geltenbort, O. Zimmer, T. Jenke, M. Van der Grinten, and M. Tucker. Neutron lifetime measurements with a large gravitational trap for ultracold neutrons. *Phys. Rev. C*, 97:055503, May 2018.

[200] Don Colladay and V. Alan Kostelecky. Lorentz violating extension of the standard model. *Phys. Rev. D*, 58:116002, 1998.

[201] Bartosz Fornal and Benjamín Grinstein. Dark matter interpretation of the neutron decay anomaly. *Phys. Rev. Lett.*, 120:191801, May 2018.

[202] James M. Cline and Jonathan M. Cornell. Dark decay of the neutron. *JHEP*, 07:081, 2018.

[203] M. Pfützner and K. Riisager. Examining the possibility to observe neutron dark decay in nuclei. *Phys. Rev. C*, 97(4):042501, 2018.

[204] Z. Tang, R. W. Pattie, N. B. Callahan, C. Cude-Woods, A. Huber, T. M. Ito, A. Knecht, M. Makela, J. W. Martin, S. M. Seestrom, W. Wei, and X. Zhao. Search for the neutron decay $n \to \chi + \gamma$. *Phys. Rev. Lett.*, 121(2):022505, 2018.

[205] X. Sun, K. K. Vos, P. D. Shidling, P. Dendooven, K. Blaum, M. P. Reiter, R. X. Schüssler, A. Türler, D. T. Yordanov, and D. Beck. Search for a dark decay of the neutron from the nuclear decay of ^{11}be. *Phys. Rev. C*, 97(5):052501, 2018.

[206] D. Dubbers and M. G. Schmidt. The neutron and its role in cosmology and particle physics. *Reviews of Modern Physics*, 83:1111–1171, 2011.

[207] Zurab Berezhiani. Neutron lifetime and dark decays of the neutron and hydrogen. *Eur. Phys. J. C*, 79(6):484, 2019.

[208] Elizabeth E. Jenkins, Aneesh V. Manohar, and Michael Trott. Renormalization Group Evolution of the Standard Model Dimension Six Operators I: Formalism and lambda Dependence. *JHEP*, 10:087, 2013.

[209] Vincenzo Cirigliano, James Jenkins, and Martin Gonzalez-Alonso. Semileptonic decays of light quarks beyond the Standard Model. *Nucl. Phys. B*, 830:95–115, 2010.

[210] Adam Falkowski, Martín González-Alonso, and Oscar Naviliat-Cuncic. Comprehensive analysis of beta decays within and beyond the Standard Model. *JHEP*, 04:126, 2021.

[211] Martín González-Alonso, Jorge Martin Camalich, and Kin Mimouni. Renormalization-group evolution of new physics contributions to (semi)leptonic meson decays. *Phys. Lett. B*, 772:777–785, 2017.

[212] Elizabeth E. Jenkins, Aneesh V. Manohar, and Michael Trott. Renormalization Group Evolution of the Standard Model Dimension Six Operators II: Yukawa Dependence. *JHEP*, 01:035, 2014.

[213] Wouter Dekens and Peter Stoffer. Low-energy effective field theory below the electroweak scale: matching at one loop. *JHEP*, 10:197, 2019.

[214] Zahari Kassabov, Maeve Madigan, Luca Mantani, James Moore, Manuel Morales Alvarado, Juan Rojo, and Maria Ubiali. The top quark legacy of the LHC Run II for PDF and SMEFT analyses. *JHEP*, 05:205, 2023.

[215] Francesco Garosi, David Marzocca, Antonio Rodriguez-Sanchez, and Alfredo Stanzione. Indirect constraints on top quark operators from a global SMEFT analysis. 9 2023.

[216] Adam Falkowski and Kin Mimouni. Model independent constraints on four-lepton operators. *JHEP*, 02:086, 2016.

[217] Jason Aebischer, Christoph Bobeth, Andrzej J. Buras, and Jacky Kumar. SMEFT ATLAS of ΔF = 2 transitions. *JHEP*, 12:187, 2020.

[218] Andy Buckley, Christoph Englert, James Ferrando, David J. Miller, Liam Moore, Michael Russell, and Chris D. White. Constraining top quark effective theory in the LHC Run II era. *JHEP*, 04:015, 2016.

[219] Jacob J. Ethier, Giacomo Magni, Fabio Maltoni, Luca Mantani, Emanuele R. Nocera, Juan Rojo, Emma Slade, Eleni Vryonidou, and Cen Zhang. Combined SMEFT interpretation of Higgs, diboson, and top quark data from the LHC. *JHEP*, 11:089, 2021.

[220] Martin Jung and David M. Straub. Constraining new physics in $b \to c\ell\nu$ transitions. *JHEP*, 01:009, 2019.

[221] S. L. Glashow, J. Iliopoulos, and L. Maiani. Weak Interactions with Lepton-Hadron Symmetry. *Phys. Rev. D*, 2:1285–1292, 1970.

[222] Andrzej J. Buras, Dario Buttazzo, Jennifer Girrbach-Noe, and Robert Knegjens. $K^+ \to \pi^+ \nu\overline{\nu}$ and $K_L \to \pi^0 \nu\overline{\nu}$ in the Standard Model: status and perspectives. *JHEP*, 11:033, 2015.

[223] Lukas Allwicher, Claudia Cornella, Gino Isidori, and Ben A. Stefanek. New Physics in the Third Generation: A Comprehensive SMEFT Analysis and Future Prospects. 10 2023.

[224] Andrzej J. Buras and Elena Venturini. The exclusive vision of rare K and B decays and of the quark mixing in the standard model. *Eur. Phys. J. C*, 82(7):615, 2022.

[225] R. L. Workman et al. Review of Particle Physics. *PTEP*, 2022:083C01, 2022.

[226] Joachim Brod and Martin Gorbahn. Next-to-Next-to-Leading-Order Charm-Quark Contribution to the CP Violation Parameter ϵ_K and ΔM_K. *Phys. Rev. Lett.*, 108:121801, 2012.

[227] Andrzej J. Buras. The Return of Kaon Flavour Physics. *Acta Phys. Polon. B*, 49:1043, 2018.

[228] Bigeng Wang. Calculating Δm_K with lattice QCD. *PoS*, LATTICE2021:141, 2022.

[229] J. de Blas, J. C. Criado, M. Perez-Victoria, and J. Santiago. Effective description of general extensions of the Standard Model: the complete tree-level dictionary. *JHEP*, 03:109, 2018.

[230] Jonathan M. Arnold, Bartosz Fornal, and Mark B. Wise. Simplified models with baryon number violation but no proton decay. *Phys. Rev. D*, 87:075004, 2013.

[231] Yong Chuan Zhan, Ze Long Liu, Shi Ang Li, Chong Sheng Li, and Hai Tao Li. Threshold resummation for the production of a color sextet (antitriplet) scalar at the LHC. *Eur. Phys. J. C*, 74:2716, 2014.

[232] F. del Aguila, J. de Blas, and M. Perez-Victoria. Electroweak Limits on General New Vector Bosons. *JHEP*, 09:033, 2010.

[233] Claudius Krause, Antonio Pich, Ignasi Rosell, Joaquín Santos, and Juan José Sanz-Cillero. Colorful Imprints of Heavy States in the Electroweak Effective Theory. *JHEP*, 05:092, 2019.

[234] J. C. Hardy and I. S. Towner. Superallowed $0^+ \to 0^+$ nuclear β decays: 2020 critical survey, with implications for V_{ud} and CKM unitarity. *Phys. Rev. C*, 102(4):045501, October 2020.

[235] Vincenzo Cirigliano, Wouter Dekens, Jordy de Vries, Stefano Gandolfi, Martin Hoferichter, and Emanuele Mereghetti. Ab initio electroweak corrections to superallowed β decays and their impact on Vud. *Phys. Rev. C*, 110(5):055502, 2024.

[236] Vincenzo Cirigliano, Wouter Dekens, Jordy de Vries, Stefano Gandolfi, Martin Hoferichter, and Emanuele Mereghetti. Radiative Corrections to Superallowed β Decays in Effective Field Theory. *Phys. Rev. Lett.*, 133(21):211801, 2024.

[237] I. Tews, J. Margueron, and S. Reddy. Critical examination of constraints on the equation of state of dense matter obtained from GW170817. *Phys. Rev. C*, 98(4):045804, 2018.

[238] S. R. Beane, S. D. Cohen, W. Detmold, H. W. Lin, and M. J. Savage. Nuclear σ terms and scalar-isoscalar WIMP-nucleus interactions from lattice QCD. *Phys. Rev. D*, 89:074505, 2014.

[239] Thomas Mehen and Iain W. Stewart. Renormalization schemes and the range of two nucleon effective field theory. *Phys. Rev. C*, 59:2365–2383, 1999.

[240] S. R. Beane, P. F. Bedaque, K. Orginos, and M. J. Savage. Nucleon-nucleon scattering from fully-dynamical lattice QCD. *Phys. Rev. Lett.*, 97:012001, 2006.

[241] Jambul Gegelia and Stefan Scherer. Consistency of the effective field theory approach to the nucleon nucleon interaction problem revisited. *Int. J. Mod. Phys. A*, 21:1079–1089, 2006.

[242] V. Cirigliano, W. Dekens, J. De Vries, M. L. Graesser, E. Mereghetti, S. Pastore, M. Piarulli, U. Van Kolck, and R. B. Wiringa. Renormalized approach to neutrinoless double- β decay. *Phys. Rev. C*, 100(5):055504, 2019.

[243] Silas R. Beane and Martin J. Savage. The Quark mass dependence of two nucleon systems. *Nucl. Phys. A*, 717:91–103, 2003.

[244] David B. Kaplan, Martin J. Savage, and Mark B. Wise. Two nucleon systems from effective field theory. *Nucl. Phys. B*, 534:329–355, 1998.

[245] David B. Kaplan, Martin J. Savage, and Mark B. Wise. A New expansion for nucleon-nucleon interactions. *Phys. Lett. B*, 424:390–396, 1998.

[246] M. Piarulli, L. Girlanda, R. Schiavilla, R. Navarro Pérez, J. E. Amaro, and E. Ruiz Arriola. Minimally nonlocal nucleon-nucleon potentials with chiral two-pion exchange including Δ resonances. *Phys. Rev. C*, 91(2):024003, 2015.

[247] E. Epelbaum, H. Krebs, and U. G. Meißner. Improved chiral nucleon-nucleon potential up to next-to-next-to-next-to-leading order. *Eur. Phys. J. A*, 51(5):53, 2015.

[248] Maria Piarulli, Luca Girlanda, Rocco Schiavilla, Alejandro Kievsky, Alessandro Lovato, Laura E. Marcucci, Steven C. Pieper, Michele Viviani, and Robert B. Wiringa. Local chiral potentials with Δ-intermediate states and the structure of light nuclei. *Phys. Rev. C*, 94(5):054007, 2016.

[249] P. Reinert, H. Krebs, and E. Epelbaum. Semilocal momentum-space regularized chiral two-nucleon potentials up to fifth order. *Eur. Phys. J. A*, 54(5):86, 2018.

[250] S. R. Beane, Paulo F. Bedaque, M. J. Savage, and U. van Kolck. Towards a perturbative theory of nuclear forces. *Nucl. Phys. A*, 700:377–402, 2002.

[251] J. Gasser, M. A. Ivanov, E. Lipartia, M. Mojzis, and A. Rusetsky. Ground state energy of pionic hydrogen to one loop. *Eur. Phys. J. C*, 26:13–34, 2002.

[252] Martin Hoferichter, Bastian Kubis, and Ulf-G. Meißner. Isospin breaking in the pion-nucleon scattering lengths. *Phys. Lett. B*, 678:65–71, 2009.

[253] Martin Hoferichter, Bastian Kubis, and Ulf-G. Meißner. Isospin Violation in Low-Energy Pion-Nucleon Scattering Revisited. *Nucl. Phys. A*, 833:18–103, 2010.

[254] S. R. Beane, V. Bernard, E. Epelbaum, Ulf-G. Meißner, and Daniel R. Phillips. The S wave pion nucleon scattering lengths from pionic atoms using effective field theory. *Nucl. Phys. A*, 720:399–415, 2003.

[255] S. Liebig, V. Baru, F. Ballout, C. Hanhart, and A. Nogga. Towards a high precision calculation for the pion-nucleus scattering lengths. *Eur. Phys. J. A*, 47:69, 2011.

[256] V. Baru, C. Hanhart, M. Hoferichter, B. Kubis, A. Nogga, and D. R. Phillips. Precision calculation of the π^- deuteron scattering length and its impact on threshold π N scattering. *Phys. Lett. B*, 694:473–477, 2011.

[257] V. Baru, C. Hanhart, M. Hoferichter, B. Kubis, A. Nogga, and D. R. Phillips. Precision calculation of threshold $\pi^- d$ scattering, πN scattering lengths, and the GMO sum rule. *Nucl. Phys. A*, 872:69–116, 2011.

[258] V. Baru, E. Epelbaum, C. Hanhart, M. Hoferichter, A. E. Kudryavtsev, and D. R. Phillips. The Multiple-scattering series in pion-deuteron scattering and the nucleon-nucleon potential: Perspectives from effective field theory. *Eur. Phys. J. A*, 48:69, 2012.

[259] Bugra Borasoy and Harald W. Griesshammer. The S wave pion deuteron scattering length in effective field theory. 5 2001.

[260] B. Borasoy and H. W. Griesshammer. Pion deuteron scattering length in effective field theory. *Int. J. Mod. Phys. E*, 12:65–80, 2003.

[261] N. Kaiser. Chiral four-body interactions in nuclear matter. *Eur. Phys. J. A*, 48:135, 2012.

[262] Martin Hoferichter, Jacobo Ruiz de Elvira, Bastian Kubis, and Ulf-G. Meißner. Roy–Steiner-equation analysis of pion–nucleon scattering. *Phys. Rept.*, 625:1–88, 2016.

[263] D. Siemens, J. Ruiz de Elvira, E. Epelbaum, M. Hoferichter, H. Krebs, B. Kubis, and U. G. Meißner. Reconciling threshold and subthreshold expansions for pion–nucleon scattering. *Phys. Lett. B*, 770:27–34, 2017.

[264] T. A. Rijken. Soft two pion exchange nucleon-nucleon potentials. *Annals Phys.*, 208:253–298, 1991.

[265] S. Ishikawa and M. R. Robilotta. Two-pion exchange three-nucleon potential: O(q**4) chiral expansion. *Phys. Rev. C*, 76:014006, 2007.

[266] V. Bernard, E. Epelbaum, H. Krebs, and Ulf-G. Meissner. Subleading contributions to the chiral three-nucleon force. I. Long-range terms. *Phys. Rev. C*, 77:064004, 2008.

[267] V. Bernard, E. Epelbaum, H. Krebs, and U. G. Meissner. Subleading contributions to the chiral three-nucleon force II: Short-range terms and relativistic corrections. *Phys. Rev. C*, 84:054001, 2011.

[268] Bao-An Li, Plamen G. Krastev, De-Hua Wen, and Nai-Bo Zhang. Towards Understanding Astrophysical Effects of Nuclear Symmetry Energy. *Eur. Phys. J. A*, 55(7):117, 2019.

[269] C. Drischler, R. J. Furnstahl, J. A. Melendez, and D. R. Phillips. How Well Do We Know the Neutron-Matter Equation of State at the Densities Inside Neutron Stars? A Bayesian Approach with Correlated Uncertainties. *Phys. Rev. Lett.*, 125(20):202702, 2020.

[270] I. Tews, R. Somasundaram, D. Lonardoni, H. Göttling, R. Seutin, J. Carlson, S. Gandolfi, K. Hebeler, and A. Schwenk. Neutron matter from local chiral EFT interactions at large cutoffs. 7 2024.

[271] D. Adhikari et al. Accurate Determination of the Neutron Skin Thickness of ^{208}Pb through Parity-Violation in Electron Scattering. *Phys. Rev. Lett.*, 126(17):172502, 2021.

[272] Brendan T. Reed, F. J. Fattoyev, C. J. Horowitz, and J. Piekarewicz. Implications of PREX-2 on the Equation of State of Neutron-Rich Matter. *Phys. Rev. Lett.*, 126(17):172503, 2021.

[273] Maria Dawid, Wouter Dekens, Christian Drischler, Mai Kumamoto, and Sanjay Reddy. Phenomnelogical constraints on the pion coupling to two nucleons and their implications for neutron stars. . *in preperation*, 2024.

[274] Bryce Fore, Norbert Kaiser, Sanjay Reddy, and Neill C. Warrington. Mass of charged pions in neutron-star matter. *Phys. Rev. C*, 110(2):025803, 2024.

[275] C. J. Batty, E. Friedman, and A. Gal. Strong interaction physics from hadronic atoms. *Phys. Rept.*, 287:385–445, 1997.

[276] E. Friedman. Density dependence of the s wave repulsion in pionic atoms. *Nucl. Phys. A*, 710:117–130, 2002.

[277] R. Somasundaram, C. Drischler, I. Tews, and J. Margueron. Constraints on the nuclear symmetry energy from asymmetric-matter calculations with chiral NN and $3N$ interactions. *Phys. Rev. C*, 103(4):045803, 2021.

[278] Domenico Logoteta, Ignazio Bombaci, and Alejandro Kievsky. Nuclear matter calculations with chiral interactions. *J. Phys. Conf. Ser.*, 981(1):012009, 2018.

[279] J. E. Lynn, I. Tews, J. Carlson, S. Gandolfi, A. Gezerlis, K. E. Schmidt, and A. Schwenk. Quantum Monte Carlo calculations of light nuclei with local chiral two- and three-nucleon interactions. *Phys. Rev. C*, 96(5):054007, 2017.

[280] Doron Gazit, Sofia Quaglioni, and Petr Navratil. Three-Nucleon Low-Energy Constants from the Consistency of Interactions and Currents in Chiral Effective Field Theory. *Phys. Rev. Lett.*, 103:102502, 2009. [Erratum: Phys.Rev.Lett. 122, 029901 (2019)].

[281] M. Piarulli et al. Light-nuclei spectra from chiral dynamics. *Phys. Rev. Lett.*, 120(5):052503, 2018.

[282] E. Epelbaum et al. Few- and many-nucleon systems with semilocal coordinate-space regularized chiral two- and three-body forces. *Phys. Rev. C*, 99(2):024313, 2019.